

Chemical Vapour Deposition of Gold Nanoparticle and Metal Oxide Composites

Clair Ka Tze Chew



A thesis submitted for the degree of
Doctor of Philosophy in Chemistry

Declaration

I, Clair Ka Tze Chew confirm that the work presented in this thesis is my own. Where information has been derived from other sources, I confirm that this has been indicated in the thesis.

Dedication

This is for my friends and family but especially Mama and Papa Chew.

Abstract

Aerosol-assisted chemical vapour deposition (AACVD) is a well-known method for synthesising metal oxide thin films on glass. The primary metal oxide presented here is SnO_2 for its transparent conducting oxide (TCO) properties. Its fluorine doped form is an established TCO and widely deposited as a window coating.

The versatility of the AACVD method is displayed in this thesis with results of the facile deposition of gold nanoparticles (AuNPs). AuNPs are another useful class of materials but in this thesis the interest is mainly in their surface plasmon resonance (SPR) absorption. Composites of fluorine doped SnO_2 and AuNPs were synthesised, allowing the successful combination of the optical and electronic characteristics in one material.

The SPR of AuNPs, which gives them their pink and purple colouring, depends on many factors including size, shape and the refractive index of the surrounding medium. Using AACVD, AuNPs were then further layered into composites with other metal oxides, including TiO_2 , Al_2O_3 , Ga_2O_3 , ZnO and MgO . Ellipsometric measurements were performed on the metal oxides in order for their refractive index to be calculated and these were compared to the shifts in the SPR that were observed.

AACVD can also deposit AuNPs onto glass (silica) wool as well as on flat float glass. These were shown to be active as catalysts in the selective oxidation of benzyl alcohol.

A wide range of functional materials have been synthesised and analysed in this thesis. New materials with interesting properties can be made from creating composites. This thesis shows that AACVD is capable of synthesising compounds and structures applicable for many devices.

Publications

Aerosol-assisted deposition of gold nanoparticle-tin dioxide composite films, C. Chew, P. Bishop, C. Salcianu, C. J. Carmalt and I. P. Parkin, *RSC Advances*, 2014, **4**, 25, 13182.

Functional thin film coatings incorporating gold nanoparticles in a transparent conducting fluorine doped tin oxide matrix, C. K. T. Chew, C. Salcianu, P. Bishop, C. J. Carmalt and I. P. Parkin, *Journal of Materials Chemistry C*, 2014, **3**, 1118-1125.

Influencing FTO thin film growth with thin seeding layers: a route to microstructural modification, N. Noor, C. K. T. Chew, D. S. Bhachu, M. R. Waugh, C. J. Carmalt and I. P. Parkin, *Journal of Materials Chemistry C*, 2015, **3**, 36, 9359-9368.

Gold catalyst formation on glass wool by chemical vapour deposition, *in preparation*.

Surface plasmon shifts of gold nanoparticle-metal oxide composites, *in preparation*.

Acknowledgements

I would like to thank my supervisors Professor Ivan Parkin and Professor Claire Carmalt for their patience and advice, Dr Peter Bishop and Dr Carmen Salcianu from Johnson Matthey for their valuable input and support, JM and EP-SRC for their generous funding, and all who I've met at UCL.

Specific thanks to Nuruzzaman Noor for guidance and chat about Chapters 2 & 3, Alaric Taylor for taking time out to work with me on Chapter 4, and Thomas Daley for his assistance and discussions that went into Chapter 5. I'm further grateful to Feyza Tunali, Joseph Bear and Sanjayan Sathasivam for some last minute data and images.

Contents

1	Introduction	29
1.1	Transparent conductors	29
1.1.1	Metals	31
1.2	Transparent conducting oxides (TCOs)	35
1.2.1	Electronic structure of TCOs	36
1.2.2	Conductivity of tin dioxide	38
1.2.3	Band gap and electronic structure	41
1.2.4	Fluorine doped tin dioxide (FTO)	43
1.2.5	Applications	44
1.3	Chemical vapour deposition of TCO materials	45
1.3.1	Aerosol-assisted chemical vapour deposition (AACVD)	49
1.3.2	Thermophoresis	50
1.4	CVD of SnO ₂ thin films	52
1.4.1	Precursors	53
1.4.2	Temperature	56
1.4.3	Carrier gas	58
1.4.4	Flow rate	59
1.4.5	Growth phase and structure	60
1.4.6	Doping SnO ₂	61
1.5	Gold nanoparticles	64
1.5.1	Optical properties and surface plasmon resonance	65
1.5.2	Synthesis	68
1.5.3	Applications	69
1.6	Composite nanoparticle metal oxide	70
1.6.1	Applications	70
1.6.2	Synthesis	71
1.7	Aims	74

2	Experimental and Analytical Details	75
2.1	Aerosol-assisted chemical vapour deposition set-up	75
2.1.1	Materials	76
2.2	Spray deposition	78
2.3	Analytical techniques	79
2.3.1	X-ray diffraction	79
2.3.2	UV-visible-IR spectroscopy	80
2.3.3	Filmetrics and Hall effect	80
2.3.4	Scanning electron microscopy	81
2.3.5	Transmission electron microscopy	83
2.3.6	Energy dispersive x-ray spectroscopy	83
2.3.7	X-ray photoelectron spectroscopy	84
2.3.8	Gas chromatography	85
3	Functional Composites of Gold Nanoparticles and Tin Dioxide	87
3.1	Introduction	87
3.1.1	Objectives	88
3.2	Experimental details	89
3.2.1	Precursor solutions	89
3.2.2	Deposition details	90
3.3	AACVD of SnO ₂	90
3.3.1	Phase and morphology	90
3.3.2	Optical and electronic properties	94
3.3.3	Summary	95
3.4	F doping and improving TCO properties	95
3.4.1	Phase and morphology	96
3.4.2	Optical and electronic properties	97
3.4.3	Summary	99
3.5	Investigation of auric acid depositions	100
3.5.1	Phase and appearance	101
3.5.2	Difference between top and bottom plates	101
3.5.3	Changing the auric acid concentration	103
3.5.4	High auric acid concentration depositions	106
3.5.5	Summary	108
3.6	One-pot solution AACVD of AuNP and SnO ₂ composites	109
3.6.1	Film appearance	109
3.6.2	Deposited phase	111

3.6.3	Surface morphology	117
3.6.4	Optical and electronic properties	120
3.6.5	Reaction pathway	124
3.6.6	Summary	125
3.7	Layering to make conductive AuNP and SnO ₂ composites . . .	126
3.7.1	FTO on Au	127
3.7.2	Au on FTO	131
3.8	Conclusion	135
4	Effect of Metal Oxide Character on the SPR in Composites with AuNPs	138
4.1	Introduction	138
4.2	Objectives	140
4.3	Experimental details	140
4.3.1	AACVD of composite films	140
4.4	Results	142
4.4.1	AuNP deposition	142
4.4.2	Metal oxide deposition	144
4.4.3	Ellipsometry and the determination of refractive index	150
4.4.4	SPR of gold nanoparticles and composites	153
4.5	Conclusion	156
5	Gold Nanoparticles on Silica Wool	158
5.1	Introduction	158
5.2	AACVD of gold onto glass wool	159
5.2.1	Results	160
5.2.2	Summary	169
5.3	Benzyl alcohol catalytic reaction	169
5.3.1	Experimental	170
5.3.2	Results	172
5.3.3	Summary	174
5.4	Spray deposition of gold nanoparticles onto glass wool	176
5.4.1	Experimental	176
5.4.2	Results	177
5.4.3	Summary	179
5.5	Conclusions	180

6	Conclusions	183
6.1	Summary of work	183
6.2	Forward look	186
6.2.1	Functional composites of gold and tin dioxide	187
6.2.2	Effect of metal oxide character on the SPR in composites of AuNPs	187
6.2.3	Gold nanoparticles on silica wool	187

List of Figures

1.1	Resistivity of evaporated gold films on bismuth oxide showing bulk resistivity at 200 Å, less than the mean free path of conduction electrons. ¹	32
1.2	Macroscopic and microscopic digital images of highly stretchable Ag nanowire network on Ecoflex being put under strain and schematic of stretching and current flow. ²	34
1.3	Tapping mode AFM scan of a PEDOT:PSS/Ag nanowire composite surface and height line profile. ³	35
1.4	Schematic energy-band model for Sn doped In ₂ O ₃ with low (left) and high concentrations of oxygen vacancies as developed by Fan and Goodenough. ⁴ It shows the Fermi level (E_F) increasing with significant doping into the conduction band (In 5s and 5p) through oxygen vacancies (V_O).	37
1.5	The relationship between electron density and mobility for various conducting materials. ⁵	38
1.6	(a) An interstitial site in SnO ₂ and the different possibilities of filling it with, (b) a neutral Sn interstitial, (c) a Sn ⁺⁴ interstitial, and (d) a neutral Sn interstitial with an O vacancy. ⁶	39
1.7	Schematic of the optical band gap (BG), Burstein-Moss (BM) shift and BG widening and narrowing due to many-body interactions. Adapted from literature. ⁷	42
1.8	Reactions and processes in chemical vapour deposition (adapted from Hitchman <i>et al</i> ⁸).	47
1.9	Arrows indicate the convection of gases upwards away from the heated substrate/bottom plate, affecting larger particles more strongly, transporting them towards the top plate and leaving smaller particles nearer the bottom plate.	51

1.10	Schematic showing a horizontal reactor and flow of dust used in calculations of thermophoretic effects. ⁹	52
1.11	Oscillation of conduction electrons due to absorption at resonant frequencies at the curved surface of metal nanoparticles called localised surface plasmon resonance.	66
1.12	Absorbance spectra of 9, 22, 48 and 99 nm sized gold nanoparticles normalised at their maxima, synthesised from auric acid with varying citrate concentrations. ¹⁰ Reprinted with permission from Size and Temperature Dependence of the Plasmon Absorption of Colloidal Gold Nanoparticles, S. Link and M. a. Sayed, The Journal of Physical Chemistry B, 1999, 103, 4212-4217. Copyright (1999) American Chemical Society.	67
1.13	TEM image of Au nanostars synthesised from H ₂ AuCl ₄ . ¹¹ . . .	69
1.14	A basic outline of the various routes used to make thin films with embedded nanoparticles (adapted from Walters <i>et al</i>). ¹² . .	72
2.1	Experimental set-up for aerosol assisted chemical vapour deposition.	76
2.2	Set up for spray deposition.	78
2.3	Schematic showing how satisfying Bragg's Law of $n\lambda=2d\sin\theta$ can generate coherent interference between the x-rays. The full length of the red line represents $2d\sin\theta$ and λ represents the wavelength of the x-ray (adapted from Diffraction Physics, by J. M. Cowley ¹³).	79
2.4	Diagram of the Hall effect where charge accumulation on a conductive thin film due to Lorentz forces from transverse applied electric and magnetic fields (adapted from Hall-Effect Sensors, Ramsden, E. ¹⁴).	81
2.5	Schematic of the scanning tunnelling microscope with positions of the backscattered and secondary electron detectors (adapted from online source ¹⁵).	82
2.6	Schematic showing the layout of the x-ray photoelectron spectroscopy set up and the mechanism by which the photoelectron is ejected due to incoming x-rays (adapted from Auger- and X-Ray Photoelectron Spectroscopy in Materials Science: A User-Oriented Guide, Hofmann, S. ¹⁶).	85

2.7	Component of a gas chromatography set up and a close-up of the flame ionisation detector (adapted from Basic Gas Chromatography, McNair, H. M. and Miller, J. M. ¹⁷).	86
3.1	XRD pattern intensities of SnO ₂ reference ¹⁸ and thin films deposited at 400, 450 and 500 °C from a precursor solution of MBTC (2 mmol) in 20 ml methanol with N ₂ (g) flowing at 2 L min ⁻¹	91
3.2	Percentage change in preferred growth of SnO ₂ deposited at 450 °C from a precursor solution of MBTC (2 mmol) in 20 ml methanol with N ₂ (g) at 2 L min ⁻¹	92
3.3	SEM images of SnO ₂ thin film deposited at (a) 400, (b) 450, and (c) 500 °C from a precursor solution of MBTC (2 mmol) in 20 ml methanol with N ₂ (g) flowing at 2 L min ⁻¹	93
3.4	Transmittance and reflectance spectra of SnO ₂ thin film deposited at 400, 450 and 500 °C from a precursor solution of n-butyltin trichloride (2 mmol) in 20 ml methanol with N ₂ (g) at 2 L min ⁻¹	94
3.5	XRD pattern and SEM image of fluorine doped tin dioxide from a 30% ammonium fluoride to MBTC solution deposited in air.	97
3.6	Percentage change in preferred growth of FTO deposited at 450 °C from a precursor solution of MBTC and NH ₄ F in methanol with air.	98
3.7	Transmission and reflection spectra of fluorine doped tin dioxide from a 30% ammonium fluoride to MBTC solution deposited with air.	99
3.8	Typical XRD pattern of AuNPs deposited from auric acid using aerosol-assisted chemical vapour deposition with cubic gold reference ¹⁹ for comparison.	101
3.9	Comparison of films deposited on bottom and top plate from the AACVD reaction of auric acid (0.02 mmol) in methanol (20 ml) with air (2 L min ⁻¹) at 450 °C. Shown here are SEM images and SPR maxima observed from the absorbance spectra at 545 nm (bottom plate) and 570 nm (top plate). The spherical shapes of the nanoparticles can be seen in the SEM images and the sizes were estimated from this.	103

3.10	Surface plasmon resonance maxima of a gold nanoparticles deposited on the top and bottom plate from various concentrations of 0.05, 1 and 2×10^{-2} mmol in 20 ml methanol at 450 °C.	104
3.11	TEM images of AuNPs deposited on the bottom plate from auric acid concentrations of (a) 2×10^{-2} , (b) 1×10^{-2} and (c) 0.5×10^{-2} mmol in 20 ml methanol.	105
3.12	Photographs of AuNPs deposited from a 20 ml solution of 6 mM auric acid in methanol. Even though the concentration of Au was high, it still maintained nanoparticulate nature as seen by the purple colour with transparency - note that text can be seen through it.	107
3.13	SEM images of gold deposited from an auric acid solution (6 mM) by AACVD. Images show showing island growth on the (a) bottom plate and large particle deposition on the (b) top plate.	108
3.14	Optical properties of a typical gold nanoparticle film: (a) transmittance, reflectance and (b) SPR absorption.	108
3.15	Photographs showing the top and bottom plate of a gold and tin dioxide composite film in transmittance and reflectance mode deposited at 450 °C from a one-pot solution of monobutyltin trichloride and auric acid in methanol.	112
3.16	Intensities of XRD patterns taken at 0, 1, 2, 3 and 4 cm away from the inlet of a bottom and top plate deposited from a precursor solution of MBTC (2 mmol) and auric acid (0.12 mmol) in methanol (20 ml) at 450 °C with N ₂ (g) carrier gas.	113
3.17	Points of 0, 4 and 8 cm away from inlet at which samples of bottom plate depositions at different temperatures from a one-pot precursor solution of auric acid and MBTC were measured for the values in Table 3.4.	115
3.18	XRD pattern of a film deposited at 500 °C with a precursor solution of MBTC (2 mmol) and auric acid (0.12 mmol) in methanol (20 ml) with N ₂ (g) carrier gas. This is an example of both the Au and SnO ₂ peaks showing. The peaks labelled are for SnO ₂ (*) and Au (°).	116

3.19	Photoemission spectra of the Sn $3d_{3/2}$ and $3d_{5/2}$ (left) and Au $4f_{5/2}$ and $4f_{7/2}$ binding energies of samples deposited at 400, 450 and 500 °C from a precursor solution of MBTC (2 mmol) and auric acid (0.12 mmol) in methanol (20 ml) with N ₂ (g) as the carrier gas.	116
3.20	SEM images taken from different regions on the bottom plate of AuNP:SnO ₂ composite deposited at 500 °C from a precursor solution of 5.6 at.% Au:Sn in 20 ml methanol at different distances from inlet of (a) 0 cm, (b) 4 cm and (c) 8 cm. EDX cannot determine if the white dot features in image (b) are nanoparticles because they are too small, however they are likely to be the uppermost features of the surface morphology.	118
3.21	SEM images of gold nanoparticles deposited on the top plate from a precursor solution of HAuCl ₄ ·3H ₂ O and BuSnCl ₃ with an atomic ratio of 0.06 in 20 ml methanol at (a) 500 °C, (b) 450 °C, and (c) 400 °C.	119
3.22	Optical properties from a deposition using a precursor solution of 5.6 at.% Au:Sn in 20 ml methanol at 500 °C. Transmittance (a), absorption (b) and reflectance (c) spectra correspond to bottom plate depositions. The observed ratios of deposited Au:Sn are labelled. The areas investigated as a function of distance from the inlet (I) 0 cm, (II) 4 cm and (III) 8 cm are labelled. (d), (e) and (f) correspond to transmittance, absorbance and reflectance top plate depositions with (I), (II) and (III) here referring to Au at.%.	123
3.23	Photographs of films showing the colour and transparency. (a) AuNPs deposited from auric acid, (b) FTO deposited from butyltin trichloride and ammonium fluoride, (c) FTO deposited as an overlayer above AuNPs and (d) AuNPs overlaid above FTO. . .	127
3.24	Comparing the properties of composite FTO (from a precursor solution of 30 at.% F:Sn) depositions on AuNP substrates from top and bottom plate positions. Different morphologies were observed from the SEM images of FTO on bottom plate (a) and top plate (b) and inserted are SEMs of the AuNP substrate. . . .	128
3.25	The (a) transmittance and reflectance spectra for FTO deposited on the bottom and top plate of a gold nanoparticle deposition. SPR absorptions were also observed as shown in (b).	130

3.26	Comparing the properties of composite films from AuNP top and bottom plate depositions onto a substrate of FTO (30 at.% precursor ratio of F:Sn). Different amounts and sizes of nanoparticles were observed from the SEM (a & b), slightly different XRD patterns (c & d) and preferred orientation (e & f).	132
3.27	SEM image of AuNPs (brighter parts of image) with decorative shapes on FTO.	133
3.28	XRD and optical spectra of AuNPs deposited onto fluorine doped tin oxide thin film. (a) XRD pattern is standard for all the FTO on AuNPs thin film. (b) The SPR absorption (arrows) of FTO overlaid above top and bottom plate gold nanoparticles.	134
4.1	Schematic showing the 2-step deposition process of layered AuNP and metal oxide composite formation.	141
4.2	The absorbances of AuNP depositions after different deposition durations (30-60 min) from a precursor solution of H ₂ AuCl ₄ (solution with dilute HCl) dissolved in methanol. As the additional heating duration is extended, the AuNP film transforms from a rough surface to nanoparticles resulting in a narrowing of the SPR absorption. The general flat absorbance between 600-1000nm develops into an SPR peak and maximum as the deposition time increases.	143
4.3	SEM and TEM images showing the AuNPs deposited using a precursor solution of 0.02 mmol H ₂ AuCl ₄ at 450 °C.	144
4.4	X-ray diffraction patterns of various metal oxides deposited using AACVD.	146
4.5	SEM images of various metal oxides deposited using AACVD.	147
4.6	Side-on SEM images of the various metal oxides deposited using AACVD.	148
4.7	Transmittance and reflectance spectra of various metal oxides deposited using AACVD.	149
4.8	Simple diagram showing the basic model used to calculate ψ and δ from ellipsometry measurements	150
4.9	Refractive index, n , extinction coefficient, k , and the observed and fit of ψ and δ from ellipsometry measurements.	152
4.10	The shifts in SPR absorption before and after forming composites with various metal oxides.	154

4.11	Graph showing the SPR shift of composites formed with gold nanoparticles and various oxides: Al ₂ O ₃ , MgO, Ga ₂ O ₃ , ZnO, SnO ₂ and TiO ₂ and the corresponding refractive indices as measured from the individual metal oxides.	156
5.1	Aerosol-assisted chemical vapour deposition set up of gold nanoparticle deposition onto glass wool.	159
5.2	Photograph of gold particles deposited by aerosol-assisted chemical deposition from auric acid (1 mmol) in 100 ml methanol with air (4 Lmin ⁻¹) at 350 °C.	161
5.3	SEM of blank glass wool.	161
5.4	XRD pattern of AuNPs deposited onto glass wool showing cubic Au reflections with reference. ¹⁹	162
5.5	Differences of gold nanoparticles deposited onto glass wool by aerosol-assisted chemical deposition from auric acid (0.2 mmol) in 50 ml methanol with air at (a) 3 and (b) 4 Lmin ⁻¹ at 350 °C.	164
5.6	Secondary and backscattered electron SEM images of AuNPs deposited on glass wool showing a more agglomerated and larger particle sizes from the orange areas using and smaller individual gold nanoparticles from the purple areas. The AuNPs are imaged as whiter and lighter shades on the backscattered images. The AuNPs were synthesised from an aerosol-assisted chemical deposition using a precursor solution of auric acid (1 mmol) in 100 ml methanol with air (4 Lmin ⁻¹) at 350 °C.	166
5.7	TEM images showing agglomerated and individual gold nanoparticles that were deposited by aerosol-assisted chemical deposition from auric acid (1 mmol) in 100 ml methanol with air (4 Lmin ⁻¹) at 350 °C.	168
5.8	Reaction scheme showing the oxidation of benzyl alcohol to benzaldehyde and further oxidation to benzoic acid and benzyl benzoate.	170
5.9	The reaction vessel showing the reaction solution and AuNP (gold nanoparticle deposited) glass wool inside it being stirred by a mechanical stirrer. The temperature probe informs the power of the heating mantle, and the microsyringe is inserted into the reaction vessel in order to extract samples for gas chromatography (GC) measurements.	172

5.10	Gas chromatography signals of mixture prior to reaction showing the time of flight peaks of the different components.	173
5.11	Conversion rate of benzyl alcohol oxidising to benzaldehyde with tert-butyl hydroxyperoxide catalysed by gold nanoparticles immobilised on glass wool with an orange colouring.	175
5.12	Secondary (a) and backscattered (b) SEM image of Corning glass wool.	177
5.13	Photograph of gold nanoparticles deposited using a spray deposition method with (a) 0.02 mmol and (b) 0.01 mmol of auric acid in a mixture of methanol (5 ml) and acetone (20 ml).	178
5.14	Scanning electron microscope image of gold nanoparticles (confirmed by EDX) on glass wool deposited by a spray deposition method.	179
5.15	Transmission electron microscope image of gold nanoparticles on glass wool deposited by a spray deposition method.	180

List of Tables

2.1	The materials investigated in this thesis and their deposition details.	77
3.1	Precursors used for the relevant materials.	89
3.2	Different concentrations of auric acid in methanol used to deposit the gold nanoparticles and their corresponding SPR maxima and sizes determined from SEM images.	101
3.3	Different compositions of one-pot precursor solutions for the deposition of gold and SnO ₂ thin films. All depositions were carried out using precursor solutions of auric acid in varying concentrations with butyltin trichloride (2 mmol) in methanol (20 ml).	110
3.4	Data measured at from different points of 0, 4 and 8 cm away from the inlet (Figure 3.17) on the bottom plate of films deposited from a 20 ml methanolic solution of 100 mM MBTC at 500 °C and together with 6 mM HAuCl ₂ at 400, 450 and 500 °C. Deposited Au:Sn atomic ratios were determined using EDX and the corresponding SPR maximum where existent. . .	114
3.5	Electronic properties of FTO on AuNPs layered thin film. Precursor solutions in methanol (20 ml) were composed of 30 at.% F:Sn for FTO and 2×10^{-2} mmol HAuCl ₄ (1 mM) for AuNPs. . .	130
3.6	A comparison of the preferentially orientated planes of SnO ₂ and FTO deposited using AACVD with MBTC and NH ₄ F. . .	136
4.1	Deposition details for the various metal oxides. All precursor solutions were made with 20 ml methanol, with the exception of titanium ethoxide which was dissolved in 15 ml toluene. All depositions occurred at 450 °C.	142

4.2	Calculated refractive indices of various metal oxides modelled from ellipsometric data.	153
4.3	Shift in SPR of AuNPs before after composite formation with metal oxide.	155
5.1	Chemicals in the reaction mixture for the catalytic oxidation of benzyl alcohol.	171
6.1	Materials that have been deposited and described for this thesis and their selected properties.	184

List of Symbols, Acronyms and Abbreviations

μ	mobility
n	carrier concentration
ρ	resistivity
AACVD	aerosol-assisted chemical vapour deposition
acac	acetylacetonate
AES	auger electron spectroscopy
AFM	atomic force microscopy
APCVD	atmospheric pressure chemical vapour deposition
at. %	atomic percent
AuNP	gold nanoparticle
BG	band gap
BM	Burstein-Moss
CBM	conduction band minimum
DFT	density functional theory
DMTC	dimethyltin dichloride
EDX	energy dispersive x-ray spectroscopy
EPR	electron paramagnetic resonance

FTO	fluorine doped tin dioxide
GC	gas chromatography
IR	infrared
ITO	tin doped indium dioxide
LDA	local density approximation
MBTC	monobutyltin trichloride
SEM	scanning electron microscopy
SPR	surface plasmon resonance
TCO	transparent conducting oxide
TEM	transmission electron microscopy
TMT	tetramethyltin
TTC	tin tetrachloride
V_O	oxygen vacancies
XRD	x-ray diffraction

Chapter 1

Introduction

This thesis will present results relating to the synthesis of gold nanoparticles and their composites with metal oxides. The main synthesis procedure used was aerosol-assisted chemical vapour deposition (AACVD). SnO₂ and the F doped analogue was the primary metal oxide synthesised and investigated for its transparent conducting character. The optical properties, specifically the surface plasmon resonance absorption, of the gold nanoparticles (AuNPs) were observed and analysed. The shifts in SPR due to the nanoparticles being in a composite with dielectric metal oxides will be investigated through the optical analysis of layered AuNP composites with varying metal oxides. AuNPs will also be deposited onto another silica substrate, glass wool, and shown to be catalytically active.

1.1 Transparent conductors

A transparent conducting material presents us with the unique spectral and electrical properties of transparency over the visible region and high conductivity, which really lend themselves as components in modern optoelectronic devices such as flat panel displays and solar energy technology.²⁰ According to

Haacke's review in 1977,²¹ the first reported transparent conductors were of very thin films of silver and platinum as electrodes in selenium photoelectric cells.^{22,23} However, for current practical applications, transparent conducting oxides (TCOs) dominate the field due to the relative ease of their synthesis and robustness.²¹

Conductivity in a wide band gap semiconductor is usually achieved by *n*-type doping of a metal oxide, where the dopant donates electrons into the conduction band. Transparent and conductive In₂O₃:Sn (tin doped indium oxide or ITO) thin films were reported during the mid-1960s,²⁴ first used for reducing heat losses from sodium lamps,²⁰ it continues to be the one of the most widely used and highest standard TCO. The addition of dopants in the metal oxide matrix increases the number of charge carriers in the system, not only does this improve the conductivity but also enables the material to reflect light from the IR region. These features of TCOs can be exploited for low emissivity windows or as the electrode layer transferring electrons to the electrochromic layer of an electrochromic window.²⁵ More details into the synthesis and applications of TCOs will be discussed in Section (1.2).

TCO properties are commonly measured and compared using their transmittance and resistance. T , the optical transmittance is related to α , the optical absorption by

$$T = \exp(-\alpha t).$$

Sheet resistance, R_{sh} , is related to the inherent resistivity, ρ and film thickness, t by

$$R_{\text{sh}} = \rho/t$$

and as t increases both T and R_{sh} decrease with differing proportions.

1.1.1 Metals

Metals are a logical material to approach in terms of conductivity for TCO applications, however these materials possess optical reflectivity that need to be overcome in order for them to be suitable for use as transparent conductors. The plasma present due to metallic bonding results in the majority of the visible light wavelengths being reflected from metal surfaces. Absorption of certain bands in the visible produces coloured metals, such as yellow for gold and red orange for copper. The problem of optical transparency in metal films can be overcome if the thickness of the film were to be lowered to less than 50 nm, preferably below 10 nm. And so, the success of generating a metal film with low thicknesses reliably is an important factor for synthesis since with increasing thickness there is an exponential decrease in transparency.^{26,27}

Normally metal thin film growth begins with island formation at low concentrations, and depending on the wettability of the surface, bridges will start to form between the islands as they coalesce. When only islands are present, the conductivity of the film is low or non-existent, and as soon as bridges form, connection pathways for carriers also start to form and the conductivity properties become similar to bulk properties, with increasing conductivity as the thickness increases.²⁸ If bridges and carrier pathways can be encouraged to grow at lower concentration, ultra-thin metal films (UTMF) can be formed, resulting in higher optical transparencies. The tendency for metal islands to coalesce is related to the surface roughness of the film and depends on the nucleation and growth kinetics of the metal films.²⁶ In transparent electrodes, the metal oxide component can be used as a seed layer to improve the chemical and physical interactions between the metal and substrate. By varying the metal oxide, the wettability of the metal to the surface can be adjusted, and so potentially reducing the thickness at which the thin film form carrier path-

ways.²⁹

Diffuse (inelastic) electron scattering can occur on the surface of thin metal films, reducing the mean free path, and thus resulting in higher sheet resistances when compared to the bulk material.³⁰ According to Sondheimer³¹ and Fuchs³² the conductivity only increases when the thickness of the film exceeds the carrier mean free path, and so the limit in resistivity is purely a geometrical effect. Apart from diffuse scattering, it is thought that strain and impurity also play important roles in determining the conductivity of a thin film. However, early experiments have shown that the relationship between film thickness, the mean free path of the electrons and conductivity is not simple and does not obey an exact rule. At room temperature the mean free path for gold is about 620 Å, but the resistivity does not increase until the film is less than 200 Å (Figure 1.1),¹ where there may be specular (elastic) scattering occurring from the surface.

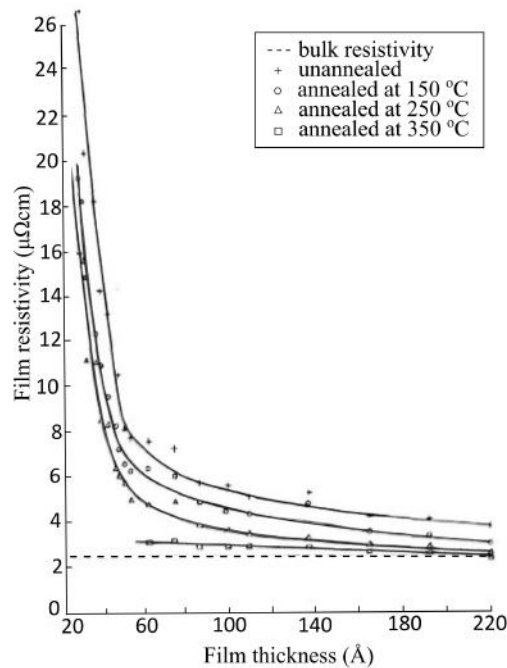


Figure 1.1: Resistivity of evaporated gold films on bismuth oxide showing bulk resistivity at 200 Å, less than the mean free path of conduction electrons.¹

Macrostructures can also be used to play with the observed transparency of metals. It has been proposed with effective medium theory that metals with a porous structure can be transparent to wavelengths larger than its pores.³³ Porous Pt with thicknesses of up to 30 nm have been incorporated into a *p*-type In-P system and been shown to remain transparent, even adding functionality as the Pt metal could catalytically improve the solar to hydrogen conversion.³⁴ Attempts to increase the thickness of porous Au films to 300 nm by forming microcylindrical structures were unsuccessful in preserving the visible transparency, but maintained infrared (IR) transparency which is normally not present in a homogeneously deposited Au film of the same thickness.³⁵

Another solution to overcome the optical restraints and maintain electrical conductivity is to create thin films of metal nanowire meshes. Solution processed Ag nanowires with a modal length of around 8 μm can result in films which have solar transmittance of 85% with sheet resistance of $10 \Omega/\square$.³⁶ The mechanical nature of the reported Ag nanowires means they can be bent up to a 4 mm radius without any effect on the sheet resistance. The solution deposition and lower temperature of synthesis also make this an attractive environmentally-friendly option when compared to traditional TCOs. Extending the nanowires to over 100 μm stretches the network to over 460% strain without losing its conductivity as shown in Figure 1.2.²

Even though flexible, metal nanowire meshes have problems similar to metal nanoparticles,^{37,38} with adhering to glass substrates, rubbing off easily and failing the Scotch tape test.³⁹ By embedding Ag nanowires in a polymer matrix the adherence problem is not only solved but the roughness of the mesh is overcome making the material more electronically connected and compatible with devices.^{3,40} Transparent electrodes made from a Ag nanowire composite in a conducting polymer has even been shown to outperform the ITO analogue (Figure 1.3 a).³

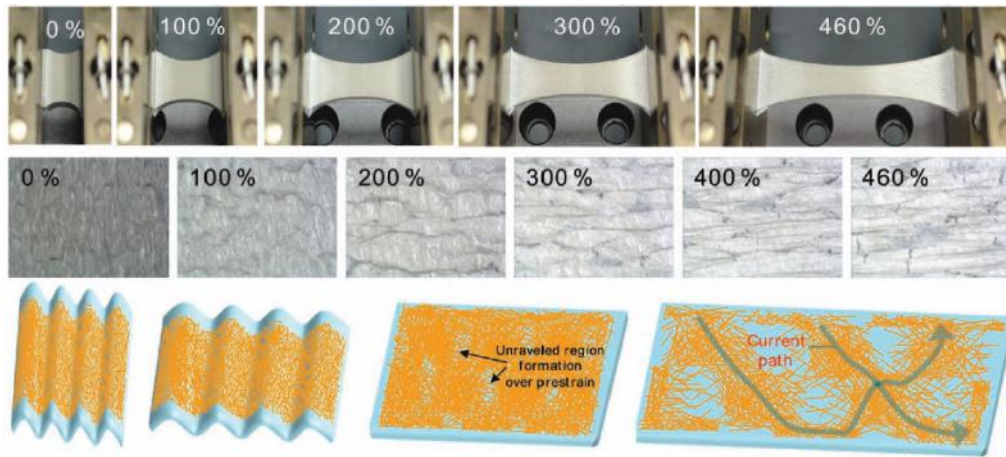


Figure 1.2: Macroscopic and microscopic digital images of highly stretchable Ag nanowire network on Ecoflex being put under strain and schematic of stretching and current flow.²

Metal patterning by laser perforation of a thin silver film was tested in silicon oxide solar cells with the idea of improving the conductivity with better surface contacts, however the best performing Ag contact (18% coverage) only achieved a current density of 30.7 mA/cm^2 compared to an ITO contact measuring in at 34.2 mA/cm^2 .⁴¹ A similar technique involves the formation of carbon nanotube meshes, which also look promising for flexible devices, however the optoelectronic properties are not yet comparable with current TCO standards.⁴²⁻⁴⁴

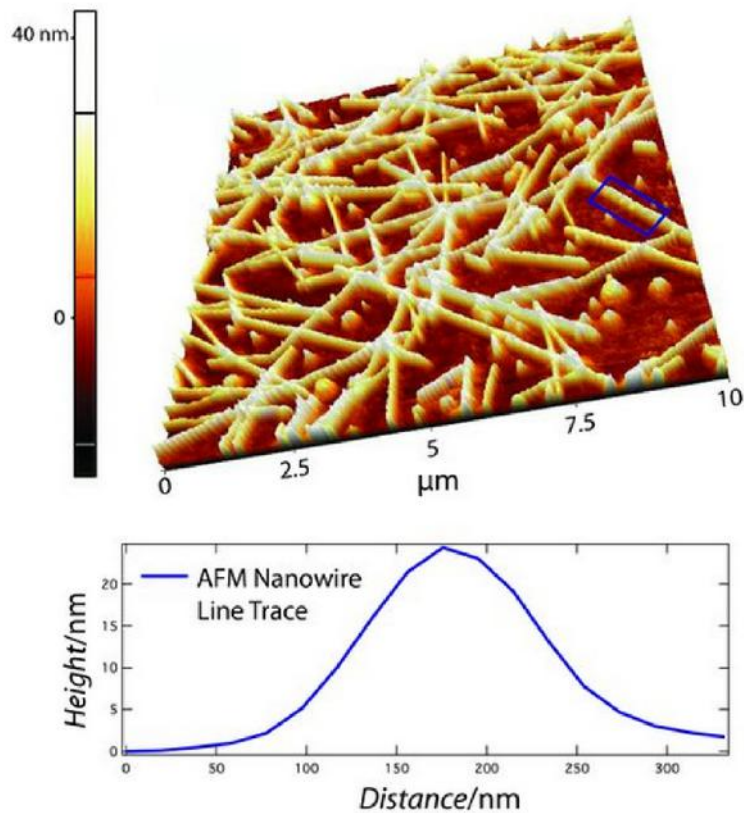


Figure 1.3: Tapping mode AFM scan of a PEDOT:PSS/Ag nanowire composite surface and height line profile.³

1.2 Transparent conducting oxides (TCOs)

Instead of working to improve the transparency of metallic materials, some metal oxide semiconductors that already possess optical transparency can, with the right synthesis also display relatively high electronic conductivity. This class of materials, called transparent conducting oxides (TCOs), having the coexistence of optical transparency and conductivity properties, was first reported in the form of cadmium oxide (CdO) around 60 years ago.⁴⁵

CdO is a promising TCO with a high carrier mobility resulting in a low resistivity of $2 \times 10^{-4} \Omega\text{m}$, however the moderately narrow band gap of around 2.3-2.5 eV means absorption in the visible wavelength region results in materials that are not fully transparent.⁴⁶ By forming a composite with another

TCO, such as ZnO which is transparent, the properties of the two oxides can be mixed. As expected, a higher Cd:Zn ratio content in the composite decreased the resistivity but at the same time also decreasing the transmittance in the visible.⁴⁷ Doping with another metal, Al manages to increase the carrier concentration but to detrimental optical effect since the presence of Al increases ionized impurity scattering and retards the mobility, furthermore the band gap was reported to narrow with increasing Al content.⁴⁸ Instead of using CdO as a factor to increase the conductivity of another metal oxide system, researchers have tried to utilise the Burstein-Moss phenomenon (see Section 1.2.3) to increase the band gap of CdO and make it more transparent.⁴⁹ Lower levels of the conduction band in CdO can be populated with excess electrons with Ti doping and an increase in band gap was observed from 2.54 eV to 3 eV when moving from undoped to 5 at.% Ti.⁴⁹ The conductivity does not however increase in line with the carrier concentration, and the authors suggest that the presence of Ti dopants introduced stress fields in CdO which reflect free carriers, reducing the mobility from 591 to 202 cm²/Vs when comparing between undoped and 5 at.% Ti doped CdO.

1.2.1 Electronic structure of TCOs

Fan and Goodenough's band structure of Sn doped In₂O₃ (ITO) derived from x-ray photoemission studies provided an early basic understanding of the band structure of a TCO material.⁴ Oxygen vacancies (V_O) and Sn interstitials both provide additional impurity donor levels just under the conduction band minimum (CBM). At high donor concentrations the impurity levels overlaps the CBM, increasing the Fermi level (see Figure 1.4) and creating a degenerate current carrying electron gas.⁵⁰

Following this the conductivity can be characterized by the itinerant elec-

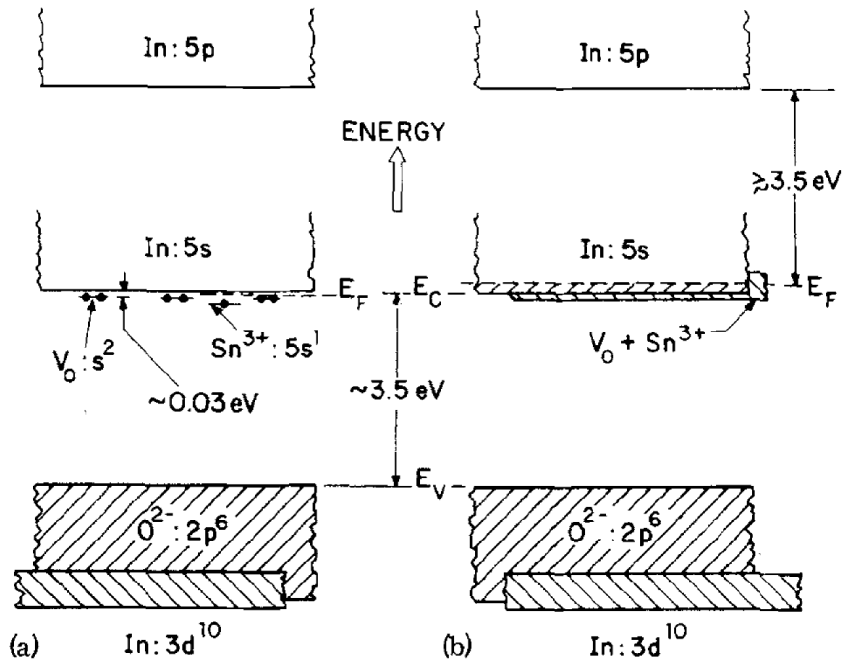


Figure 1.4: Schematic energy-band model for Sn doped In₂O₃ with low (left) and high concentrations of oxygen vacancies as developed by Fan and Goode-nough.⁴ It shows the Fermi level (E_F) increasing with significant doping into the conduction band (In 5s and 5p) through oxygen vacancies (V_O).

trons and treated with the electron-gas model of solids.⁵ The resistivity will then follow the equation:

$$\rho \approx (ne\mu)^{-1}$$

where ρ is the resistivity, n the carrier concentration, e the electronic charge and μ the mobility of the charge carriers. Mobility, μ is directly proportional to the free carrier resistivity relaxation time, τ and inversely proportional to the carrier effective mass, m^* :

$$\mu = \frac{e\tau}{m^*}$$

The relationship between the electron mobility and electron densities of different materials can be seen in Figure 1.5. Metals have both high μ and n , semimetals low μ and high n and semiconductors high μ and low n . TCOs occupy the space between semiconductors and metals with metal-like conduc-

tivity and insulator-like transparency. Further details on the origin of the conductivity of SnO_2 , the main TCO system focused here in this thesis, is discussed in Section 1.2.2.

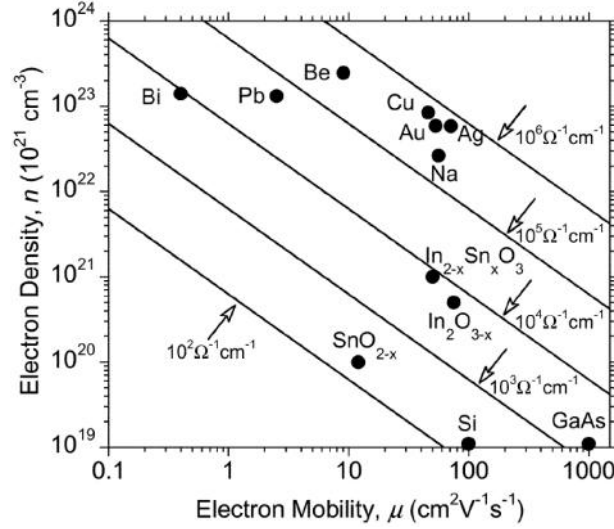


Figure 1.5: The relationship between electron density and mobility for various conducting materials.⁵

1.2.2 Conductivity of tin dioxide

Introduction of defects into a metal oxide lattice will lead to defect levels in the band gap which when at a high enough density will start contributing the electrical conductivity character of the host material.⁵¹ Tin dioxide can be made conducting very easily without extrinsic doping. The origin of this inherent conductivity was put down to the presence of oxygen vacancies, native point defects, which can act as donors or acceptors.^{52–55} However, based on DFT-LDA calculations Kılıç and Zunger suggested that it was actually intrinsic defects in the form of +4 Sn interstitials that contribute to the conductivity through the formation of conductive shallow donor states, rather than O vacancies (V_O) which they say form deep non-conductive levels.⁶ The different interstitial sites they considered are shown in Figure 1.6. Electrons around the Sn orbitals are very weakly bound, thus the formation energy of Sn interstitials

are low. The addition of +4 Sn interstitials causes a change in bond lengths to similar distances that is found in SnO, another stable tin oxide structure. Oxygen vacancies were also found to have low formation energies, becoming more favourable in the presence of Sn interstitials because of a strong interdefect attraction between them, explaining their detected presence in conducting SnO₂ samples. The DFT-LDA modelling method used by Kılıç and Zunger for calculating the formation energies of various defects have been questioned, and instead calculations are said to be more accurate when using the generalized gradient approximation (GGA) + U , as it reportedly can acquire the correct band gap and consequently more accurate defect formation energies. (GGA) + U studies concluded instead that interstitial Sn sites do have high formation energies.⁵⁶

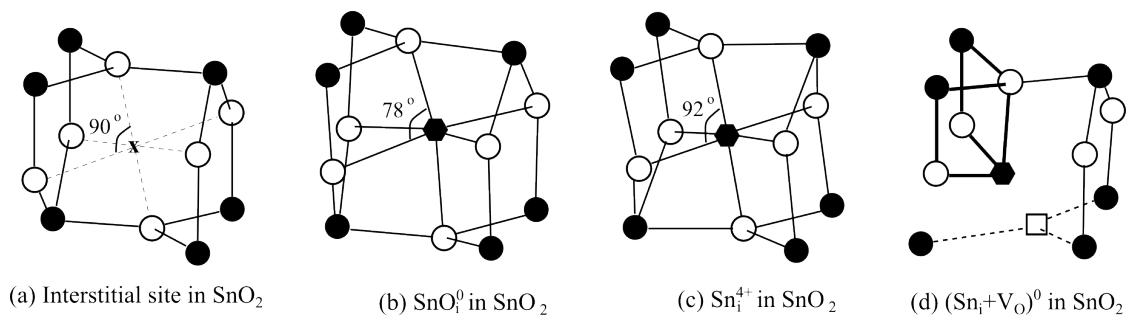


Figure 1.6: (a) An interstitial site in SnO₂ and the different possibilities of filling it with, (b) a neutral Sn interstitial, (c) a Sn⁺⁴ interstitial, and (d) a neutral Sn interstitial with an O vacancy.⁶

Electron paramagnetic resonance (EPR) can detect spins of unpaired electrons within systems. EPR studies of SnO₂ have identified a singly ionized resonance which has been attributed to V_Os, since the signal intensity was found to decrease in an oxygen environment and increase with increasing conductivity in a hydrogen environment.^{57,58} Instead of assigning this state to V_Os, and because of the lack of confirmation from other forms of experimental detection, some researchers have also assigned the defect, which contributes to intrinsic SnO₂ conduction, to interstitial hydrogen.⁵⁶ Furthermore, hydrogen has been

reported to contribute to a shallow donor state and therefore increasing the number of charge carriers in ZnO, In₂O₃ and SnO₂.⁵⁹⁻⁶¹ Some researchers have found unintentional extrinsic doping of Cl, originating from a chlorinated tin precursor being used in synthesis,⁶² which is also believed to have led to increases in conductivity levels of SnO₂.^{63,64}

To describe the effects of metal cation defects on the conductivity of SnO₂ films, the small-polaron hopping conduction model was proposed since the defects that contribute to conduction also cause disorder as it moves through the system.^{55,65} To investigate this, SnO₂ was doped with Li⁺, Cd²⁺, Al³⁺ (*p*-type), Ti⁴⁺ (same valency), Nb⁵⁺, and W⁶⁺ from a hydrothermal method. The authors concluded that ionization energy values of each individual defect will affect the position of the defect levels. Conductivity was found to decrease for the Li, Cd, Al and Ti doped films, but increase for Nb and W doped films. Decreased conductivities were thought to be due to V_Os formed to charge compensate some of the *p*-type cation dopants (Li, Cd and Al). The Ti⁴⁺ dopant was believed to have been reduced to a Ti³⁺ acceptor state which can stably form in SnO₂ and neutralise any conductivity. When SnO₂ was doped, it was found that the hopping energy was lowered due to a change in dielectric constant, and this can be used to describe the electron transport properties of defect-rich metal oxide semiconductors.^{65,66}

Scattering and mobility

The resistance of a conducting thin film can be decreased simply by increasing the thickness of the film, however for a TCO material this method of increasing conductivity is limited by the increase in scattering and absorption of light as the film thickness increases. For polycrystalline thin films, scattering can occur on the grain boundaries.⁶⁷ Knowing the dominant crystal structure is important in trying to elucidate transport properties limited by trapped cen-

tres at the grain boundaries. The (200) plane of SnO₂ is predicted to have no deep lying trap levels at grain boundaries and this is correlated to higher conductivities.⁶⁸ Grain boundary mechanisms can be ignored if the grain sizes are larger than the electron mean free path. At higher deposition temperatures, with larger resultant crystallite size and higher crystallinity, grain boundary resistance effects are negligible.⁶⁹

The scattering mechanisms and frequency affects the final electron mobility of the material. In single crystals electrons can be scattered by phonons, and when doped intrinsically at high levels from the ionized dopant atoms. Non-metal dopants, such as F, can therefore increase n without compromising the optical performance. Recently, it has been suggested that for Mo doped In₂O₃ high mobilities can be retained even for highly doped systems overcoming the impurity scattering frequently associated with these systems. In order for this to occur, the amount of hybridization between the dopant states and the host lattice must be low at the conduction band minimum.⁷⁰

There is a wealth of published research on SnO₂ TCOs, synthesised in a large variety of ways, so there is that there exists a large variation in the reported electronic and optical constants some of which will be highlighted in the discussion.⁷¹

1.2.3 Band gap and electronic structure

The band gap (BG) in a semiconductor refers to the gap between the valence band maximum (VMB) and conduction band minimum (CMB). TCOs are transparent because the energy size of the gap is larger than that for visible light. They become conducting when the conduction band is filled with enough electrons, n -type, or if there are mobile holes in the valence band, p -type, which will then have an effect on the BG structure.

When lower levels of the conduction band are filled by extrinsic or intrinsic doping, the measured optical band gap can be seen to increase and this is called the Burstein-Moss shift (Figure 1.7).^{72,73} The Burstein-Moss shift is compensated by band gap narrowing due to many-body interactions, which causes shifts in the valence and conduction bands.⁷ For an n -doped semiconductor far above the Mott critical density, where the density of electrons are high enough to become conducting, an effective mass model can be used to interpret the data that takes into account the electron-electron and electron-impurity scattering.⁷⁴ The Burstein-Moss shift can be correctly calculated for SnO_2 using this model, with a further consequence of band shape distortion with increasing degrees of degeneracy.⁷

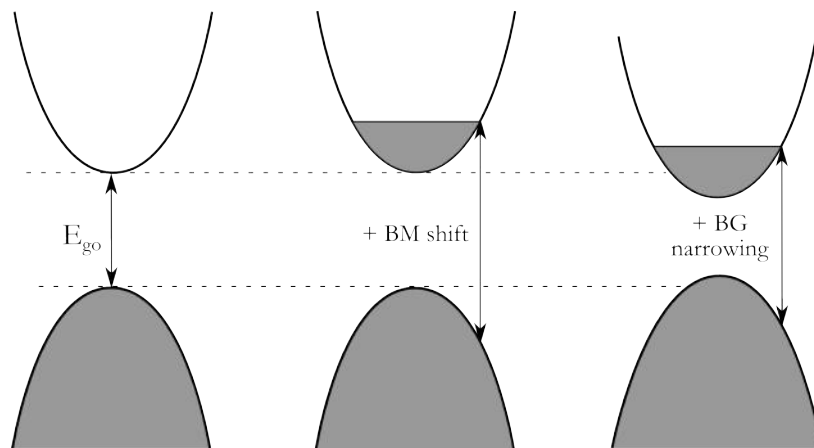


Figure 1.7: Schematic of the optical band gap (BG), Burstein-Moss (BM) shift and BG widening and narrowing due to many-body interactions. Adapted from literature.⁷

At the edge of the optical band gap an exponential tailing can be observed which is referred to as the Urbach tail caused by which is due to deformation at high carrier concentration.⁷⁵ Impurity, disorder and defects in structure leads to local electric fields that affect band tails.⁷⁶

1.2.4 Fluorine doped tin dioxide (FTO)

A common way to improve SnO_2 's conductivity is through fluorine doping to make fluorine-doped tin oxide (FTO). F is a favourable substituent because of its comparable size to the O^{2-} , similar bond energy of Sn-O and Sn-F and lack of contribution to ionic scattering. Lab and large scale depositions of SnO_2 or FTO normally yields polycrystalline thin films. Different facets and the orientation of planes can influence the observed optoelectronic character of the material. (110), (211) and (301) planes have trapping states at the surface which hinders conductivity, while films with high (200) facing crystallites should have the same transport properties found in thicker films as the (200) plane is said to be of higher density.⁷⁷ Therefore many instances of FTO with high mobility character have been found to deposit with a preference for the SnO_2 (200) plane.^{69,78,79}

At very high levels of F doping, an Sn-F complex is predicted to form from X-ray photoelectron spectroscopy (XPS) results, as the F starts populating the V_{O} sites, decreasing carrier concentration and mobilities.⁸⁰ If F is substituted onto an V_{O} there is expected to be a drop in carrier concentration, whereas if the F substitutes the O site, an increase in carrier concentration should be observed. Excess doping can lead to F sitting at interstitial sites, becoming an electron acceptor and increasing lattice disorder, therefore hindering conductivity. As F dopants were introduced and increased in the spray pyrolysis of SnO_2 , an initial drop in carrier concentration was observed, before the expected increase and finally reaching a saturation point when precursor solutions of F:Sn at 250 at.% was used.⁷⁷

As has been shown by Auger Electron Spectroscopy (AES) studies, F has a high desorption rate induced by the electron beam,⁸¹ therefore elemental analysis of the film surface will probably prevent correct assessment of the F content.

In general, the dopant amount and inherent size of F in FTO is normally very low that it is hard to detect and measure using conventional lab techniques.⁸²⁻⁸⁴

1.2.5 Applications

TCOs play an important role in the structure of solar cells. The basic concept of a solar cell is the generation of electricity from the absorption of a photon which promotes a carrier from the ground to excited state. Some way is then needed to extract or supply carriers to or from these states. In the two more popular types of solar cells, silicon *p-n* junction and dye sensitized solar cells, TCO materials were used as electrodes to extract the electrons from the light absorbers.⁸⁵ Anti-reflection properties can also enhance the effect of photoabsorbers by making sure the maximum amount of light gets through to the photoactive material.⁸⁶ A scattering film which gives the appearance of “milky” is advantageous for solar cell applications as it allows the average path length of the light in the absorber to be longer. The main way to increase the scattering is to generate roughness in a film⁸⁷ and when measured by diffuse scattering only 5% is needed for optimized solar energy capture.⁸⁸ This scattering is called haze and is measured by:

$$\text{haze\%} = T_{\text{diff}} / (T_{\text{diff}} + T_{\text{spec}}) \times 100$$

where T_{diff} is diffuse scattering and T_{spec} is specular transmission.

Doped with the right element, electrochromism, the changing of the colour of a material due to charge, can be displayed in SnO₂. Sb doped SnO₂ weakly absorbs in the visible and near IR due to intraband absorptions of conduction band electrons.⁸⁹ When applying a potential to Sb doped SnO₂, the intensity of absorption in the visible and IR region changed according to applied potential.^{90,91} Sb:SnO₂ is blue at positive potentials and by decreasing the applied

potential from $E = +1.4$ V to $E = +0.2$ V there was an observed increase in absorption. By further decreasing to a negative potential of $E = -0.4$ V, increases in absorption was also observed near the UV region indicating the introduction of other absorption processes. Degradation of system electrodes and the electrolyte occurs outside the range of $E = +1.4$ V and -0.4 V, but within this range the electrochromic effect can be cycled without losing efficiency or colouration up to 10^6 times.⁹¹

Large scale depositions of FTO as low 'e' architectural windows, coatings with reflectance in the IR, makes FTO one of the most widely deposited TCOs. TCOs are also used in devices where transparent electronics are essential such as touch screens, flat panel displays and transistors.

1.3 Chemical vapour deposition of TCO materials

Reports in literature of transparent conducting SnO_2 thin films have shown that it can be synthesised by many techniques such as spray pyrolysis, chemical vapour deposition (CVD), sputter coating amongst others.⁹² A variant of chemical vapour deposition (CVD) is the method of choice for making thin films industrially on-line for glass coatings and, as shown in this thesis, can be scalable to smaller laboratory experiments. The results from lab-scale CVD experiments are a valuable tool for understanding and predicting the reactions that might occur in a larger scale reactor. In this thesis, aerosol-assisted chemical vapour deposition (AACVD) was used to deposit metal oxides, gold nanoparticles (AuNPs) and composites comprised of both onto glass substrates.

Chemical vapour deposition of thin films are labelled so because the *chemical reactions* between the *vapourised* precursors begin to occur in the gas phase

or on the substrate, before further reacting and leading to *deposition* of thin films.⁹³ This is different to physical vapour deposition (PVD) which involves adsorption of atoms or molecules onto the surface prior to reacting i.e. if the precursor or droplets adsorb onto the surface before reacting. Pilkington introduced industrial "on-line" atmospheric pressure CVD (APCVD) on architectural glass, the most successful coating being FTO low emissivity coatings. Spray pyrolysis has been used to make SnO₂ thin films and the precursors in solution are sprayed onto a heated substrate.⁹⁴⁻⁹⁶ If the droplets do not react in the gas phase and land on the surface before evaporation or initial reactions, it is classed as a PVD process. Sputtering is another example of a PVD technique whereby the precursors in the form of atoms are generated and accelerated towards a substrate where it reacts to form thin films.

Reactions involved in the CVD mechanism are complicated and involve many factors such as the temperature, carrier gas, precursor, and flow rate. Varying any of these factors change the concentration of precursors present in the gas phase, residence time of reactants on the surface, and consequently influence the nature of reactions occurring both in the gas phase and on the surface. Specifically, the formation of a thin film depends on adsorption of at least one reactant on surface, formation of critical nuclei by surface reactions preceded by surface diffusion and formation of activated complexes. Any waste gaseous products undergo desorption of gaseous with or without some surface migration. Figure 1.8 show the key steps in a CVD that mainly characterised by the following processes:

- i Vapour flow into the reactor followed by the evaporation and of the precursor reagents
- ii Gas phase reactions of the precursors produce reactive intermediates and by-products
- iii Reactants move by mass transport onto the surface

- iv Reactants then adsorb onto the surface
- v Reactants can diffuse across the surface and further react to forming the thin film
- vi Surface products desorb and move by mass transport away from the reaction area

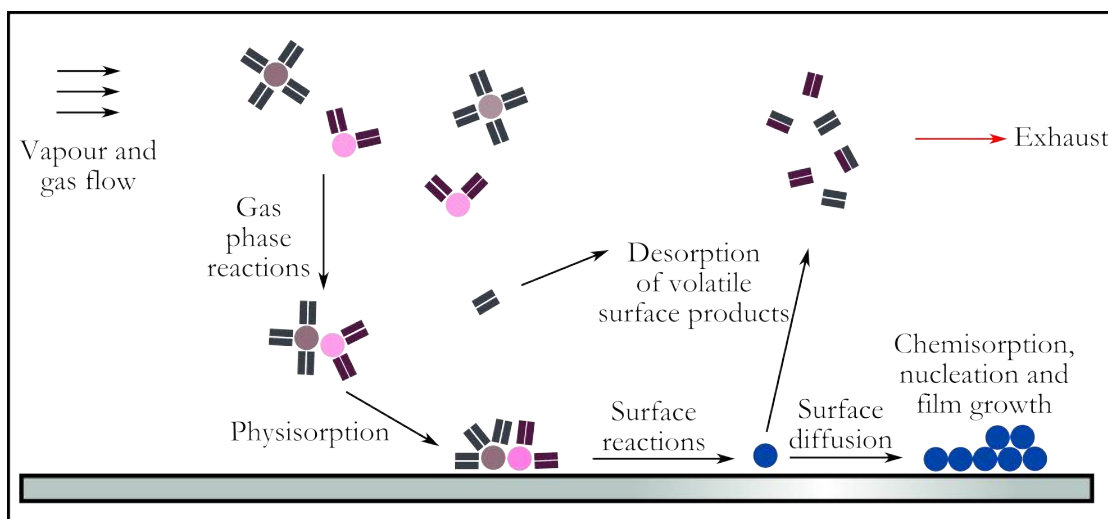


Figure 1.8: Reactions and processes in chemical vapour deposition (adapted from Hitchman *et al*⁸).

CVD reactions are traditionally initiated through thermal processes, as it is with the AACVD set up used in this thesis. As the temperature of the reactor increases, the growth rate increases in relation to the Arrhenius equation.⁹⁷ However, after a certain temperature the growth rate becomes dependent on the mass transport of reagents to the surface and is said to become mass transport or diffusion-controlled growth.^{72,98} If gas phase reactions occur too early, it may mean that the product is formed as a powder rather than a thin film. In the CVD of SnO_2 , it is unlikely that there homogenous gas-phase volume reaction found except at high temperature.⁹⁹ There are many other methods apart from CVD used to make TCOs which will be briefly discussed here.

If low temperatures are needed, for example if the material is thermally sensitive, plasma-assisted or plasma-enhanced CVD can occur at low temper-

atures where electrical energy is used to initiate reactions.¹⁰⁰ Sol-gel produces highly uniform film, with less risk of reactions happening in unwanted areas of the reactor, but requires a two-step process of first forming the amorphous layer which is crystallised normally using heat.^{101,102} Even though relatively cheap, this process can be very time expensive as each amorphous layer has to be dipped or spun onto the surface and is unsuitable for large scale high-throughput depositions.

In general extremely high levels of layer-by-layer control can be achieved with atomic layer deposition or an epitaxy-type deposition, however long deposition times are required with specialist equipment for maintaining low pressures and precise control of high-purity precursor flow.^{103,104} This is in contrast to AACVD where reactions can be carried out in atmospheric pressures and environments. For accurate controlled ratios of elements sputtering is often used, as the amounts of metal atoms in the gas phase released from the source can be controlled by the voltage of the high energy electron beam but this is an off-line method.

Inkjet printing methods of TCO materials provides the user with the option of direct patterning, extremely useful for solar cell fabrication, and precise control of the desired amounts of deposition. Due to the ink-drying process,¹⁰⁵ the thin films do not yet provide high conductivities seen from other deposition methods. Spray methods can be fast and the mechanism of reaction initiation can be adjusted according to the desired end product. The disadvantages are that the films produced from spray can be uneven and films tend to have impurity issues.¹⁰⁶

Instead of using a tightly controlled deposition process such as ALD and MBE, highly pure and dense thin films can be produced using CVD because of the way reactions occur through chemical reactions between the precursors in the gas phase. It is a non line-of-sight uniform coating process which is advan-

tageous over PVD processes that suffer from shadowing and uneven coatings on non-flat substrates.⁹³ In terms of experimentation, there are many independent variables allowing the user to tune the properties of the thin film such as morphology, orientation, and surface structure. In particular for aerosol-assisted CVD, as the volatility of the precursors is not as important, it opens up a wider selection range of precursors.

1.3.1 Aerosol-assisted chemical vapour deposition (AACVD)

There are a variety of ways to generate the gaseous precursors for CVD. Commonly atmospheric pressure chemical vapour deposition (APCVD) is used to carry out FTO deposition in industry.¹⁰⁷ In APCVD the precursor gas is generated directly using heat from the liquid precursor chemicals, without the use of a solvent, and mixed prior to being carried into the reactor deposition.¹⁰⁸ Even though APCVD allows for a high throughput process producing excellent optical and electronic properties, it is harder to control morphologies, which can be important for certain applications for example haze for solar cells. With AACVD, a solvent is used to dissolve the precursors, and this offers the user another factor to vary the resultant phase and morphology. This control in morphology achieved using AACVD, can be used as a seeding layer for APCVD, thereby combining the modification with the quicker synthesis of industrial-style APCVD.¹⁰⁹

For AACVD, fine aerosol droplets are formed from a precursor solution using either a Collision type atomizer, ultrasonically or through a standard spray head. In this thesis the droplets were mainly produced ultrasonically, but also through a spray head whereby the droplet size can be controlled by adjusting the liquid flow. The aerosol droplet size affects the proximity the precursor molecules are to each other and so the final film structure and mor-

phology through different energetically preferred reactions.¹¹⁰ When comparing the two droplet production types, ultrasonic droplets have an average size of 45 μm whereas the Collision atomizer produce much smaller droplets of around 0.3 μm . It has been shown that aerosols generated with a Collision type atomizer are more effective at depositing fluorine-doped tin dioxide with more desirable transparency and conductivity when compared to the ultrasonic generation or APCVD.⁶⁹ However, as the Collision atomizer is made from metal, it degrades when coming into contact with the auric acid precursor solution and so was not used for the purpose of this thesis.

A range of variables can be used in AACVD which allows the user to control the electrical and crystal properties such as deposition temperature, dopant concentration and aerosol size as variables.⁶⁹ We decided to use the AACVD system since there have already been reports of auric acid as a precursor for AuNPs in AACVD reactions,³⁸ and the system has also been shown to produce high quality SnO_2 TCOs.^{69,79} Reports on AuNP depositions using AACVD up until now have been sparse and this thesis aims to investigate these reactions further, improving the process and elucidate the reactions that are happening.

1.3.2 Thermophoresis

In an AACVD reactor there are a multitude of forces that affect the way in which the aerosol and particles flow through the reactor such as electrostatic, gravity, diffusion and thermophoretic forces.⁹ As the heat source lies along the bottom plate for an AACVD reactor (Figure 1.8) there is a decreasing temperature gradient from the bottom to the top plate. Thermophoresis describes the process when particles suspended between the plates can experience a force and flow upwards away from the heat source. The force is exerted on the particles from convection of gases within the reactor.

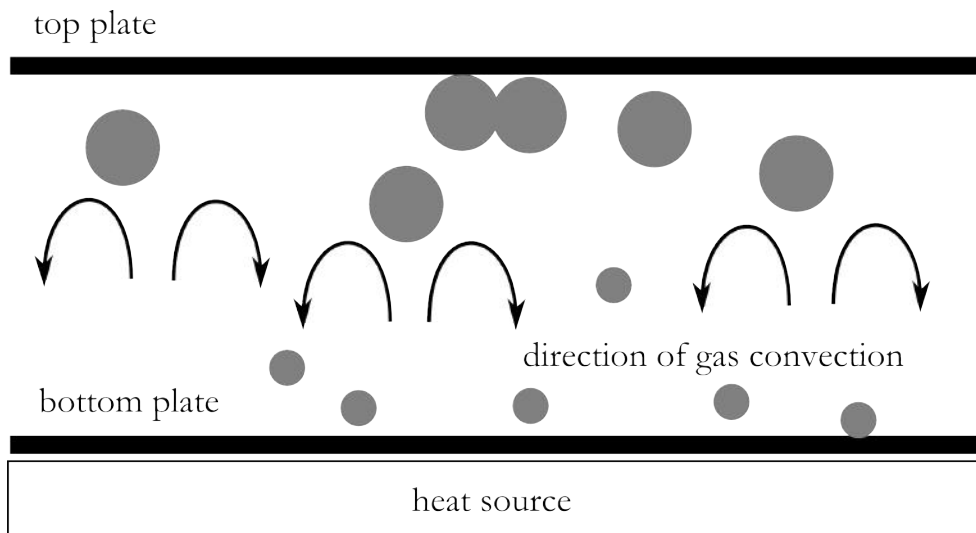


Figure 1.9: Arrows indicate the convection of gases upwards away from the heated substrate/bottom plate, affecting larger particles more strongly, transporting them towards the top plate and leaving smaller particles nearer the bottom plate.

The thermophoretic effect can be useful for directing unwanted contaminant particles away from the substrate¹¹¹ but can also make reactions unpredictable and be an unwanted effect for NP deposition. NPs are likely to experience thermophoresis due to their size compared to reactive molecules or particles, as has been shown for AuNPs in an AACVD reactions.^{38,112}

Temperature and flow rate affect the flow within the reactor and the observed thermophoretic effects. Flows of TiO_2 particles were measured for a horizontal reactor investigating the thermophoretic effects present. As a result of the flow and an upwards movement of the particles a perceived dust-free region was observed (Figure 1.10).⁹ This dust-free region was also found to increase with increasing substrate temperature and decreasing flow rates. Heavier and larger particles have smaller dust-free regions, however the particles investigated were all above $0.8 \mu\text{m}$, much larger than the NPs discussed in this thesis.

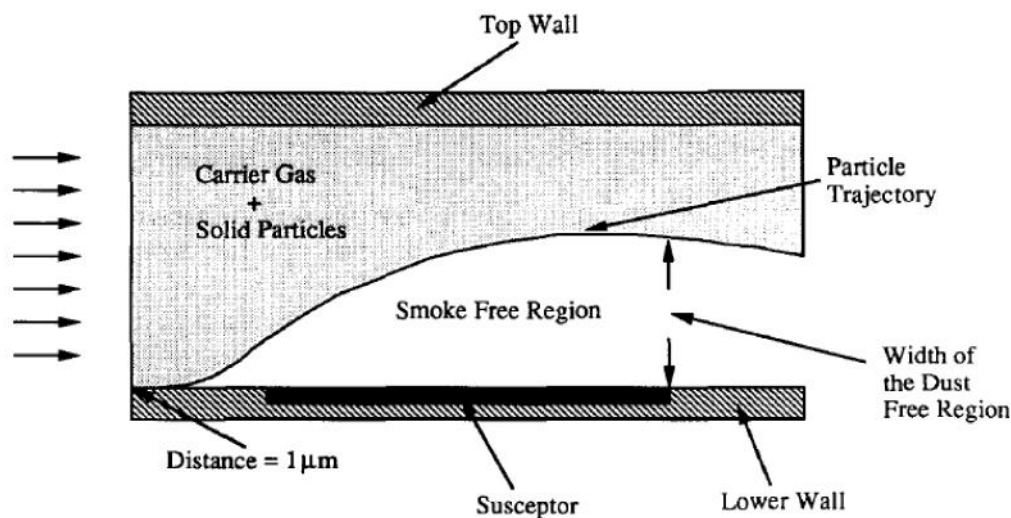


Figure 1.10: Schematic showing a horizontal reactor and flow of dust used in calculations of thermophoretic effects.⁹

1.4 CVD of SnO₂ thin films

Precursors are selected in terms of availability, solubility, decomposition temperature and molecular structure. Having the precursor in the desired oxidation state or already bonded to the desired atom, e.g. bonded with oxygen if product is an oxide, can be useful for achieving the desired product. The solvent is selected based on whether it can dissolve the desired precursor and how easily it forms a vapour in the ultrasonic humidifier. Solvents can be inert, act as a reagent or even a catalyst.^{69,79,113} This is also true for the carrier gas. The rate at which the gas carries the aerosol into the reaction chamber can determine where the reaction and deposition occurs. Deposition temperature is important for giving the desired phase and deposition pattern on the substrate; too high and the deposition occurs in the baffle not on the substrate, too low and product forms and exits through the exhaust. The various factors affecting the CVD of SnO₂ will be discussed briefly here.

1.4.1 Precursors

The deposition techniques used will determine the type of precursor chosen, which will then affect the final properties of the film by more than just the basic elemental composition. SnO_2 can be sputtered into thin film form from a readily oxidised SnO_2 or metallic Sn target. The metallic Sn reacts with O_2 gas in a process called reactive sputtering. However, instead of reacting at the surface with sputtered Sn atoms, the O_2 gas can also oxidise the target surface itself, switching to compound sputtering mode. The switch between metal and compound sputtering modes presents itself as a hysteresis in the material, resulting in a non-uniform and irreproducible thin films.¹¹⁴ As a result of this instability amongst others, various phases and oxidation states of Sn can be found in one deposition.¹¹⁵

For chemical vapour depositions involving tin chlorides such as SnCl_4 , an initial continuous rise in growth rate proportional to the precursor concentration was observed after which further increases had no effect.¹¹⁶ Agashe and Major suggests that instead of the Sn precursor undergoing gas phase pyrolysis, the Sn containing species first adsorbs onto the surface then reacts with H_2O to form the oxide. At certain precursor concentration levels the substrate becomes saturated with adsorbed species and there is not enough oxygen from H_2O to react with Sn which leads to a constant growth rate unaffected by the amount of Sn in the reactor. To further confirm surface reactions as key steps, experiments with tin tetrachloride (TTC) showed that the growth rates were actually too slow for the reaction to be initiated by gas-phase reactions.¹¹⁷ Using monobutyltin trichloride (MBTC) can give a more complicated view as when water and oxygen are involved, pyrolysis, hydrolysis and surface reactions all could be occurring simultaneously in the reactor.¹¹⁸

Van Mol et al. discussed kinetic models of reaction between MBTC, H_2O

and O₂ by combining computational techniques and comparing these to experimental data. For organometallic precursors such as MBTC the reaction can begin with the breakage of the Sn-C bond in the gas phase if temperatures reach above 400 °C, forming radicals which then start a chain reaction where deposition then occurs. However, commercial CVD reactors might not have high enough temperatures in areas that are not in direct contact with the heating element for the initial cleavage of the Sn-C bond, as areas away from the heated substrates are usually under 400 °C and so depositions under these conditions is only limited to surface reactions.¹¹⁸ They reported that the most likely model would begin with the gas-phase formation of an MBTC-H₂O complex, adsorption onto a substrate and consequent reaction with a gaseous O₂, which results in a mass transport limited growth rate observed dependent on the presence on MBTC concentrations. When using tetramethyltin (TMT) or dimethylindichloride (DMTC) as the precursor, it has been proposed that the rate limiting chemistry occurs in gas phase, leading to species such as SnO or SnO₂ which diffuse to the film where they are absorbed and further oxidised. However, modelling of the SnO₂ formations might be unrealistic as they were based on a laminar flow reactor within a tube furnace, meaning the whole reactor is heated evenly with little or no temperature gradient above the substrate.^{97,119,120}

By-products of precursor decomposition can have unintended effects on film growth. Radicals, formed from the breakdown of bromotrifluoromethane, act as scavenging agents inhibiting film growth.¹¹⁹ Further tests by using additional compounds of Br₂ and tert-butyl bromide in the reaction mixture was shown to inhibit film growth, therefore when choosing a precursor it is important to note if it thermally decomposes into any of radical scavenging species.⁹⁷ For reactions using common chlorinated Sn precursors, for example tin tetrachloride, by-products could include Cl₂ and HCl, and the ratio of these can

determine if the film has a rough or smooth surface.¹²¹ Any produced Cl_2 acts as an etchant, reducing the roughness and resulting in smoother films.¹²²

Sn precursors react with O containing species in the reactor to form SnO_2 and using a O containing Sn compound doesn't necessarily mean that fully oxidised SnO_2 is obtained. Tin acetylacetonate has been found not to form a film when deposited in N_2 , adding of H_2O formed SnO , and only when the carrier gas contained O_2 did SnO_2 deposit.¹²³ Alkoxides and β -diketonato precursors can deposit SnO_2 but with poor crystallinity and high resistivity.^{124,125}

Working within the AACVD system, tin precursors with a crown ether as a multidentate macrocyclic ligand has been used to try and modify the surface structure of SnO_2 in order to improve its gas sensing properties to some success.¹²⁶ In trying to deposit SnO_2 nanoparticles within a TiO_2 film from a nanoparticulate precursor solution, the system suffered from precursor loss, with the resulting film having decreased photocatalytic, electronic and optical properties.¹²⁷ SnCl_4 , although useful as an APCVD precursor, the high volatility is not needed for an AACVD system, and rather the high reactivity deters it as a precursor choice. Using compounds with an O present, such as an acetylacetonate adduct, results in SnO_2 with high C contamination giving less transparent films. Since MBTC reacts initially by the cleavage of the Sn-C bond,¹¹⁸ when used in an AACVD reactor MBTC deposits cleanly, with little C contamination. MBTC also volatilises easily in the bubbler using ultrasonic methods.¹⁰⁹ MBTC was used in this thesis as a Sn precursor because of its track-record of producing thin films with high transparency and low resistance,^{69,79} as well as the ease of handling and reasons just previously mentioned.

1.4.2 Temperature

High quality SnO₂ deposition has been reported mostly between temperatures of 400-600 °C. Early CVD studies of tetramethyltin (TMT) show that by increasing the deposition temperature, larger grains were produced since smaller crystallites had more energy to coalesce.¹²⁸ Larger grains will have less grain boundary scattering and the material should have a higher mobility.¹²⁹ Higher conductivity was observed in vapour deposited SnO₂ from SnCl₄ (TTC) when increasing temperatures from 380 up to 525 °C. This could be due to larger grain size, however, the conductivity could also stem from O deficiencies which also increases with deposition temperature. The increased conductivity was not observed if the temperature surpassed 600 °C, and instead mobility and carrier concentration began to decrease, perhaps due to O entering the lattice.⁶³ Another reason could be that in the reported films, Cl was also detected in the lattice, present in all films apart from the one at 600 °C. The Cl left behind from the TTC precursor could be contributing to the conductivity and explaining the increased resistance in films deposited at 600 °C. Other unintentional extrinsic doping has been found for example, Br has been detected in some films where SnBr₄ has been used as a precursor for spray deposition. As with the previously discussed depositions, increasing deposition temperature also increased O defects and lowered the final dopant concentration in the resulting film.⁶⁴ Another study also showed higher extrinsic F and Cl doping occurring only at lower temperatures.¹²⁸

For direct oxidation of TMT in a low pressure CVD system, at temperatures above 600 °C an observed a spontaneous gas phase reaction was observed which resulted in a white powder and only a very thin deposited layer of desired material.¹³⁰ Under 400 °C, TTC pyrosol depositions was suggested to be led by nucleation resulting in a smoother fine grained amorphous structure that re-

sembles “spherulites” or “cauliflowers”.¹²¹ This morphology was reportedly due to HCl and Cl₂ are produced as a by-product of TTC, and as the temperature increases, the amount of Cl₂ decreases leaving a larger proportion of HCl which etched the surface leaving it rougher.

Some precursors are able to deposit SnO₂ at a temperature lower than 400 °C, for example tin (II) bis-trifluoro acetate and tin acetylacetonate can deposit polycrystalline SnO₂ from 230 °C.^{123,131} The deposition reactions appear to be thermally activated, dependent on the surface reactions and the desorption and adsorption of gas phase species. Higher temperatures are still more advantageous as the deposition rate has been shown to increase from 0.092 nms⁻¹ at 360 °C to 0.65 nms⁻¹ at 510 °C.¹²¹ Along with a higher deposition rate, a higher temperature also means adsorbed surface molecules will be able to diffuse and find the most energetically favourable site, creating films with less imperfect crystallinity and a higher mobility. In an investigation using TTC there was an activation energy associated with the deposition rate and temperature again suggesting thermally activated growth led by surface reactions which depend on adsorption and desorption of gas phase species.¹²¹

Since temperature can affect the way precursor is broken down and the dopants, it can also affect the final Sn lattice positions. SnO and β-Sn peaks have been found in CVD depositions from chlorinated Sn precursors between 450-550 °C which can result in a narrowing of the band gap and reduction of optical transparency.^{79,128} Apart from the deposition temperature, the formation of Sn phases with lower oxidation states is also a factor of carrier gas and precursor compound.

1.4.3 Carrier gas

The carrier gas in the CVD production of SnO₂ can be inert or take part in the reaction, but either way its presence can still affect the reaction. Earlier studies have shown that Cl dopant levels found in SnO₂ was higher for films deposited in N₂, then O₂ and finally lowest for H₂.⁶³ Since O₂ can be involved in the reaction to form SnO₂, it is logical to assume that there might be a simple relationship found between oxygen pressure and deposition rate.¹³⁰ However, studies have shown that when the flow of O₂ was adjusted to a very low rate, a spontaneous gas reaction occurred, similar to reactions seen at high deposition temperatures (see Section 1.4.2).

When O₂ is in the reaction chamber and reacting to deposit SnO₂, it could eliminate oxygen vacancies thus decreasing the conductivity, as found by Kim et al., where their SnO₂ deposited with O₂ was more insulating than if N₂ was used.⁶⁴ Pre-mixing the precursors with O₂, rather than introduction in the reactor can result in a film with weaker crystallinity. The authors of a study on tin trifluoroacetate suggest that by introducing the O₂ to the tin compound earlier, the reaction occurs in the gas phase forming particles first before depositing on the substrate. Since the SnO₂ lattice had already been formed from gas phase reaction, it might be energetically unfavourable to rearrange on the substrate surface to form a more crystalline film overall.¹³¹

H₂O can also help the oxidation of Sn from tin (II) acetylacetonate (acac), but only incompletely to SnO, since the additional presence of O₂ was still needed for complete oxidation to SnO₂.¹²³ Even with laser ablation from an SnO₂ target, only when O₂ gas was present in the chamber did SnO₂ form.¹³² Perhaps because of the lack of crystallinity, using N₂ can also lead to more resistive and less transparent films, with a decrease in Hall mobility, rather than carrier concentration, which indicates scattering due to imperfect crystallisation

from a deficiency in reactive O species.¹³³ Post treatment after film synthesis such as annealing in N₂ or H₂ plasma can also improve conductivity, however with the danger of β -Sn formation.¹³⁴

Oxygen poor conditions has been shown to give rise to poor mobility probably due to scattering from the defects and disorders. This disorder due to thermal and structural defects manifests itself in Urbach tailing (Section 1.2.3), which was observed to a larger degree when N₂ was used as a carrier gas rather than air.⁷⁹

1.4.4 Flow rate

As the precursors flow into the reactor with the carrier gas, the mass transport of these reactants can be the limiting factor affecting the deposition reactions and rate. It was been shown that at very low flow rates the reaction rate is controlled by gas-phase mass transfer and the deposition rate is dependent on it, but with increasing flow the boundary layer thickness attains a limiting value and the reaction becomes controlled by the chemical surface reaction rate; growth is now independent of flow rates.⁹⁹

As the precursors enter the heated part of the reactor they can either pyrolyse, hydrolyse, react with another molecule in the gas phase, or adsorb onto the substrate before undergoing subsequent reactions. Instead of being mass transport limited, if any of these subsequent reactions have a low rate of reaction, any of them can also ultimately be the limiting factor in the rate of deposition. For example, the flow rate of TMT into the reactor was observed not to affect deposition rate, which probably means that formation of an active complex that is inherently related to O₂ is the rate limiting step. Consequently, deposition rate is proportioned to the square root of oxygen flow rate at low flow rates and constant at high flow rates.¹³⁰

1.4.5 Growth phase and structure

Certain depositions can result in SnO being detected in the final film, probably because SnO is an intermediate to SnO₂ and can be a consequence of incomplete oxidation. The oxidation of SnO to SnO₂ can occur directly, or through intermediates such as Sn₂O₃ and Sn₃O₄.¹³⁵⁻¹³⁷

The effects of using methanol and water with varying ratios as solvents in TTC pyrolysis reactions was found to increase the electrical resistance as CH₃OH:H₂O increased above a ratio of 2-3.¹³³ The hydrolytic formation of SnO₂ from the reaction of TTC and water was observed from SEM and XRD to form larger grains with higher crystallinity and preferred growth in the (200) plane resulting in higher Hall mobilities. An increase in the presence of CH₃OH at any reaction sites will lower the amount of H₂O present and so result in a lower rate of hydrolytic reactions, explaining why thin films deposited with higher CH₃OH:H₂O had a higher resistance. The balance has to be struck however, since the oxidation of Sn does not occur if the water content is too high.¹³³

Preferred orientation due to preferred nucleation on crystal surface, the deviation from randomly orientated powder crystals, increase with thickness of the film. The nucleation becomes more random or less deviated from random planes when the temperature increases to 600 °C or the partial pressure of the reactant is high.¹³⁸

The HF formed from pyrolytic reactions, as a result of using F dopant precursors, will linger in the reactor and etch the surface of the SnO₂ resulting in rougher thin films and should be taken into consideration as it may affect the perceived rate of deposition. When using identical deposition conditions in spray pyrolysis, FTO films exhibit a surface structure with higher granularity than when compared to SnO₂ films.⁸⁰

The use of the alcohols methanol, ethanol and isopropanol (IPA) as additives can adjust the surface morphology by increasing the micrograin density whilst decreasing micrograin size.¹³⁹ Authors have suggested that with the addition of alcohols, reactions with HCl in the reactor occur that decreases the amount of Cl on the surface and consequently increase the available nucleation points for H₂O, which controls the deposition rate in their reaction. The choice of solvent is an important factor since marked differences in the structure, preferred orientation and characteristics of films have been found in an extensive study of SnO₂ CVD depositions when using a wide variety of solvents.⁷⁹

1.4.6 Doping SnO₂

Intrinsic and extrinsic dopants can help increase the transparency and conductivity of SnO₂ as discussed in Section 1.2.2. Using average CVD synthesis temperatures can result in SnO₂ films with conducting properties are frequently observed, and since fully oxidised SnO₂ is insulating, it has been concluded that intrinsic doping is easily achievable in SnO₂. Extrinsic doping can occur on either the Sn or O site. The most common substitutional dopant is F, which forms F doped SnO₂ or FTO, and on the Sn site various cations with a higher valency than +4 have also been tested widely.

Alkoxyfluoro tin complexes, Sn(OR¹)F(R²COCHCOR²)₂ **1** (R¹ = *tert*-amyl, isopropyl, ethyl; R² = methyl, *tert*-butyl) with a covalent bond between the Sn and F were synthesised as precursors for sol-gel and seemed promising as thermal treatment at 550 °C yielded crystalline solids with low resistivity.¹⁰¹ However, after complexes **1** were prepared through the sol-gel route and deposited either by spin-coating or spray pyrolysis, even though the thin films had good F incorporation of 3 mol.% the optical transmittance was low due

to high C contamination. Further to this, during the formation of the thin film by spin-coating, large amount of organic compounds were released during the thermal treatment leaving the structure with high microporosity and a low electronic conductivity across the thin film.¹⁴⁰ Films spray coated from the same compound might also seem promising with resulting films containing even higher F doping of up to 10 at.%, however it was found that the F did not contribute to the carrier concentration, as instead of sitting in O sites the F dopants were occupying interstitial sites or the edges of the grain boundaries, and so the F dopants contribute to carrier scattering and reduced the overall mobility of the material. F ratios of up to 250 at.% Sn in the precursor solution has been shown to improve conductivity before saturation when using a higher concentration.⁷⁷

The ease of which something can be doped into a lattice is affected by the size. Not only can a dopant affect the host lattice by being incorporated in the structure it can also affect the growth mechanism as shown by the increasing grain size of SnO₂ due to strain from Sb doping.¹²⁹ There seemed to be an optimum F/Sn ratio whereby the thin film can become the most polycrystalline in nature which should give the good mobilities suitable for TCO purposes. It was observed that increasing the atomic ratio of the precursor solution F/Sn to 0.1 can increase the crystallinity of the film resulting in higher intensity reflections in the XRD pattern. However, at even higher atomic ratios the intensity of the XRD reflections was seen to begin to decrease again due to lattice disorder from high dopant concentration.¹⁴¹

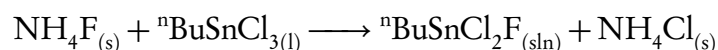
The doping levels of F actually entering the SnO₂ lattice has been found to be small compared to the amount in the starting precursor solution, though some studies have still shown that higher F in solution results in more effective F incorporation.¹⁴² F has been observed to evolve and form a very stable HF by-product that would not take part in the CVD reaction, which might be the

case in most precursor solutions since H will be in abundance due to the breakdown of any precursor compounds and also trace H_2O .⁸⁰ Since the uptake of F into SnO_2 is relatively poor, the environment of the F atoms in the precursor solution is probably an important factor as to whether it can actually dope the host lattice effectively and also the final position of the dopant atom.

Naturally, using a precursor compound with a pre-existing Sn-F bond has been suggested for improving the solubility of F in SnO_2 , however most Sn-F compounds have poor volatility making them unsuitable for many deposition methods where the precursor solution needs to be nebulised into droplets.¹⁴³ There are still a few examples of Sn-F precursors in the literature. For example, the CVD of trichlorotrifluoroethane ($\text{C}_2\text{F}_3\text{Cl}_3$) can result in FTO films, however unknown phases of SnF_2 or Sn_xO_y were detected in the XRD due to incomplete decomposition of SnO_2 .⁶⁸ A complex of amyloxyfluorodipentan-2,4-dionatotin(IV) was used in sol-gel, spin and spray coated resulting in thin films with F content of 3 at.% and 10 at.% respectively. The spin coated film suffered from large resistivity due to a disconnected microstructure and the spray coated was also quite resistant either due to excess F or C, since appreciable levels of C at 10 at.% were detected.¹⁴⁰ Another option would be to use a complex containing both Sn and F elements, but not connected with a direct bond, for example an organotin fluoroalkoxide. Variation was found as to how much F can be incorporated into the SnO_2 lattice, however this depended not on the quantity of F, rather the environment, even so the best F incorporation was found to be only 1.52 at.%.¹⁴³

For AACVD, the deposition technique used in this thesis, F-doping has been performed with trifluoroacetic acid,^{69,109} Even though a fluorinated tin compound has been shown to be able to deposit FTO with APCVD, the optoelectronic properties and F incorporation was still worse than dual source precursors.¹⁴³ Increasing the amount of F in the compound does not improve

the incorporation and it was found that the position of the F in the molecule is more important. In other AACVD reactions, an exchanged reaction between NH_4F and MBTC (shown below) in the precursor solution has been observed explaining the high quality doping that can be seen in FTO thin films produced using AACVD and this precursor mixture.⁷⁹



Ammonium fluoride would thus pair well as a dopant for MBTC used in the AACVD system used for this thesis.

1.5 Gold nanoparticles

TCOs can be combined with other optically interesting material to add new functionality and create new hybrid materials. Gold nanoparticles (AuNPs) have an unusual and interesting absorbance called the surface plasmon resonance (SPR) absorption which gives them visually attractive purple and pink colours. Composites of AuNPs and TCOs based on SnO_2 are presented in Chapter 3 and are shown to have a novel combination of properties: highly conductive, transparent and robust with a strong SPR absorbance from AuNPs.

Evidence for the use of nanoparticles colouring glass can be traced back to the 4th or 5th century AD, a famous example being the Lycurgus cup. Production of ruby red glass began in the 17th century with the use of Purple of Cassius - the product of a reaction between gold salts with tin (II) chloride.¹⁴⁴ It was thought that a Au:Sn alloy was the source of the colour, but we now know that the true origin of colour was the Au nanoparticles supported on tin dioxide.¹⁴⁵ Nowadays coloured glass for architectural windows is highly sought after and is traditionally introduced by body tinting via doping with

various metal oxides such as cobalt oxide for blue glass.¹⁴⁶ However since the metal oxide dopant is introduced into the liquid part of the flow process of glass production, when changeover is needed large amounts of waste are generated when flushing the system. We propose that a gold nanoparticle coating could be used as a potential colourant for modern glass production.

1.5.1 Optical properties and surface plasmon resonance

Particles in the nanosize region are interesting as they exhibit properties not seen in bulk material or their molecular counterparts. For metallic particles larger than 2 nm a surface plasmon band absorption is observed in the UV-vis spectra. These are effects due to surface plasmon resonances (SPR) or the Mie resonance, the scattering of electromagnetic waves due to a homogenous dielectric particle.¹⁴⁷ Gold, along with silver and copper exhibit very intense surface plasmon bands, or SPR absorbances, hence can be easily seen with the naked eye. This is one of the reasons as to why these elements have become successful in applications involving nanoparticles. The fascinating array of colours associated with the gold have been well known historically and investigations by Faraday was presented at a Royal Society Lecture in 1857.¹⁴⁸ Faraday realised that the red colour seen in some instances of gold could be due to the small sizes of the metal particles.

The colour of gold nanoparticles (AuNPs) originate from strongly localised surface plasmon resonance (SPR), which changes according to the size and shape of the particles and the surrounding dielectric media.¹⁴⁹ Light induces a dipole in the nanoparticle causing the surface electrons to oscillate against the restoring force of the positive static nuclei. An absorption called localised surface plasmon resonance (LSPR) occurs at the wavelengths where the incoming photon frequency are coherent with the collective oscillations of the

surface electrons (Figure 1.11).¹⁴⁷ Mie's theory describes and predicts the dependence of the SPR with regards to the size of the nanoparticles by solving Maxwell's equations for spherical particles.¹⁵⁰ However since the delocalised conduction electrons oscillate in the interface of two materials with different dielectric functions, such as between metal and air, changing the character of the media surrounding the NPs, specifically the dielectric constant, will alter the interface properties experienced at the NP surface and consequently change the resonant frequency of the conduction electrons. The LSPR absorption frequency will thus change giving a different coloured nanoparticle. Changing the interface property by altering the dielectric constant of the surrounding media allows the character of the nanoparticles to be fine-tuned and adjusted for many different applications other than a colourant, such as in sensors, catalysis and imaging.¹⁵¹

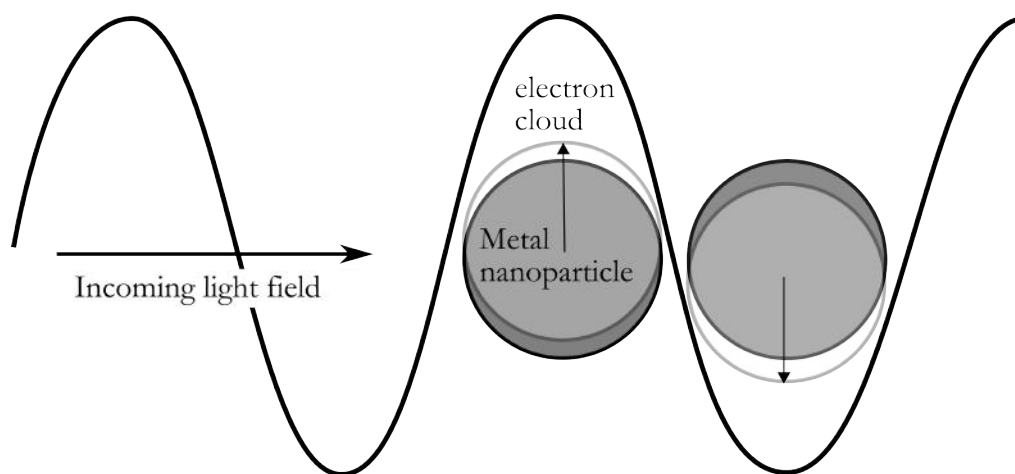


Figure 1.11: Oscillation of conduction electrons due to absorption at resonant frequencies at the curved surface of metal nanoparticles called localised surface plasmon resonance.

Many papers have been published studying the relationship between the surface plasmon band and the properties of the nanoparticles. It has been found that the surface plasmon band is affected by the size and shape of the nanoparticles.^{10,152} This is illustrated simply in Figure 1.12 whereby the authors adjust

the size of the nanoparticles by the amount of auric acid used in their citrate reduction method.¹⁰ Another factor that affects the SPR of nanoparticles are the dielectric constants of the medium in which they sit in.¹⁵³ This is exploited and used to enhance the Raman signal of organic molecules – surface enhanced Raman spectroscopy (SERS). In 1979 the Raman scattering signals of pyridine was found to increase when adsorbed onto silver or gold nanoparticles.¹⁵⁴ The localised resonances create an effective electric field at the molecules and the metal-adsorbed-molecule system enhances the Raman scattering of the adsorbed molecule.¹⁵¹ Tuning the SPR to midway between the exciting laser and the Raman band optimizes the SERS effect.¹⁵⁵

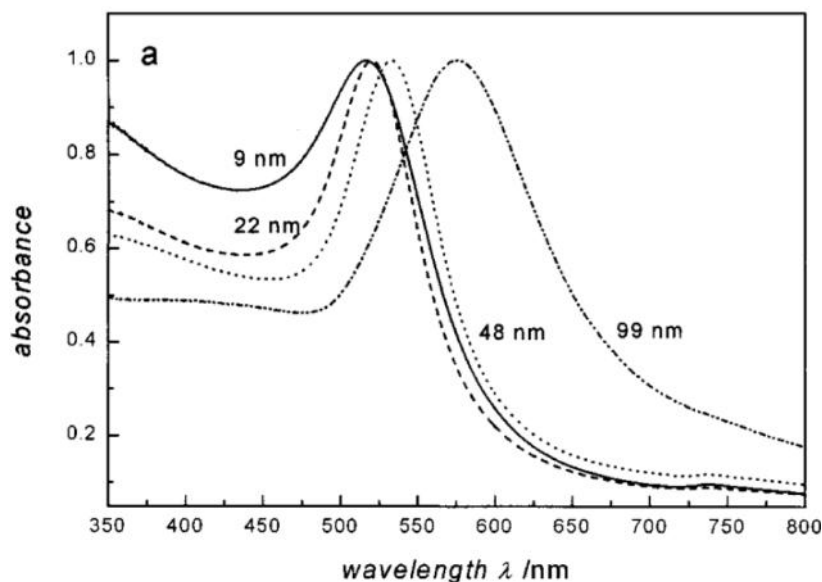


Figure 1.12: Absorbance spectra of 9, 22, 48 and 99 nm sized gold nanoparticles normalised at their maxima, synthesised from auric acid with varying citrate concentrations.¹⁰ Reprinted with permission from *Size and Temperature Dependence of the Plasmon Absorption of Colloidal Gold Nanoparticles*, S. Link and M. a. Sayed, *The Journal of Physical Chemistry B*, 1999, 103, 4212-4217. Copyright (1999) American Chemical Society.

1.5.2 Synthesis

The ability to tailor the properties of nanoparticles is desirable since it fundamentally affects the role NPs play in many applications such as the optical properties or its performance as a catalyst.¹⁵⁶ A common and established way to make AuNPs on the benchtop is through the Turkevich method which involves the reduction of auric acid by trisodium citrate in water.¹⁵⁷ Heat is applied to the stirring solution and at 100 °C the reaction takes about 10 minutes to complete. The resulting nanoparticles can be monodisperse and range between 10-30 nm. The trisodium citrate also acts as the capping agent and the concentration of it can affect on the final size of the AuNPs, however this can also depend on the initiation method of the reaction.¹⁵⁸ Growth of AuNPs in citrate proceeds through an Ostwald ripening mechanism first where the smaller NPs dissolve into larger NPs before equilibrating to a maximum size. For nanoparticles in organic liquids, the Brust-Schiffrin method can be employed. Here tetraoctylammoniumbromide (TOAB) is used as a transfer agent, before reduction in the organic solvent proceeds through a reduction with sodium borohydride with dodecanethiol as the capping agent.¹⁵⁹

Through preliminary experiments using the AACVD set-up as described in this thesis, it was found that depositions using gold nanoparticles in the bubbler was poor because they were very thermophoresis and the gas flowing through the reactor. In Section 3.5, AuNPs are instead directly reduced and deposited simultaneously onto glass substrate in an AACVD reactor. It is typical for AuNPs to not adhere well to surfaces such as glass,^{112,160} and although silanisation reactions between the AuNPs and glass surfaces can overcome this.^{37,161,162}

1.5.3 Applications

In medicine, gold nanoparticles have been shown to be promising drug delivery vehicles, with the ability to densely pack and stabilise the delivery drug.¹⁶³ Drugs were loaded onto gold nanostars with an average size of 25 nm and a SPR centred at 780 nm, allowing them to enter the cell and deliver the treatment directly at the cell nucleus.¹⁶⁴ The tips and bodies of the nanostars shown in Figure 1.13 have different resonances, increasing the range of energy they can transfer to the molecule.¹¹

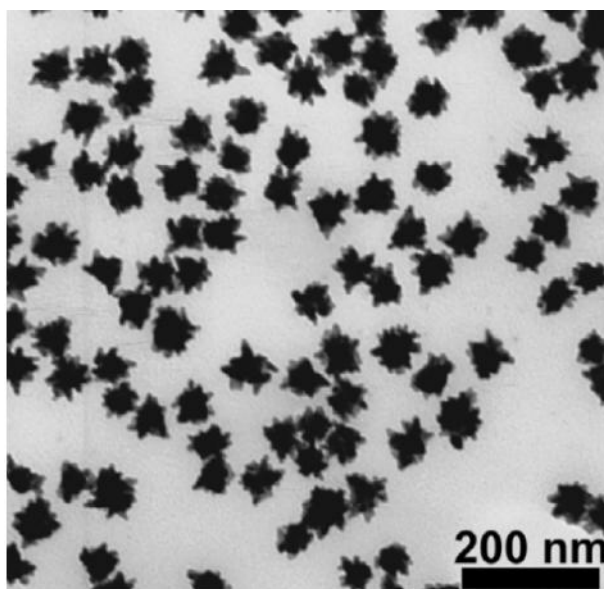


Figure 1.13: TEM image of Au nanostars synthesised from HAuCl_4 .¹¹

AuNPs are used in many and everyday health applications. Most famously, they are found in First Response pregnancy tests whereby the AuNPs become mobile when the correct peptide is present and clump together manifesting itself as a coloured sign.¹² Novel treatments use AuNPs to photothermally kill cancerous cells and bacteria.^{165,166} It has also been found to be antibacterial when paired with toluidine and light activated methylene blue as well as used for the detection of anti-microbial susceptibility.^{167,168}

Another popular and widely used application of AuNPs is in the field of

catalysis, some of which will be tested in Chapter 5. Reactions that AuNPs are effective catalysts for are extensive: low temperature oxidation of CO,¹⁶⁹ partial oxidation of hydrocarbons,¹⁷⁰ the water-gas shift reaction, where hydrogen is generated from CO and water¹⁷¹ and reduction of nitrogen oxides,¹⁷² which is useful for cleaning emissions from engines or factories, the polymerisation of pyrrole,¹⁷³ and aniline,¹⁷⁴ and oxidation of alcohols.^{175,176}

1.6 Composite nanoparticle metal oxide

1.6.1 Applications

By depositing noble metal nanoparticles alongside metal oxides desirable functional optoelectronic properties can be improved. The enhancement of the local electric field by nanoparticles such as gold onto dielectric materials can also be useful for optical and photonic devices because of their resulting large third order optical non-linearity.¹⁷⁷ Au composites have also been shown to improve the switching properties in a WO_{3-x} electrochromic system.¹⁷⁸

It has been recently reported that gold nanoparticle metal oxide composites have been suggested to exhibit photocatalytic activity in the visible range. TiO_2 is another widely synthesised metal oxide because of its use in many applications such as the photocatalytic degradation of organic molecules for self-cleaning materials and for cleaning up surface waters.¹⁷⁹ Titania is also an important component in the conversion of solar to chemical energy by water splitting. AuNPs have been said to work both as light harvesters in the visible, promoting electrons into the conduction band as well as catalytic sites for gas generation.¹⁸⁰ Other work has shown an increase in photocatalytic activity in the visible but a slight decrease in the UV. They suggest that the improvement of the activity is caused by local electric field enhancement near the TiO_2

surface, increasing the photogeneration of charge thereby increasing catalytic activity.¹⁸¹ Au-TiO₂ can also have anti-reflective properties, bringing an added efficiency boost to solar cells.⁸⁶

Another important gold:metal oxide application worth mentioning is metal oxide supported gold catalysts, whereby the catalytic activity of the gold is related to its state as a composite with the metal oxide.¹⁸² The extent of this catalytic activity can be related to the other functional properties of AuNP and metal oxide composite.

1.6.2 Synthesis

Gold nanoparticle:metal oxide matrices have mostly been deposited in bulk form or as thin films, they have also been synthesised as nanowires and nanocomposite particles.¹² In general there are five different routes to noble nanoparticle metal oxide composite thin films as shown in Figure 1.14. In Route 1 a thin film of metal oxide is first deposited, after which nanoparticles are added on top. Ready-made FTO electrodes were silanised, then soaked in a solution of AuNPs synthesised using citrate reduction, before being tested in a dye-sensitised solar cell.¹⁸³ Of the various sizes tested, the 25 nm AuNPs were found to increase the overall performance by 15 % compared to the basic FTO electrode.

Route 2 describes the method whereby metal ions or compounds are first deposited onto the metal oxide thin film, then through a secondary process are converted into nanoparticles. For example, an organogold precursor was first adsorbed onto Al₂O₃, SiO₂, and TiO₂, after which a heat driven decomposition reaction resulted in gold nanoparticle composite catalytic materials for the oxidation of Co and H₂.¹⁸⁴ AuNPs can also be formed through agglomeration of a thin Au film by being heated for 2 hours at 400 °C, as shown when

Scheme 1 Methods of making thin films with embedded nanoparticles

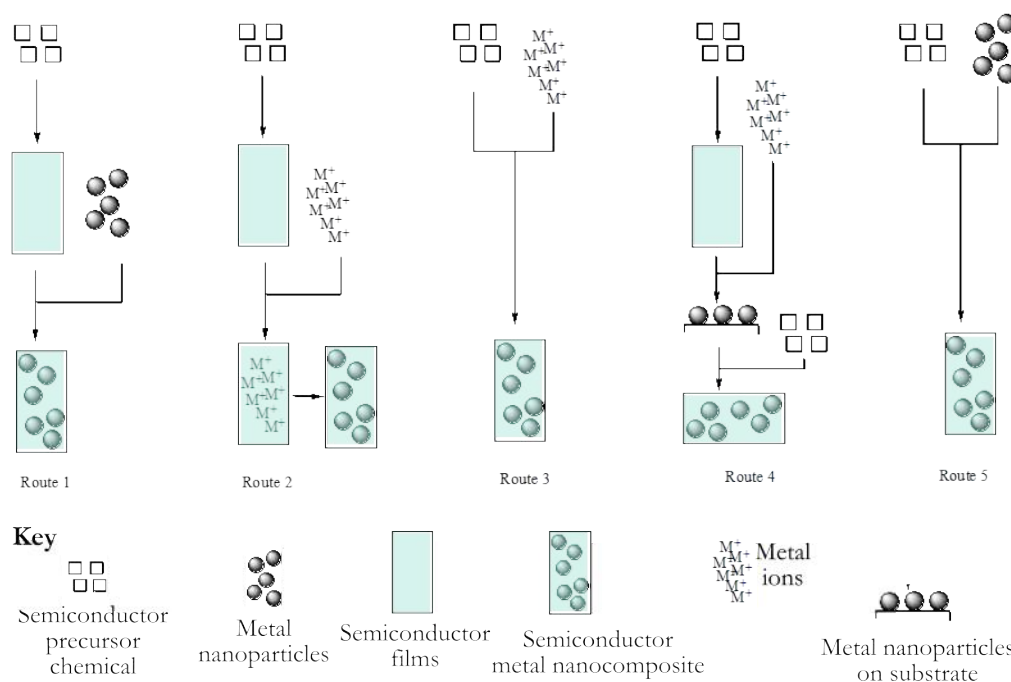


Figure 1.14: A basic outline of the various routes used to make thin films with embedded nanoparticles (adapted from Walters *et al.*).¹²

for depositions using reactive magnetron sputtering onto a ZnO film,¹⁸⁵ where another layer of ZnO was deposited on top of the AuNPs to create a sandwich structure. A similar sputtering technique was used for metal oxide/Ag/metal oxide thin films, with the omission of the thermal agglomeration resulting in a Ag thin film, with very low resistance of $4.4 \Omega/\square$ and high transparency.^{186,187}

The metal oxide and nanoparticle precursor can be delivered and deposited at the same time as described by Route 3. AACVD experiments have been used to deposit various AuNPs and metal oxide nanocomposites of WO_3 , MoO_3 and TiO_2 using auric acid on glass in a single-step process from one precursor solution.³⁸ Again using AACVD, thin films of Pt (1-4 nm) and Au (4-11 nm) nanoparticles composites with WO_3 nanoneedles were deposited onto gas sensors but this time from two separate precursor solutions.¹⁸⁸ With another one-pot solution of chloroauric acid and zinc acetate, thin films of gold nanoparticle (7-13 nm) and ZnO composites were deposited onto glass and ITO substrates

via spray pyrolysis.¹⁸⁹ An increase in the photoelectrical current performance was found and a change in the morphology of the ZnO with the presence of chloroauric acid, which might affect the optical properties of the solar cell. The aerosol in the CVD system can be generated using two mechanisms as shown by the hybrid AA/APCVD system used to deposit AuNP vanadium dioxide thin films.¹⁹⁰ Using a liquid phase deposition method, AuNPs dispersed in SiO₂ was deposited onto TiO₂.¹⁹¹

In Route 4, the metallic nanoparticles are deposited and formed on the substrate first, with a second step for metal oxide deposition. The electrochromic performance of WO₃ was shown to improve if the structure was decorated with gold nanoparticles due to an increase in charge transfer ability. The composites were formed in a two-step process with the AuNPs being deposited first. The AuNPs with sizes of 40-60 nm were first electrodeposited onto ITO using potassium dicyanoaurate, and an WO₃ layer subsequently deposited above it using sol-gel.¹⁷⁸ Care has to be taken when using this route, as the nanoparticles could undergo further change during the second metal oxide deposition step, as high temperatures are frequently needed to obtain a high quality crystalline film.

If the size and character of the nanoparticles are of great importance to the final product, Route 5 can be undertaken as the nanoparticles are synthesised prior to forming the composite. Recently a thin film of Au nanoparticles embedded in SnO₂ was spin coated from a sol-gel solution of SnO₂ coated Au nanoparticles to ensure a homogenous film.¹⁹² Sol-gel solutions containing the Ti precursors as well as AuNPs synthesised from the Turkevich method, were dip coated with the thickness of the films varied from the number of coatings and withdrawal speed.¹⁹³ Even though the size of the nanoparticles can be controlled at the outset, there is still a final annealing stage at 550 °C for one hour which could alter the shape of the nanoparticles. AACVD with a one-pot solu-

tion of gold nanoparticles and metal oxide precursor has been used to deposit TiO₂ and WO₃ composite films.³⁸ Self-assembled arrays of gold nanoparticles and silica produced highly ordered thin films, using micelles of gold nanoparticles in a emulsion solution with soluble silica.¹⁹⁴

1.7 Aims

There have been a few studies focusing on the application of Au:SnO₂ composites in gas sensors, where powders and nanoparticles have been synthesised,^{195,196} however, there isn't much in the literature about AuNP/SnO₂ composites with high transparency or low resistance properties. The CVD procedure is closely related to the industrial way of coating glass and at the outset this thesis explores the possibility of synthesising composite AuNP/SnO₂ films with a high electrical conductivity and visible transparency, and a linear combination of both films without detrimental effect to the TCO or thin film quality. Having deposited noble nanoparticles using this method, composites can be expanded to other metal oxides, with the possibility of tuning the SPR with changing character of the metal oxide thin film rather than the shape of the nanoparticles. Finally, AACVD is used to deposit gold nanoparticles on another silica substrate other than float glass, on glass wool. With the high surface area of glass wool, the potential catalytic activity of the AuNPs is explored.

Chapter 2

Experimental and Analytical

Details

This chapter will give details into the deposition techniques used to make the thin films of metal oxides and gold nanoparticles as well as the various characterisation techniques used for analysis.

2.1 Aerosol-assisted chemical vapour deposition set-up

The AACVD set up used in in this thesis is shown in Figure 2.1. This is a cold-walled (only substrate is heated) tubular reactor, with a thermocouple-controlled graphite block, containing a Whatmann cartridge heater which was used to heat the glass substrate. The temperature of the substrate was monitored and maintained using a Pt–Rh thermocouple. The ultrasonic aerosol was generated with a PIFCOHEALTH ultrasonic humidifier, with an operating frequency of 40 kHz and 25W of power. The aerosol was moved to the reactor using a nitrogen gas flow via PTFE and glass tubing, where it entered through a baffle between the top and bottom plates. The single-entry baffle ad-

justs the gas flow so that it enters the reactor in a horizontal plane and prevents the heating and premature reaction in equipment directing the aerosol flow. The structure of the top and bottom plates with 8 mm separation between them encourages laminar flow and an even deposition on the substrate. The main substrates used in this thesis were Pilkington NSG barrier glass with a 50 nm SiO₂ coat which prevents ionic impurities diffusing into the deposited film. These were cut to fit the reactor (145 mm × 45 mm) cleaned with soapy water, isopropanol and acetone then air dried prior to use. Any gaseous by-products left via an exhaust.

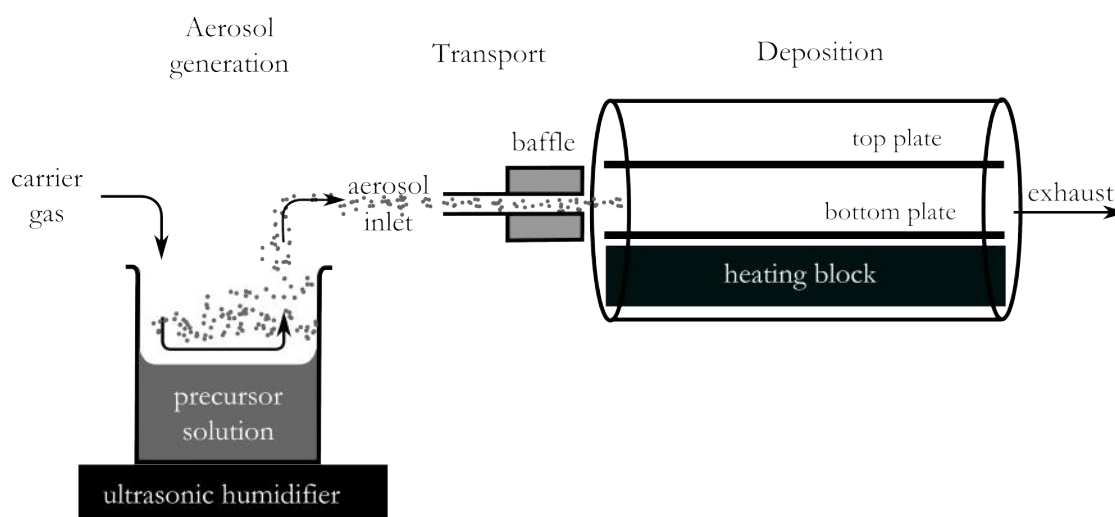


Figure 2.1: Experimental set-up for aerosol assisted chemical vapour deposition.

2.1.1 Materials

Hydrogen tetrachloroaurate hydrate (49% Au) and hydrogen tetrachloroaurate(III) solution (40-44% Au) were supplied by Alfa Aesar of Johnson Matthey Plc. Monobutyltin trichloride (95%), ammonium fluoride (>99.99% trace metal basis), titanium ethoxide (technical grade), gallium acetylacetonate (99.99% trace metal basis), aluminium acetylacetonate (99%) were all purchased from Sigma Aldrich Chemical Co.. Magnesium acetate and zinc acetate were obtained

2. Experimental and Analytical Details

from Hopkin & Williams were. Methanol was bought from Fisher Chemical and was used as received.

Table 2.1 gives an overview of the materials deposited using AACVD in this thesis, the precursors and deposition details. The metal oxides that formed a layered composite in Chapter 4, were chosen to deposit at the same temperature as the AuNPs of 450 °C to avoid further reactions of AuNPs. The flow rate and carrier gas were chosen to give the most efficient and even coverage in the deposition. Ti precursors suffer from spontaneous powder formation in the gas phase and so the equipment (bubbler, any connecting pipework and baffle) were all dried in an oven for at least 1 hour prior to use.

Table 2.1: The materials investigated in this thesis and their deposition details.

Desired material	Precursor	Solvent	Carrier gas	Temperature (°C)
SnO ₂	monobutyltin trichloride (CH ₃ (CH ₂) ₃ SnCl ₃)	methanol	compressed air or nitrogen	400-500
AuNPs or particles	hydrogen tetrachloroaurate (HAuCl ₄ xH ₂ O)	methanol	compressed air or nitrogen	400-500
TiO ₂	titanium ethoxide (Ti(OC ₂ H ₅) ₄)	toluene	nitrogen	450
Al ₂ O ₃	aluminium acetylacetonate ([CH ₃ COCH=C(O-))CH ₃] ₃ Al)	methanol	air	450
Ga ₂ O ₃	gallium acetylacetonate ([CH ₃ COCH=C(O-))CH ₃] ₃ Ga)	methanol	air	450
ZnO	zinc acetate ((CH ₃ CO ₂) ₂ Zn)	methanol	nitrogen	450
MgO	magnesium acetate ((CH ₃ CO ₂) ₂ Mg)	methanol	air	450

2.2 Spray deposition

The precursor solution is injected into a chamber where a high pressure stream of gas pushed the solution through a pneumatic atomizing nozzle creating a downward flow of aerosol towards the substrate which was heated to 350 °C (Figure 2.2). The nozzle is the Lechler series 136.330.xx.16 nozzle with a diameter of 0.40 mm and a 20° spray angle with a full cone using a siphon principle and external mixing.

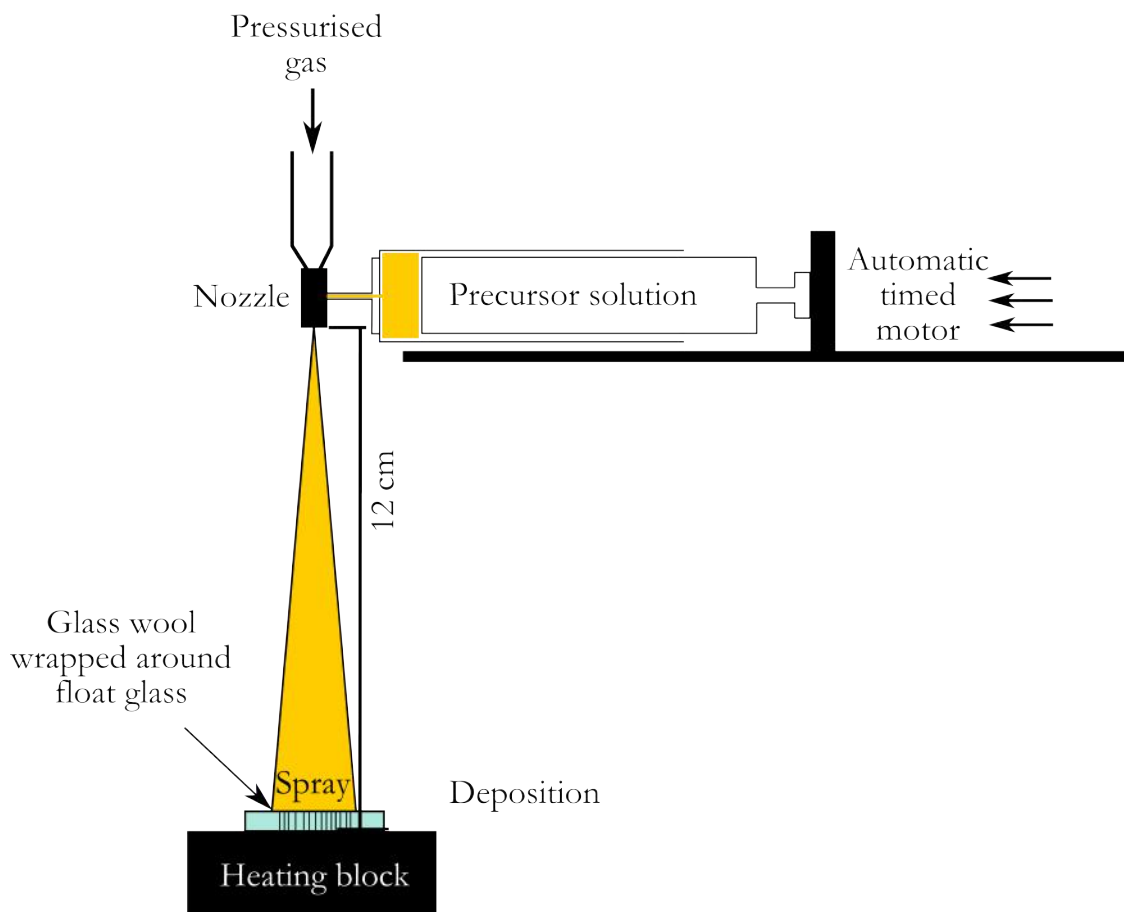


Figure 2.2: Set up for spray deposition.

2.3 Analytical techniques

2.3.1 X-ray diffraction

XRD was used to detect phase and preferred orientation growth. Thin film measurements were performed at a glancing angle of $1-5^\circ$ on a Bruker D8 (GADDS) and Discover LynxEye diffractometer using monochromated Cu $K\alpha$ radiation ($\lambda = 1.5406$) in reflection mode over $10-66^\circ/2\theta$. Depositions on glass wool were measured using a STOE diffractometer with monochromated Mo $K\alpha 1$ radiation ($\lambda = 0.7093$) in transmission mode over the angle range $2-40^\circ/2\theta$.

Diffraction peaks in an XRD pattern arise from the coherent interference of x-rays when they specularly reflect from a periodic lattice of atoms, as those found in a crystal structure. The different planes of a unit cell generate different lattice spacings and so giving rise to interference at different angles. The interferences relate to the incoming wavelength with Bragg's equation:

$$n\lambda = 2d \sin\theta$$

In order for the reflected light to be coherent, the wavelength of the x-rays have to be multiples of $2d \sin\theta$ as shown in Figure 2.3.

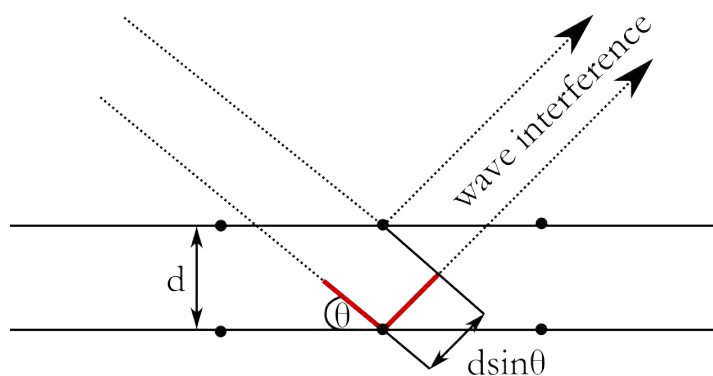


Figure 2.3: Schematic showing how satisfying Bragg's Law of $n\lambda = 2d \sin\theta$ can generate coherent interference between the x-rays. The full length of the red line represents $2d \sin\theta$ and λ represents the wavelength of the x-ray (adapted from Diffraction Physics, by J. M. Cowley¹³).

From comparisons of the XRD intensities of reflections in each plane between a randomly orientated powder and any deposited thin film, the preferred growth of each plane can be calculated and described using the texture coefficient.

2.3.2 UV-visible-IR spectroscopy

Optical properties such as transmittance, reflectance, absorbance, band gap and SPR absorption were measured using UV-Vis spectroscopy on a Perkin Elmer LAMBDA 950 UV-Vis/IR Spectrophotometer. The Swanepoel method was used to calculate film thickness from interference pattern¹⁹⁷ and was correlated with the F20 Filmetrics measurements made in air and calibrated with a silica standard. The band gap was measured from Tauc plot calculations.¹⁹⁸

2.3.3 Filmetrics and Hall effect

The Filmetrics F20 system was used to measure film thickness based on the interference pattern from reflections over 350-1000 nm. Electronic properties of the thin films were measured using the Hall effect on an Ecopia HMS 3000 set up on samples cut into 0.5-1 cm square pieces, with silver painted electrodes on each corner, and using a 0.58 T permanent magnet at currents of 0.01-1 mA. When a conducting sample is placed perpendicular to a magnetic field, a voltage difference arises perpendicular to both the current and the magnetic field (Figure 2.4). The Hall voltage with film thickness input is then used to calculate resistivity, carrier concentration and mobility.

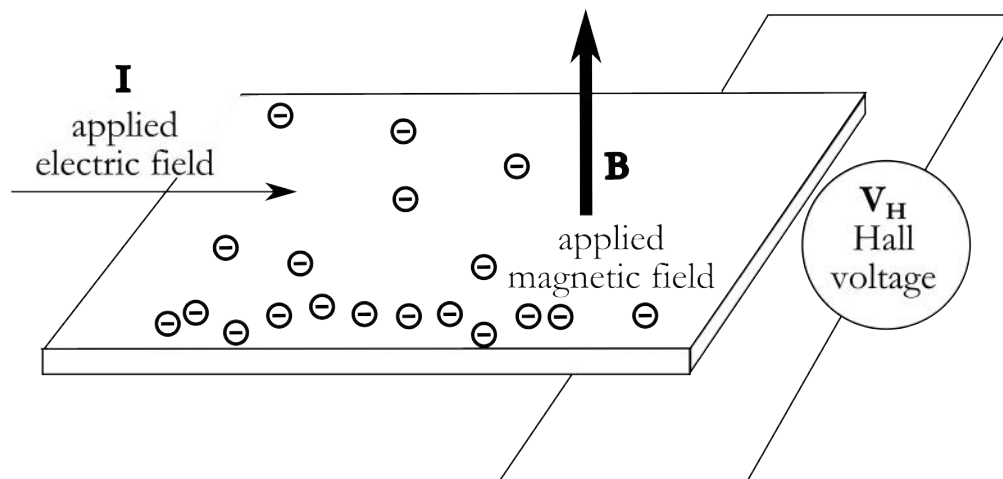


Figure 2.4: Diagram of the Hall effect where charge accumulation on a conductive thin film due to Lorentz forces from transverse applied electric and magnetic fields (adapted from Hall-Effect Sensors, Ramsden, E.¹⁴).

2.3.4 Scanning electron microscopy

SEM was performed to investigate surface morphology and elemental analysis on a JEOL JSM- 6301F and 6700F field emission microscope operating at 3-10 kV for imaging and 10-20 kV for EDX. Samples were cut and stuck onto the stage with carbon tape, sputtered with C or Au and grounded with Cu tape or Ag paint to prevent charging. In an SEM (Figure 2.5), electrons are accelerated towards the sample using a bias and secondary electrons are detected to create an image based on the electron density. Secondary electrons are ejected due to inelastic scattering between the samples valence electrons and the incoming electron beam. The beam is scanned across the surface and so the intensity of secondary electrons and resulting image represents topographical character of the sample surface at the micrometre level making it a valuable tool for interpreting the optical and morphological properties of thin films. Backscattered electrons are detected from electrons that elastically scatter from the nucleus and is useful for distinguishing between some elements, since elements with a high atomic number ejects more backscattered electrons resulting in a brighter parts of the image. Detection of elastically scattered electrons was

used to quickly scan across a large area to locate noble metal nanoparticles that are embedded within a semiconductor, where EDX provided further elemental confirmation.

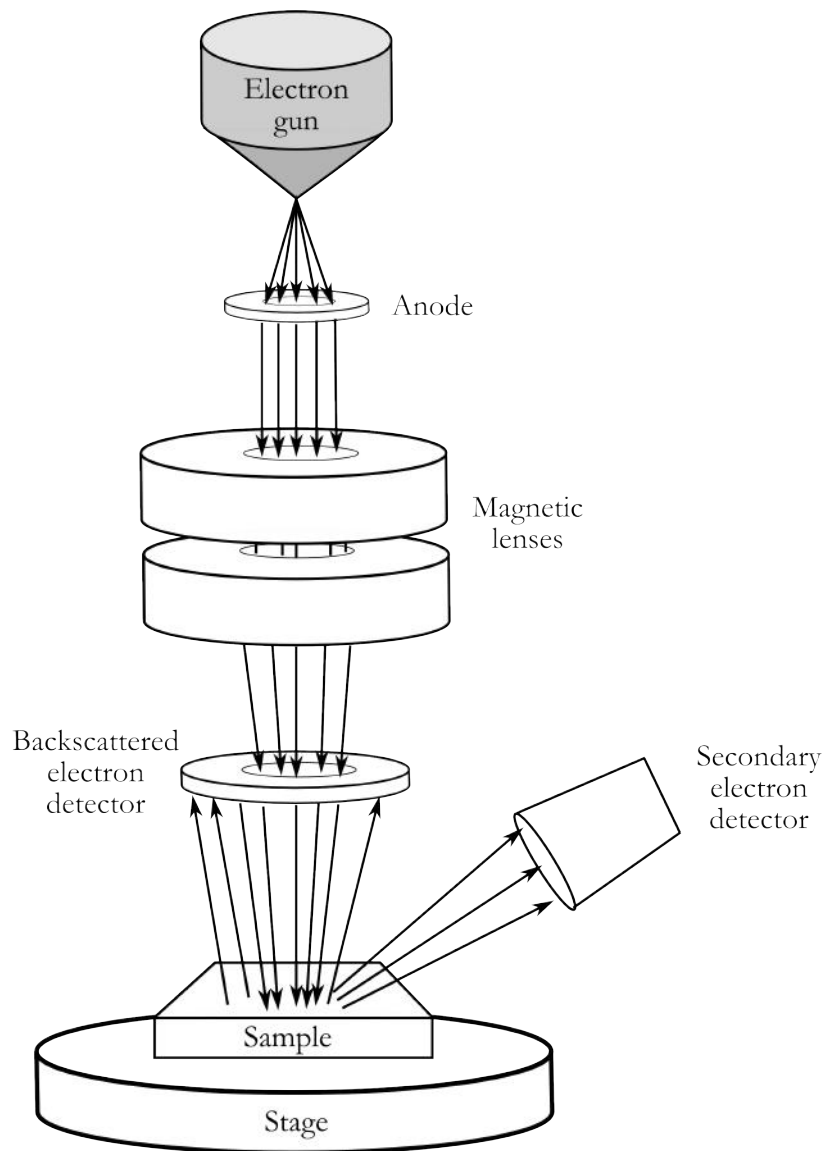


Figure 2.5: Schematic of the scanning tunnelling microscope with positions of the backscattered and secondary electron detectors (adapted from online source¹⁵).

2.3.5 Transmission electron microscopy

In a transmission electron microscope a beam of electrons is focused on a thin layer of sample and transmitted through it. The electron beam interacts with the sample and the forward scattered electrons are detected with a charge-couple device. The electron beam is scattered by the electron cloud and nuclei of the sample, and so charged particles scatter more strongly and an image is formed due to the variation in amount of electrons that are scattered and the intensity detected.

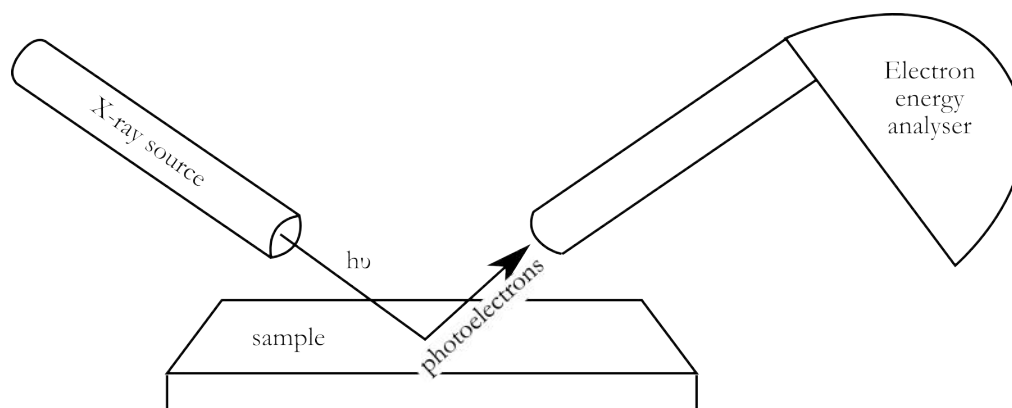
Samples of material were scrapped off the glass substrate and sonicated in *n*-hexane creating a suspension. The sample suspensions were then drop-casted onto a 400 Cu mesh lacy carbon film TEM grid (Agar Scientific Ltd) before use in the transmission electron microscope (TEM) machine. Images were taken using a Jeol 2100 HRTEM with a LaB₆ source operating at an acceleration voltage of 200 kv with an Oxford Instruments X-Max EDS detector running AZTEC software and micrographs were detected with a Gatan Orius CCD.

2.3.6 Energy dispersive x-ray spectroscopy

Energy dispersive x-rays (EDX) can be used in parallel with TEM and SEM imaging. With higher energy electron beam, electrons from the ground states are ejected leaving holes which are then filled by electrons from a higher energy levels, x-rays are released with an energy of the difference between the two orbitals, which are therefore characteristic to their elemental composition. The detector measures the intensity of emitted x-rays against their energy and can be used to determine the elemental composition of the sample.

2.3.7 X-ray photoelectron spectroscopy

Elemental analysis was also carried out with x-ray photoelectron spectroscopy (XPS) on a Thermo Scientific K Alpha with monochromated Al-K α source (0.834 nm, 1486.6 eV). X-rays are used to eject core shell electrons, the energies of which correspond to the core shells of a particular element (Figure 2.6). For Al-K α , electrons deeper than 10 nm away from the surface have a very low probability of escaping it without loss in energy, therefore XPS peaks are mainly contributed from the surface material. The chemical environment around an element can shift the energy levels, and so analysis of the XPS peaks and position can inform the user of the chemical environment surrounding the element of interest.



$$\text{Kinetic Energy} = h\nu - \text{Binding Energy} - \phi_{\text{spectrometer}}$$

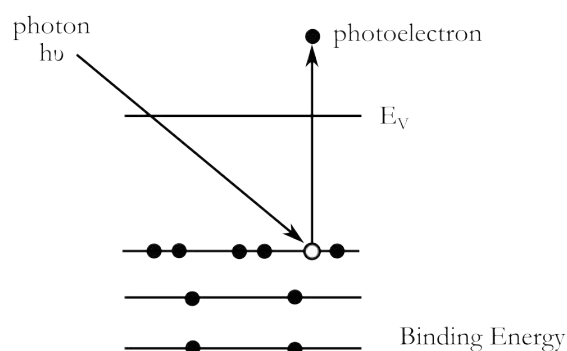


Figure 2.6: Schematic showing the layout of the x-ray photoelectron spectroscopy set up and the mechanism by which the photoelectron is ejected due to incoming x-rays (adapted from Auger- and X-Ray Photoelectron Spectroscopy in Materials Science: A User-Oriented Guide, Hofmann, S.¹⁶).

2.3.8 Gas chromatography

In gas chromatography (GC), the sample is vapourised and separated along a column allowing for quantitative analysis. GC experiments described in Chapter 4 were performed using a flame ionization detector (FID) Perkin Elmer Clarus[®] 500 GC. The analytes were ignited with H₂ gas and accelerated towards the collector which possessed a negative bias. Samples were extracted from the reaction mixture and stored in the fridge prior to measurement. An internal standard was used (dodecane) to calculate the component quantities.

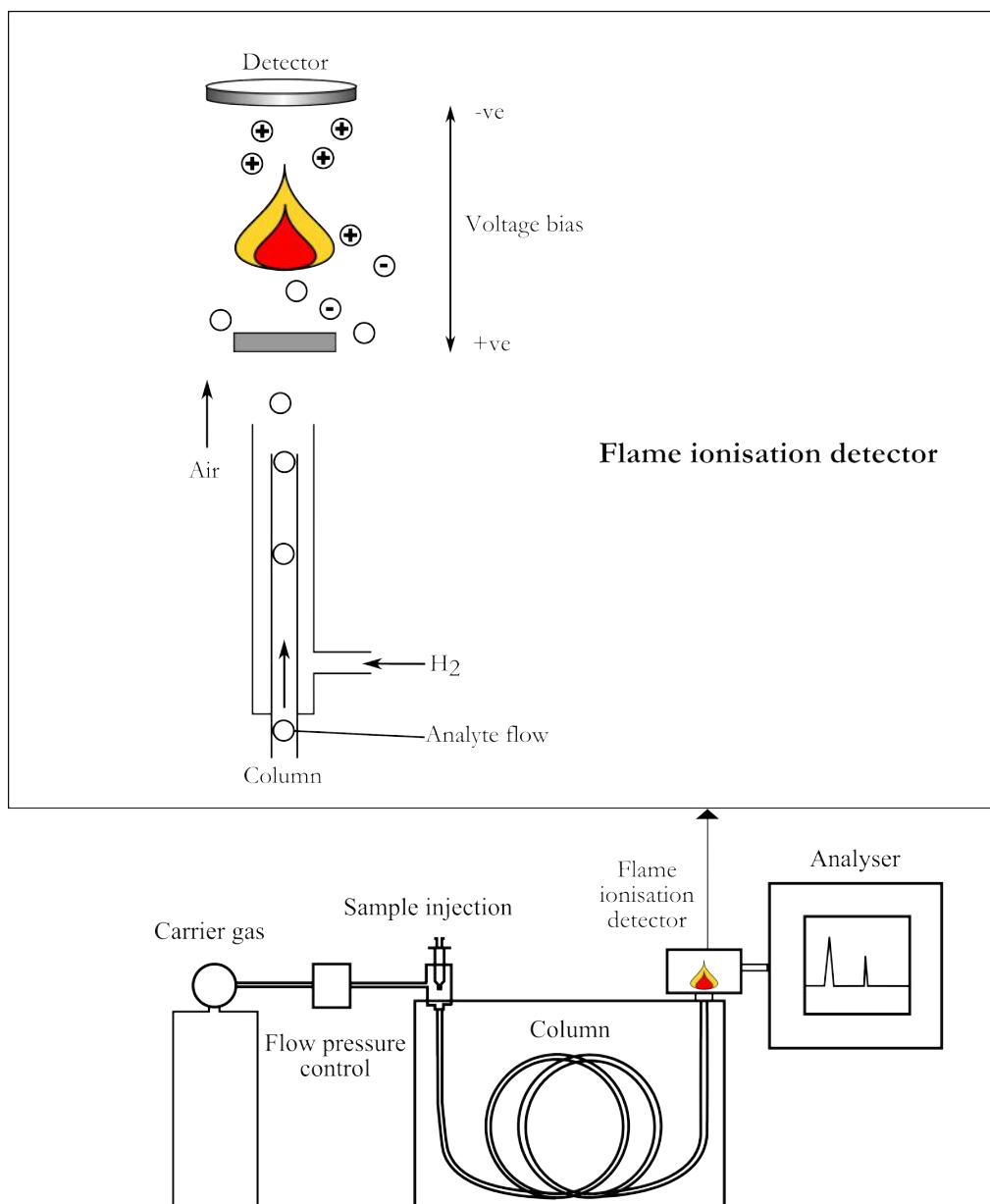


Figure 2.7: Component of a gas chromatography set up and a close-up of the flame ionisation detector (adapted from Basic Gas Chromatography, McNair, H. M. and Miller, J. M.¹⁷).

Chapter 3

Functional Composites of Gold Nanoparticles and Tin Dioxide

This chapter describes composite films of gold nanoparticles (AuNPs) and tin dioxide that were synthesised, combining their respective functional properties of surface plasmon resonance (SPR) absorption, transparency over the visible, high electronic conductivity, reflectance in the infrared region, while being relatively robust and easy to handle in ambient environment.

3.1 Introduction

Transparent conducting SnO_2 have been deposited using many different techniques such as spray pyrolysis, sol-gel, sputtering and chemical vapour deposition (CVD).^{72,199} In this chapter, aerosol-assisted chemical vapour deposition (AACVD) was used to make F-doped tin dioxide (FTO) from monobutyltin trichloride (MBTC) and ammonium fluoride (NH_4F) similar to previously reported experiments.^{69,79} The carrier gas and temperature was varied in order to improve the optoelectronic properties of the thin films.

Gold nanoparticle:metal oxide matrices have mostly been deposited in bulk

form or as thin films,^{12,177} they have also been synthesised as nanowires²⁰⁰ and nanocomposite particles.²⁰¹ A multi-target sputtering system was employed to form AuNP composites with dielectrics (TiO_2 and mixed ZnS-SiO_2) where a large third-order non-linearity was observed, useful for photonic devices.¹⁷⁷

More specifically for Au: SnO_2 composites, powders and nanoparticles have been synthesised for their use as gas sensors.^{195,196,202} Recently a thin film of SnO_2 embedded with Au nanoparticles were spin-coated from a sol-gel solution of SnO_2 coated Au nanoparticles ensuring a homogenous composite film.¹⁹² The AuNPs of around 15 nm were formed from a citrate reduction method before being coated with SnO_2 through stirring with sodium stannate trihydrate forming composite particles of around 55 nm. A SnO_2 sol was then prepared with the addition of the resulting composite particles and finally spin coated into a composite film, whereby the thickness can be increased through additional coatings. The films displayed transparency and SPR absorbances but the authors did not report high electric conductivity.

Similar AACVD systems have been shown able to deposit various AuNPs and metal oxide nanocomposites on glass in a single-step process using auric acid in the precursor solution.^{38,203} Hybrid AACVD and APCVD deposited Au:metal oxide composite films, where the addition of tetraoctylammonium-bromide (TOAB) was used to influence the size of the AuNPs.¹⁹⁰

3.1.1 Objectives

The work in this chapter aims to improve on the AACVD techniques previously used to deposit composite metal oxide nanoparticle films, by improving the control of AuNP deposition and quality of the optical and electronic properties not previously explored. Various precursor solutions will be tested, one-pot, with gold and tin oxide precursors together, or separately, where better

control and quality can be achieved. The AACVD procedure is closely related to the industrial way of coating glass and results in composite films containing metal oxides with desirable optoelectronic properties, not reported from other methods such as sol-gel¹⁹² and sputtering.¹⁷⁷ The properties of the films produced in this chapter focus on high visible transparency, low resistivity, a blue colouration potentially useful for window tint, SPR absorbances and adherence to the glass substrate which to our knowledge has not been explored.

3.2 Experimental details

3.2.1 Precursor solutions

Table 3.1 below shows the precursors required and used in this section to deposit SnO₂, F doped SnO₂, Au nanoparticles and AuNP:SnO₂ composite films. These were all one-pot solution depositions. The solvent (methanol) was added to the required precursor(s) and stirred till dissolution before aerosol generation. NH₄F was used instead of trifluoroacetic acid because it has been shown to effectively dope when used with MBTC (see Section 1.4.6).

Table 3.1: Precursors used for the relevant materials.

Materials	Precursors used
SnO ₂	MBTC (monobutyltin trichloride, CH ₃ CH ₂ CH ₂ CH ₂ SnCl ₃)
F doped SnO ₂	NH ₄ F + MBTC
Gold nanoparticles (AuNPs)	HAuCl ₄ .xH ₂ O (gold chloride hydrate)
AuNP:SnO ₂ composite	MBTC + HAuCl ₄ .xH ₂ O

3.2.2 Deposition details

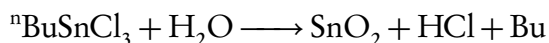
Aerosols were generated with an ultrasonic humidifier from the precursor solution contained in a glass bubbler. Carrier gas of pressurised air or N₂ was used to transport the vapour at a rate of 1-2 L min⁻¹ into the CVD reactor which was heated to 400-500 °C.

3.3 AACVD of SnO₂

SnO₂ was deposited from a solution of MBTC in methanol at different temperatures (400, 450 and 500 °C) with N₂ as the carrier gas (2 Lmin⁻¹). Methanol was used as a solvent as it has been shown to increase the density and conductivity of SnO₂.¹³⁹ All depositions took around 30 min resulted in transparent films with good coverage and adherence on the bottom plate. C contamination could be observed through the colouring and was found more often at higher temperatures concentrated and mostly close to the inlet evidenced by brown and black tinted depositions.

3.3.1 Phase and morphology

It is well known that the breakdown of MBTC is complicated and many products are formed, but due to the non-anhydrous nature of the reaction vessels it is possible that instead of reacting with methanol the reaction initiates with water as follows^{118,204}:



The XRD patterns for the films deposited at all three investigated temperatures were almost identical, apart from a slight increase in the (200) plane at 450 °C (Figure 3.1). The orientation of deposited planes can depend on a number

3. Functional Composites of Gold Nanoparticles and Tin Dioxide

of things, the initial reactions, consequent growth after the first few layers and the deposition rate, all of which are affected by the temperature of deposition. The deposition conditions and precursors at 450 °C induced an increase of Sn at interstitial sites in the SnO₂ lattice¹¹⁶ resulting in a slight increase in the (200) direction.

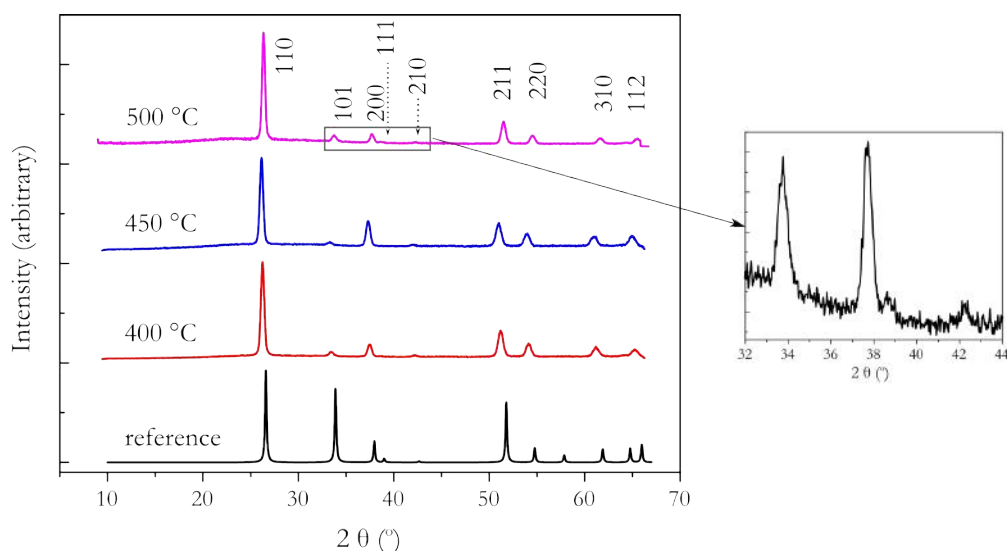


Figure 3.1: XRD pattern intensities of SnO₂ reference¹⁸ and thin films deposited at 400, 450 and 500 °C from a precursor solution of MBTC (2 mmol) in 20 ml methanol with N₂ (g) flowing at 2 L min⁻¹.

The most preferred growth for the films deposited at all temperatures was the (210) plane (Figure 3.2), which is normally suppressed in the single crystal.¹⁸ The (111) and (110) plane peaks were observed to be the second and third most dominant growth planes. The observed preferred orientation was unlike previously reported films whereby the majority of SnO₂ deposited using CVD or spray pyrolysis was found to be orientated along the (101),²⁰⁵ (111),⁷⁸ and (200) planes,^{78,133,206} probably due to the use of N₂ as a carrier gas and oxidation of Sn from the methanol precursor or water rather than abundant O₂ in the environment. No Sn(II)O peaks were observed indicating that oxygen was efficiently incorporated into the SnO₂ matrix from the methanol or any residual in the environment.

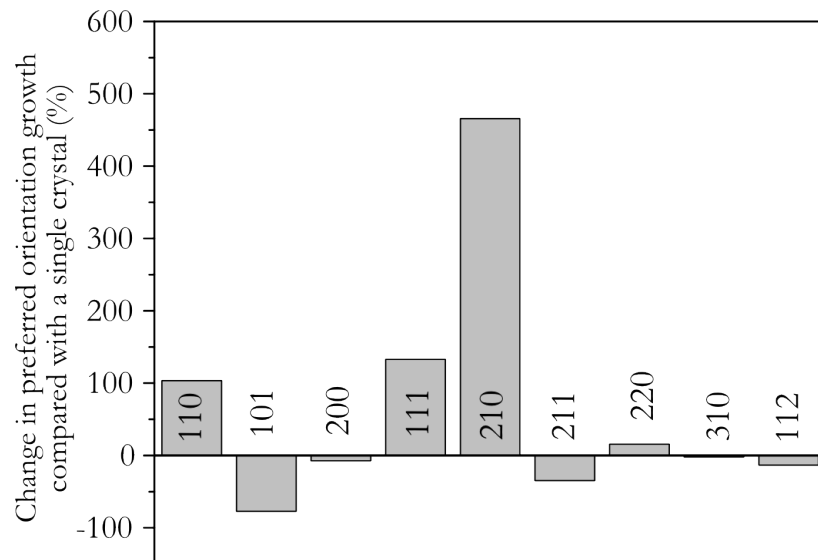


Figure 3.2: Percentage change in preferred growth of SnO₂ deposited at 450 °C from a precursor solution of MBTC (2 mmol) in 20 ml methanol with N₂ (g) at 2 L min⁻¹.

The SEMs (Figure 3.3) of the SnO₂ films show a similar surface morphology for all deposition temperatures reflecting the nearly identical XRD pattern for all three films. However the surface changed from being relatively flat on the surface to becoming more faceted and rough with increasing deposition temperatures probably indicating the increasing crystallinity.

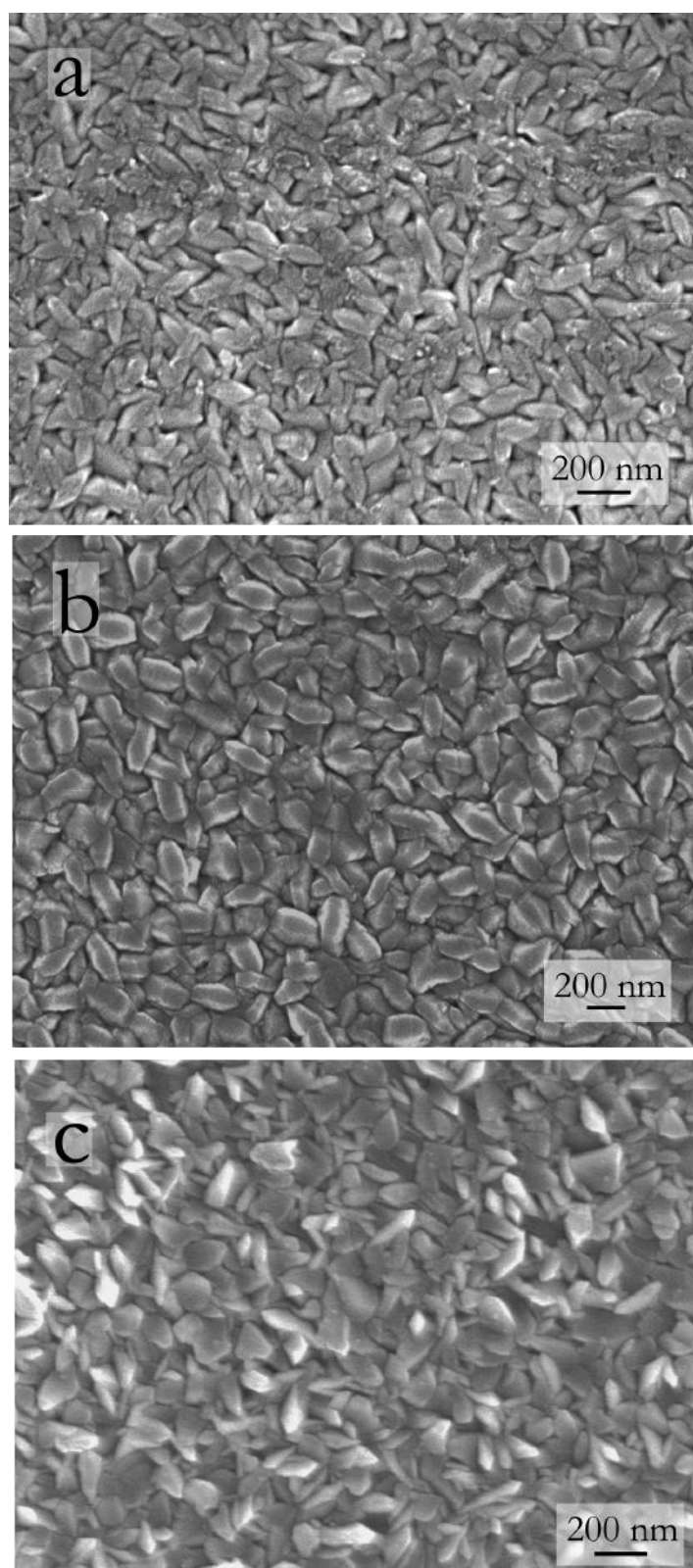


Figure 3.3: SEM images of SnO₂ thin film deposited at (a) 400, (b) 450, and (c) 500 °C from a precursor solution of MBTC (2 mmol) in 20 ml methanol with N₂ (g) flowing at 2 L min⁻¹.

3.3.2 Optical and electronic properties

The transmittance of the deposited SnO₂ films were fairly high, between 60 and 80% in the visible range (Figure 3.4 a). The sheet resistance was lowest for the film deposited at 500 °C at 100 Ω/□, compared to 250–400 Ω/□ for the films deposited at 400 and 450 °C. The higher conductivity corresponds to the reflection seen in the far IR (see Figure 3.4) which is a characteristic TCO property for low emissivity applications. The increase in conductivity here is related to the thicknesses of the films, with the film deposited at 500 °C being about 400 nm thick and the films deposited at 400–450 °C about 250–300 nm thick as measured by Filmetrics. However, the increase in conductivity can also be due to better electrical connectivity between the crystallites when they form at a higher temperature as seen by the increase in overlap in the SEM images (Figure 3.3). Theoretically, minimising the amount of oxygen in the reactor environment, through using N₂ rather than air, should encourage the formation of oxygen vacancies in the SnO₂ matrix and increase the conductivity of the thin film, however this was not observed with relatively poor conductivity when being considered for TCO purposes.

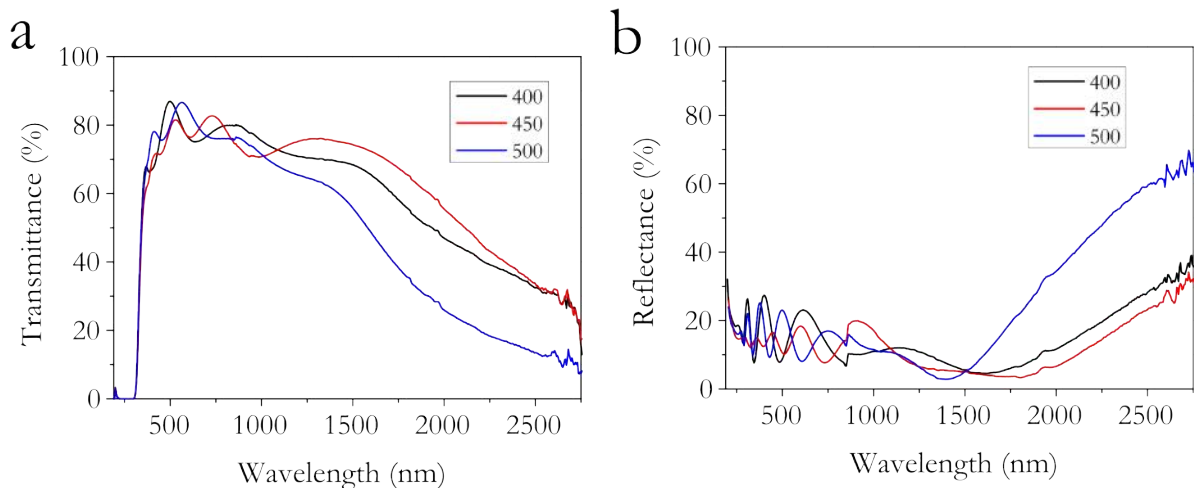


Figure 3.4: Transmittance and reflectance spectra of SnO₂ thin film deposited at 400, 450 and 500 °C from a precursor solution of n-butylin trichloride (2 mmol) in 20 ml methanol with N₂ (g) at 2 L min⁻¹.

3.3.3 Summary

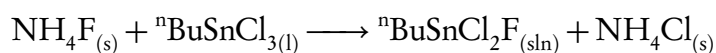
Even though the films were transparent and conductive, the sheet resistances were still quite high when comparing to industrial standards i.e. Pilkington Tec-8 at $8 \Omega/\square$. Depositing at a lower temperature produces a film that seems more transparent by eye, even though the transmittance spectra are pretty similar, as films deposited at a higher temperature suffered from slight carbon contamination, scattering and haziness caused by a rougher microstructure as seen in the SEM images (Figure 3.3). As a compromise, 450°C was decided as the best deposition temperature for SnO_2 in this system as with all other factors the same, it had both reasonable transparency as well as potential for increasing electrical conductivity. In order to improve the conductivity, gaseous oxygen could be introduced into the environment by using air as a carrier gas.⁷⁹ Gaseous O_2 is more reactive in the deposition chamber compared to the oxygen contained in the methanol of precursor droplets which needs more energy to atomise, so the reaction between the Sn and O happens earlier and more connectivity is developed within the SnO_2 crystallites. Less defects and disorder was formed leading to a lower level of scattering therefore also improving the transparency.^{79,207}

3.4 F doping and improving TCO properties

Fluorine doping has long been known to improve the TCO properties of SnO_2 as discussed in Section 1.2.4.²⁸ With this AACVD system it is easy to incorporate F into a host SnO_2 film simply by adding ammonium fluoride into the Sn precursor solution.^{69,79} The results presented here are of a fluorine doped tin oxide (FTO) film deposited from a 30 at.% F:Sn solution at 450°C with air (1 L min^{-1}) using NH_4F and MBTC as the precursors. AACVD of FTO achieved

good coverage across the glass substrate resulting in uniform transparent conducting films with small gradients in thicknesses of around 50 nm across the whole substrate.

Choosing the dopant for F can also affect the growth phase and final morphology as discussed in Section 1.4.5. Using ammonium fluoride and butyltin trichloride can result in an exchange process whereby the Cl in butyltin trichloride is replaced by F in some cases,⁷⁹ forming ammonium chloride and a fluorotin complex as shown below



This reaction is beneficial for the normally hard to achieve incorporation of F into SnO₂.

3.4.1 Phase and morphology

The FTO thin film (around 450 nm thick) displayed sharp SnO₂ reflections in the XRD pattern and a typical pyramidal microstructure as observed from SEM images (Figure 3.5). The FTO film adhered well to the glass, passed the Scotch[®] tape test and could not be rubbed off unless scratched with a metal spatula. A more crystalline morphology and XRD pattern was observed for FTO when compared to SnO₂, due to the more complete oxidation by using air, which contains O₂, rather than N₂ as the carrier gas. Using air and a F dopant in the deposition increased intensities for the (101), (200), and (211) and decreased the (110) reflections when compared to the undoped SnO₂ (Figure 3.2).

Preferred growth was found to be in the (200) and (210) planes (Figure 3.6) which correlate with low electrical resistivity of previous FTO studies.⁷⁹ The increase of (200) from SnO₂ to FTO agrees well with the decrease in sheet

resistance, from $100 \Omega/\square$ to $10 \Omega/\square$. The (200) plane also correlates with a sharper-edged morphology¹³³ that has better electrical connectivity. The (210) and (110) planes have both been found to be preferred in thin films formed in an AACVD system with methanol. The use of methanol compared to other solvents also seem to enhance the effect of deposition temperature with different preferred phases found for different deposition temperatures.⁷⁹

The growth of the (200) seems favoured for SnO_2 thin film deposition on glass based substrates as it this was found to be the preferred plane also for sprayed¹¹⁶ and APCVD films.⁷⁸ The (200) orientation has a low atomic density and a minimum interfacial energy for rutile SnO_2 , having been observed to be the preferred orientation even for sprayed SnO_2 thin films on a range of substrates.¹⁴²

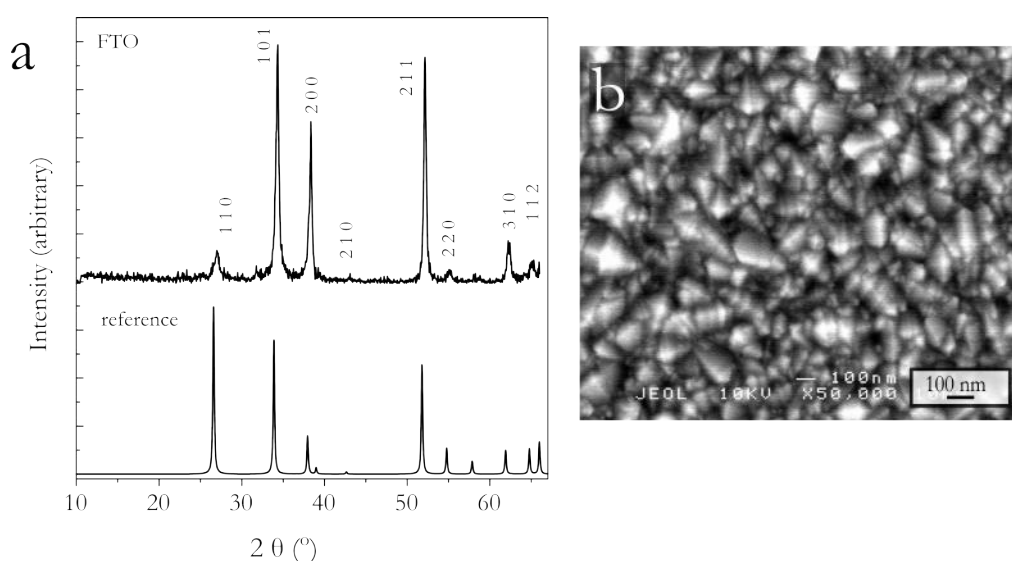


Figure 3.5: XRD pattern and SEM image of fluorine doped tin dioxide from a 30% ammonium fluoride to MBTC solution deposited in air.

3.4.2 Optical and electronic properties

The transmittance of the FTO film was high at around 70-80% in the visible region (see Figure 3.7) and also visibly transparent (Figure 3.23), even though the

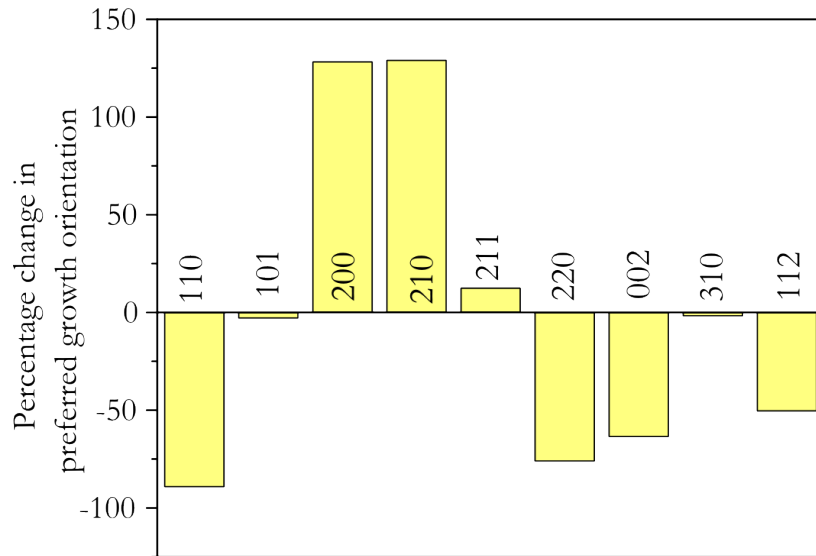


Figure 3.6: Percentage change in preferred growth of FTO deposited at 450 °C from a precursor solution of MBTC and NH₄F in methanol with air.

transmittance measurements were similar to SnO₂ deposited with N₂ (Figure 3.4), by eye the FTO film looked more transparent. This can be related to the increase in reflectance at the visible region, which is at 10-30% for SnO₂ (Figure 3.4) compared to 10-20% for the FTO (Figure 3.7) due to a small amount of carbon contamination or the haziness in the SnO₂.

Measurements using the Hall effect and Van der Pauw calculations show that the FTO thin film on glass is *n*-type with a charge carrier concentration of $4.9 \times 10^{20} \text{ cm}^{-3}$, mobility $25 \text{ cm}^2 (\text{V s})^{-1}$, sheet resistance $10 \text{ } \Omega/\square$ and resistivity $5.0 \times 10^{-4} \text{ } \Omega \text{ cm}$. These figures are comparable and in some cases exceed those of the leading commercial TCO for glass Pilkington TEC-8, which has a carrier concentration $5.3 \times 10^{20} \text{ cm}^{-3}$, mobility $28 \text{ cm}^2 (\text{V s})^{-1}$, sheet resistance at $8 \text{ } \Omega/\square$ and resistivity $5.2 \times 10^{-4} \text{ } \Omega \text{ cm}$. The electrical properties are in line with the reflectance spectra, displaying the characteristic plasma band onset of increased reflectance towards the IR (Figure 3.7) due to high charge carrier concentration and an interference pattern due to the thickness of the film.²⁰⁸ The FTO presented here possesses a near ideal transmittance and long wavelength

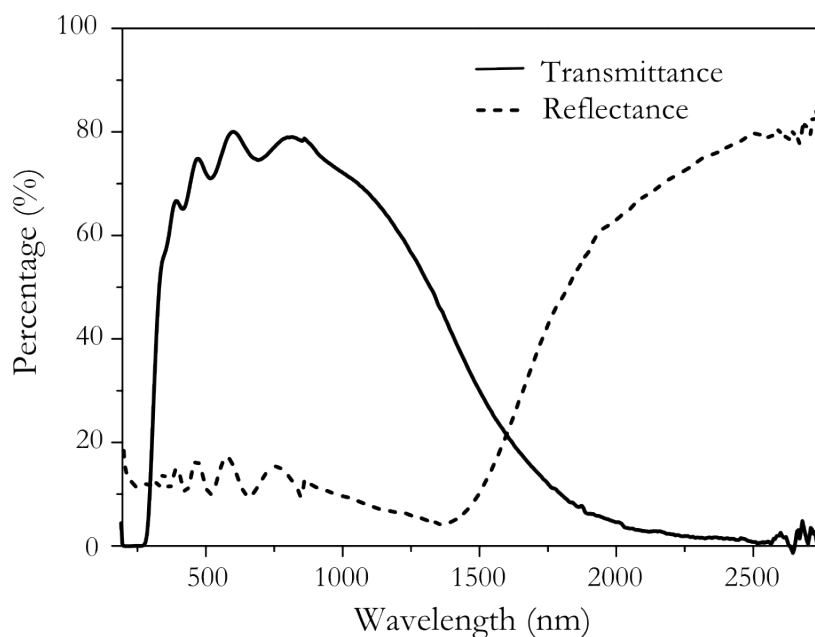


Figure 3.7: Transmission and reflection spectra of fluorine doped tin dioxide from a 30% ammonium fluoride to MBTC solution deposited with air.

reflectance profile for low emissivity coatings (Figure 3.7).

3.4.3 Summary

The precursor and AACVD deposition conditions here produced consistently high quality FTO film at industrial standards. This allows us to create composites with AuNPs that have guaranteed good TCO properties described in Section 3.7. By doping with F and using air as the carrier gas there were dramatic increases in conductivity compared to the SnO_2 deposited using N_2 whereby the sheet resistance was lowered from $100 \Omega/\square$ to $8 \Omega/\square$, but still maintaining the high transparency of 65-80% transmittance. Thin films of SnO_2 produced by other methods other than CVD seem to not produce simultaneously transparent and conductive films. When compared to FTO deposited by CVD, or specifically AACVD, the resistivity were very similar and in some cases better than previously reported, with high carrier concentrations in the order of 10^{20} cm^{-3} and mobility of around $20 \text{ cm}^2(\text{Vs})^{-1}$.^{78,79,109}

3.5 Investigation of auric acid depositions

Results of gold depositions from auric acid are reported in this section. In order to achieve good coverage of the glass substrate higher flow rates were needed for AuNP compared to SnO₂ based depositions. Auric acid reduces to gold at a lower temperature and depositions on the glass can accumulate by the inlet if temperatures are too high.

Different methods were tried in order to vary the sizes of nanoparticles being deposited, for example varying the temperature or the inclusion of various stabilisers, e.g. tetraoctyl ammoniumbromide (TOAB) to the precursor solution.¹¹² However for AACVD of AuNPs using gold chloride hydrate, changing the precursor concentration seems to give the best and uniform result of decreasing nanoparticle sizes. Details of the precursor concentrations are given in Table 3.2 and discussed in Section 3.5.3.

Due to thermophoresis (Section 1.3.2) the gold also deposits on the top plate, unlike most metal oxide depositions where deposition occurs almost exclusively on the bottom plate, under which the heating element is located due to a higher thermal activation energies. The difference in top and bottom plate depositions are discussed in Section 3.5.2.

Precursor solutions (20 ml) as described in Table 3.2 were placed in the bubbler and used straightaway for AACVD deposition using air as a carrier gas. Each deposition took around 30 minutes.

3. Functional Composites of Gold Nanoparticles and Tin Dioxide

Table 3.2: Different concentrations of auric acid in methanol used to deposit the gold nanoparticles and their corresponding SPR maxima and sizes determined from SEM images.

Amount of HAuCl_4 (mM)	SPR maximum (nm) of bottom plate substrate and top plate (nm)	Range of nanoparticles observed (nm)
0.25	535; 540	10-40
0.5	540; 560	30-50
1	545; 570	50-70

3.5.1 Phase and appearance

All the depositions from auric acid resulted in coloured AuNP thin films that displayed cubic metallic gold XRD patterns as in Figure 3.8.

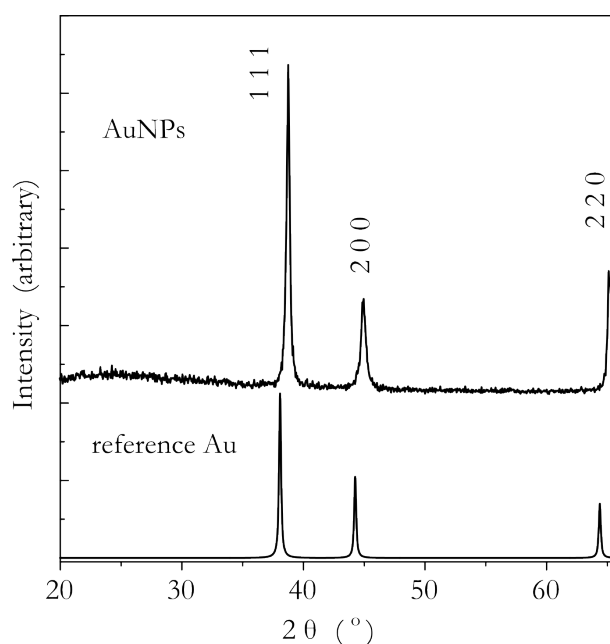


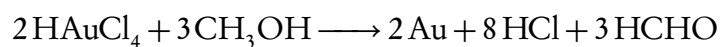
Figure 3.8: Typical XRD pattern of AuNPs deposited from auric acid using aerosol-assisted chemical vapour deposition with cubic gold reference¹⁹ for comparison.

3.5.2 Difference between top and bottom plates

From SEM images in Figure 3.9 it can be seen that in general the top plate gold nanoparticles formed in the CVD reaction of auric acid were slightly larger at

30 nm to 70 nm compared to the bottom plate nanoparticles at 20 nm to 60 nm. Larger particles were observed more often on the top rather than bottom plate as when NPs form in between the plates, they are more susceptible to thermophoresis and are pushed upwards due to convection in the reactor eventually settling on the top plate. The larger sizes of the top plate particles corresponded to observations of SPR absorption maxima at longer wavelengths.²⁰⁹ Even though the top plate nanoparticles were larger, there were fewer nanoparticles observed in the SEM, since a larger area of glass can be observed from SEM images.

Thermogravimetric analysis of HAuCl_4 showed a loss of HCl between 80 and 110 °C followed by a loss of $3/2 \text{ Cl}_2$ between 150 °C and 200 °C.³⁸ However, since MeOH is also present in the reaction, the reaction could also possibly proceed as below.



AuNPs are formed when auric acid is reduced by methanol in the reactor where the temperature is high enough for reaction activation. So even though reduction and NP formation can occur in between the plates, overall AuNPs will form more readily near the heated bottom plate substrate, therefore a higher number of depositions occur on the bottom plate and it is where we observe a higher concentration of AuNPs as seen from SEM images (Figure 3.9).

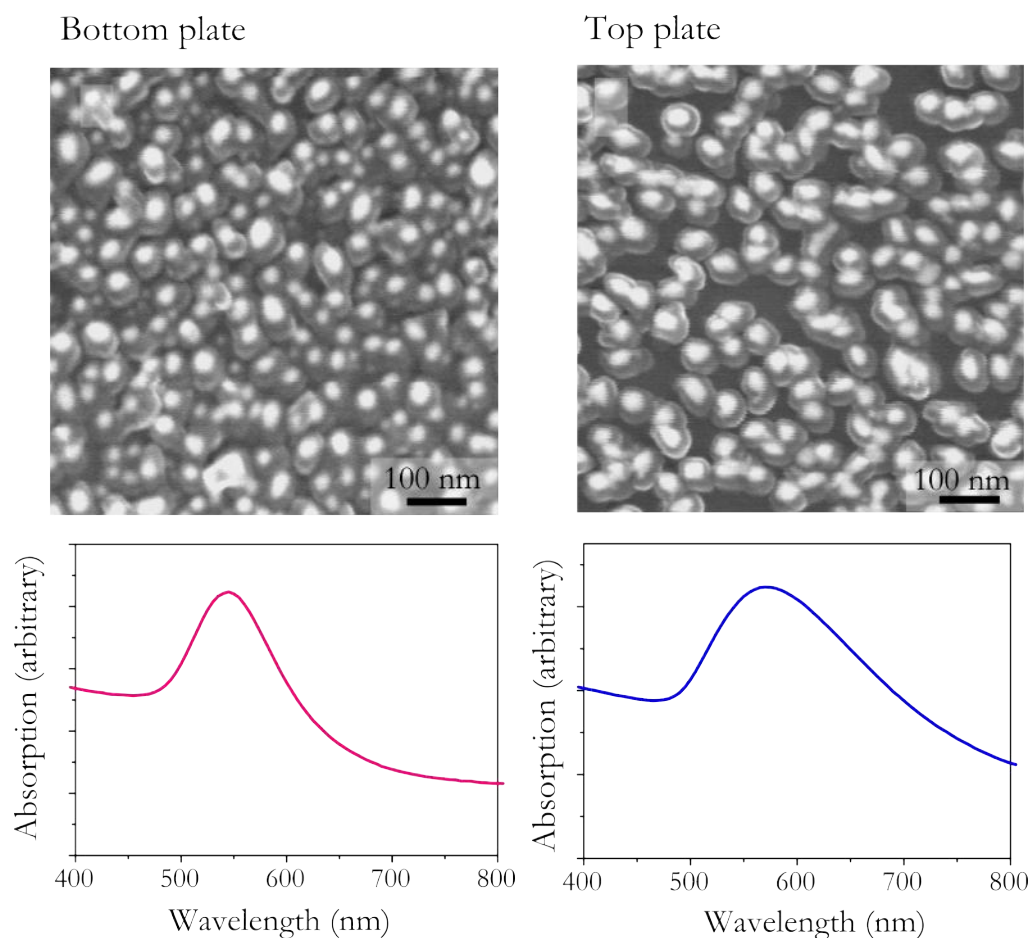


Figure 3.9: Comparison of films deposited on bottom and top plate from the AACVD reaction of auric acid (0.02 mmol) in methanol (20 ml) with air (2 L min^{-1}) at 450°C . Shown here are SEM images and SPR maxima observed from the absorbance spectra at 545 nm (bottom plate) and 570 nm (top plate). The spherical shapes of the nanoparticles can be seen in the SEM images and the sizes were estimated from this.

3.5.3 Changing the auric acid concentration

Gold nanoparticles were deposited from a range of auric acid precursor concentrations (Table 3.2) resulting in nanoparticle with a range of sizes. Depositions from higher concentrations of gold in the precursor solution resulted in larger and more irregular sized particles with a larger dispersity as seen in the TEM images (Figure 3.11). The SPR of nanoparticles deposited from higher auric acid concentrations were observed at longer wavelengths (Figure 3.10), similar to NPs deposited on the top plate as shown in Table 3.2.

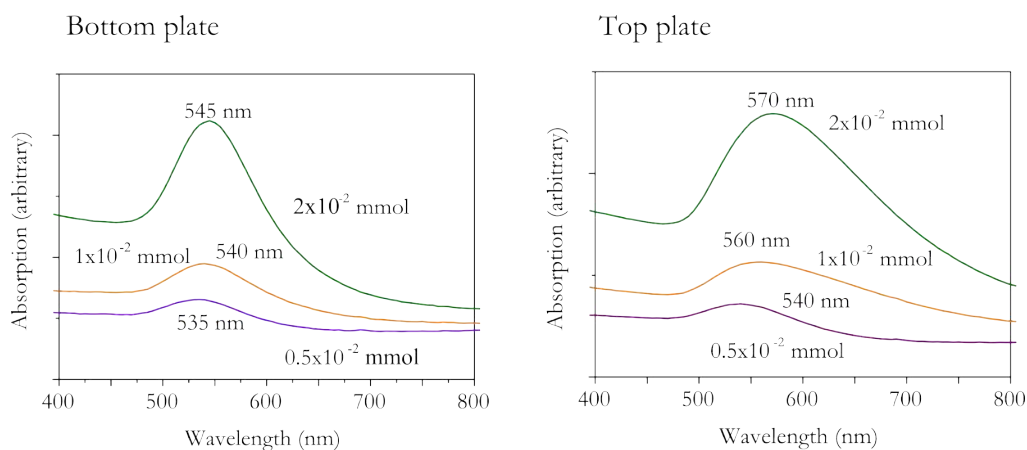


Figure 3.10: Surface plasmon resonance maxima of a gold nanoparticles deposited on the top and bottom plate from various concentrations of 0.05, 1 and 2×10^{-2} mmol in 20 ml methanol at 450 °C.

As the concentration of auric acid used in the precursor solution was lowered, the resulting nanoparticles became smaller and more spherically uniform, decreasing to 10 nm (see TEM images in Figure 3.11). The reduction of nanoparticle sizes were only seen on the bottom plates, all the top plate nanoparticles still had large size variations and irregularly shapes. The amount of nanoparticles on the top plate however, did decrease in correlation with decreasing auric acid concentration. Since it seems that the thermophoresis only affects a certain type of nanoparticle, large and irregular sized, it can be postulated that these nanoparticles are all formed by the same mechanism, when suspended in between the two plates not on the bottom plate surface, otherwise their presence would have also been observed on the bottom plate.

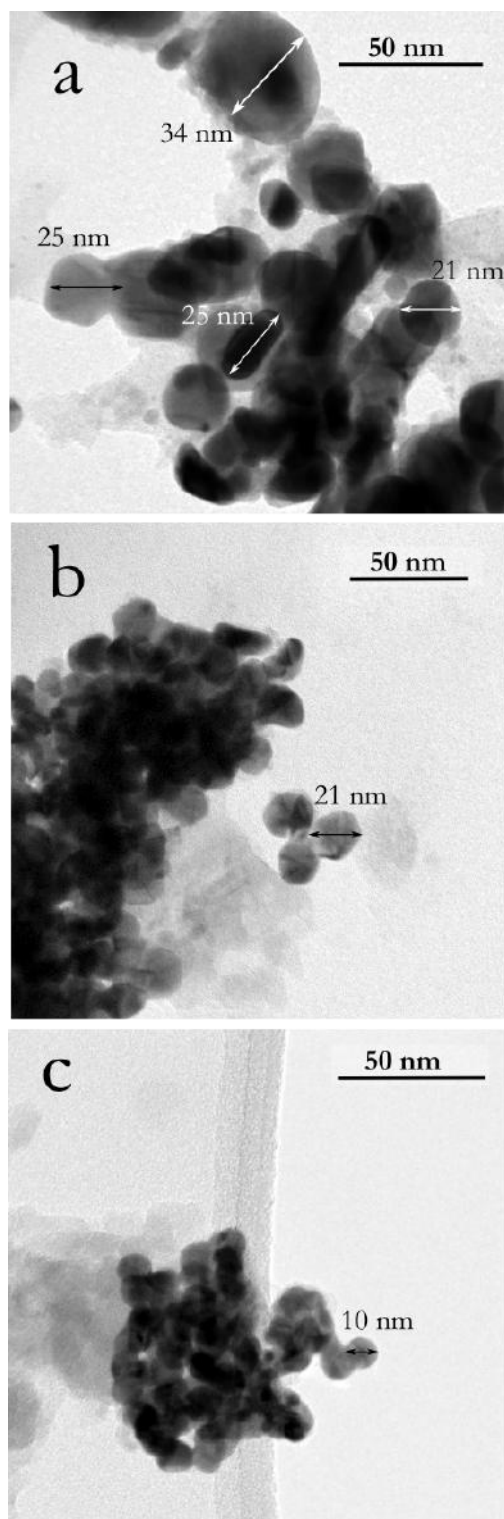


Figure 3.11: TEM images of AuNPs deposited on the bottom plate from auric acid concentrations of (a) 2×10^{-2} , (b) 1×10^{-2} and (c) 0.5×10^{-2} mmol in 20 ml methanol.

3.5.4 High auric acid concentration depositions

Composites of AuNP:SnO₂ deposited from one-pot solutions of auric acid and MBTC at different ratios are discussed in Section 3.6. The concentration of auric acid used for the one-pot AuNP:SnO₂ depositions, 6 mM of auric acid in methanol, was much higher than the auric acid reactions described in Section 3.5.3 (up to 1 mM). Results in this section describe depositions using that higher concentration of auric acid but without the Sn component. The auric acid was dissolved into methanol to make a 6 mM solution, 20 ml was placed in a bubbler used for deposition at 450 °C with N₂ at a rate of 2 L min⁻¹.

As observed from the photograph in Figure 3.12 there is a gradient of Au concentration on the glass substrate, with a higher concentration closer to the inlet of orange deposits indicating absorptions from bulk gold. The concentration of gold decreases while moving further from the inlet where instead there is a purple colour due to gold nanoparticless. The intensity of purple lessens moving away from the inlet due to precursor depletion, but is still of a higher intensity compared to depositions using a lower precursor concentration as in Section 3.5.3.

From the SEMs (Figure 3.13) it was observed that the films were discontinuous, having either particulate or island morphology. A discontinuous morphology indicates that the deposition of NPs occurs first at random locations on the glass, which could serve as nucleation points where more Au can then deposit on it. Since there seems to be overlapping particles on the bottom plate, but still the presence of the characteristic nanoparticulate SPR absorption, it is likely that the reduction into gold occurs mostly in the aerosol before deposition onto the substrate, with no particle diffusion that would occur when forming a continuous film. Reactions of auric acid into AuNPs and deposition onto the glass substrate were more efficient than in the one-pot Au:Sn deposi-

3. Functional Composites of Gold Nanoparticles and Tin Dioxide

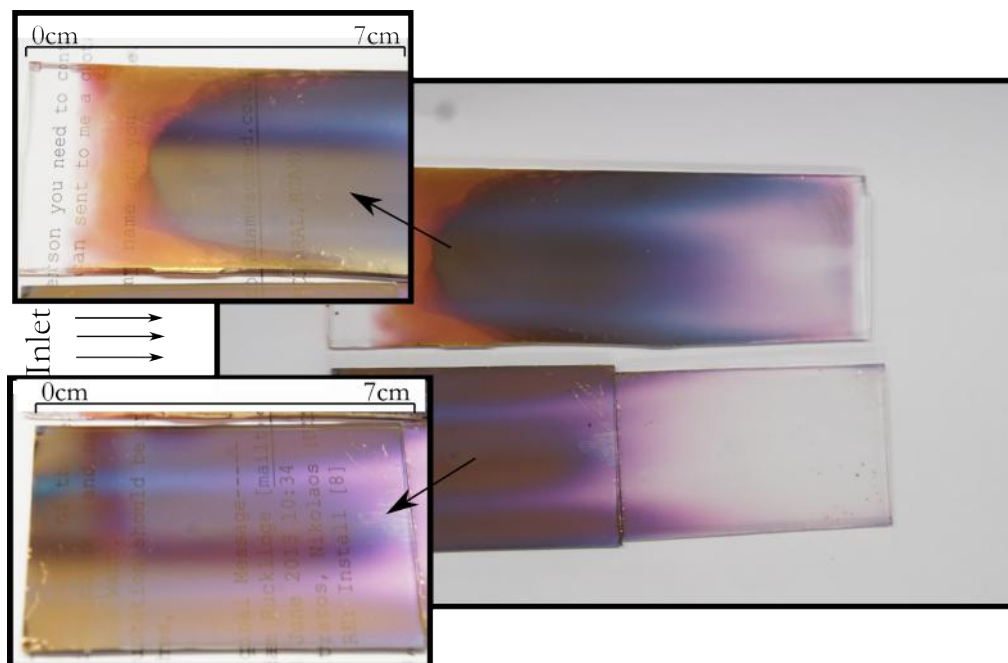


Figure 3.12: Photographs of AuNPs deposited from a 20 ml solution of 6 mM auric acid in methanol. Even though the concentration of Au was high, it still maintained nanoparticulate nature as seen by the purple colour with transparency - note that text can be seen through it.

tion described in Section 3.6, as there were more observed AuNPs on both the top and bottom plate.

The AuNPs deposited from this relatively highly concentrated solution were in general larger and less spherical than the nanoparticles deposited from a lower precursor concentration described in Section 3.5.3. In terms of optical properties (Figure 3.14), the gold films possessed a broad reflectance from 500 nm and onwards towards longer wavelengths characteristic of the metallic reflectance. There was a strong absorbance from the SPR, resulting in the blue and purple colour when looking through the film, which was of a higher intensity than when depositing with the Sn precursor in the one-pot solution (Section 3.6).

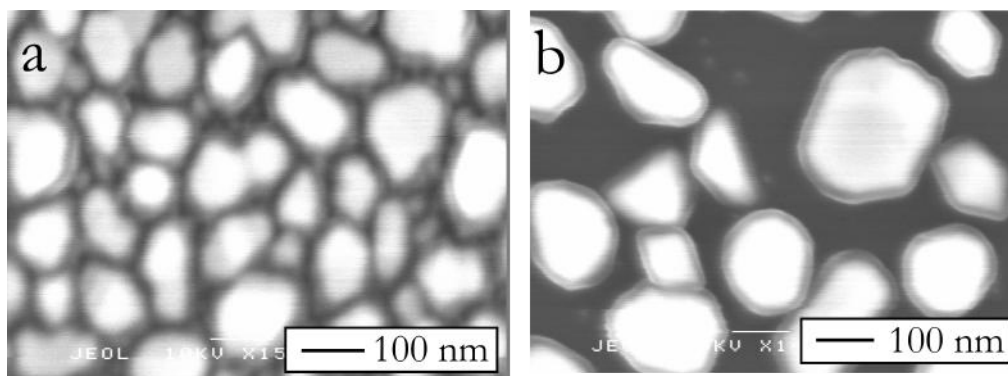


Figure 3.13: SEM images of gold deposited from an auric acid solution (6 mM) by AACVD. Images show showing island growth on the (a) bottom plate and large particle deposition on the (b) top plate.

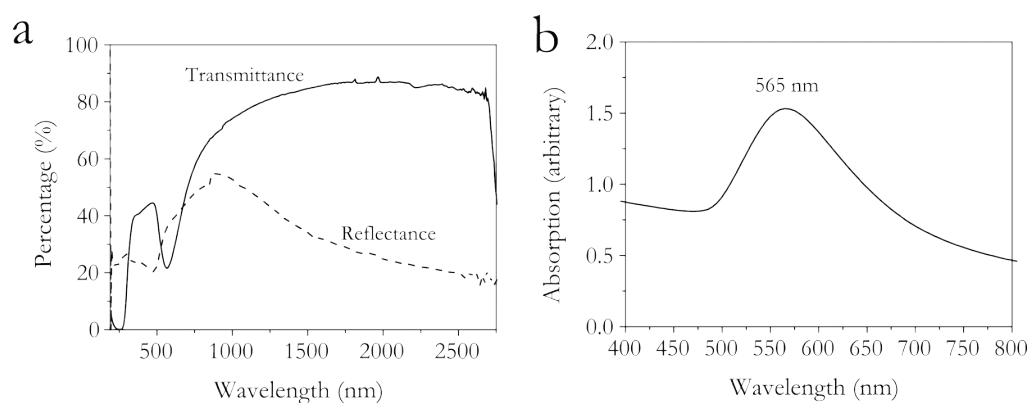


Figure 3.14: Optical properties of a typical gold nanoparticle film: (a) transmittance, reflectance and (b) SPR absorption.

3.5.5 Summary

AuNPs can be synthesised and deposited as a thin film onto glass with AACVD. Furthermore, we can control the depositions by controlling the auric acid precursor solution, allowing the properties of the nanoparticles that were deposited on the bottom plate to be optimised according to the application moreso than for the one-pot AuNP:SnO₂ composite depositions discussed in Section 3.6. By depositing the AuNPs by itself, rather than *in situ* with a metal oxide, different metal oxide composites can be synthesised without having to consider complicated interactions between the auric acid and metal oxide precursors in the precursor solution and during the reaction in the reactor. Compared to

other pure auric acid CVD investigations, where the Au film possessed SPR absorption from nanomorphological features,¹¹² the NPs synthesised here were smaller having a more discrete individual nanoparticulate nature as if synthesised using bench top methods.

3.6 One-pot solution AACVD of AuNP and SnO₂ composites

Ideally a composite synthesised from CVD would be made from a one-pot precursor solution to increase ease of preparation. In this section composites of nanoparticulate Au embedded within a thin film of SnO₂ were generated from a one-pot solution of auric acid and MBTC. Gradation of Au content in the films was useful in allowing the analysis of different compositions and combinations from a single CVD experiment. Reaction pathways can also be derived from the deposition patterns. Auric acid was dissolved into methanol with varying amounts of MBTC, stirred thoroughly then used shortly afterwards in the AACVD reactions. Some of the one-pot depositions showed mostly metallic gold or none at all, and through judging by appearances the Au:Sn precursor ratio showing the most efficacious incorporation of nanoparticulate gold into SnO₂ (5.6 at.% Au:Sn) which was further investigated in terms of deposition temperature.

3.6.1 Film appearance

Most of the films deposited, as per the conditions shown in Table 3.3 displayed the same colours with metal-like reflectivity despite using different precursor concentrations (i.e. Au:Sn ratio). However, the intensity of colours did change depending on the ratio of Au:Sn and sometimes displaying full bulk gold re-

Table 3.3: Different compositions of one-pot precursor solutions for the deposition of gold and SnO₂ thin films. All depositions were carried out using precursor solutions of auric acid in varying concentrations with butyltin trichloride (2 mmol) in methanol (20 ml).

Auric acid (mmol)	Au:Sn (at%)	Temperature °C
0.4	16.7	500
0.2	9.1	500
0.12	5.6	400, 450 & 500
0.1	4.8	500

flectance at high concentrations (Figure 3.15). The films deposited at 400 and 450 °C tended to cover the whole substrate, but at a higher temperature of 500 °C the breakdown of precursors occurs faster, so reaction, formation and deposition of SnO₂ was concentrated near the aerosol inlet (Figure 3.15).

The depositions on the top plates tended to be powdery and non-adhesive which indicated that the material has little intermolecular interaction with the silica coated glass. The top plates appeared to have a gold metal-like reflectivity, shades of purple in reflected light and shades of blue and orange in transmitted light. The colouration and low adhesion of the top plate films suggests that they are composed of mostly gold nanoparticles with little or no SnO₂. On the bottom plates, depositions were generally adhesive provided the films were less than 1 µm thick. Likewise the colours of the bottom plates were dark blue/black when viewed in transmitted light and purple in reflected light indicating the presence of gold. Better adhesion of the film to the glass substrate on the bottom plates indicated that it consisted also of a large part SnO₂, whilst the colour is due to the presence of gold nanoparticles within the metal oxide composite since tin oxide depositions are colourless or white.

3.6.2 Deposited phase

In order to have a look at deposition pathways, XRD patterns were obtained at 5 interval distances away from the inlet (Figure 3.16). As expected on the bottom plate, SnO₂ reflections were the main peaks detected. The intensities indicate crystalline SnO₂ depositions were most favourable about 3 cm from the inlet (Figure 3.16). Sharp peaks correlate with a thicker film whilst a higher background can be accounted for by a thin deposit (less than 200 nm). On the other hand, for the top plate cubic Au peaks were detected. The maximum intensities for the Au peaks on the top plate were detected 1 cm from the inlet before decreasing with increasing distance. A higher background can be seen on the top plate XRD patterns which come from the nanoparticulate morphology and underlying amorphous glass at places of low coverage. The proximity of Au deposition to the inlet and the absence of Au depositions in the baffle (see Figure 2.1) suggest that nanoparticles form as soon as precursor droplets enter the reactor, these nanoparticles are immediately affected thermophoretically resulting in top plate depositions close to the inlet. Most of the XRD patterns observed only show either SnO₂ or cubic metallic Au peaks. On the other hand SnO₂ forms more readily on the bottom plate, indicating that MBTC has a higher thermal activation energy for decomposition.

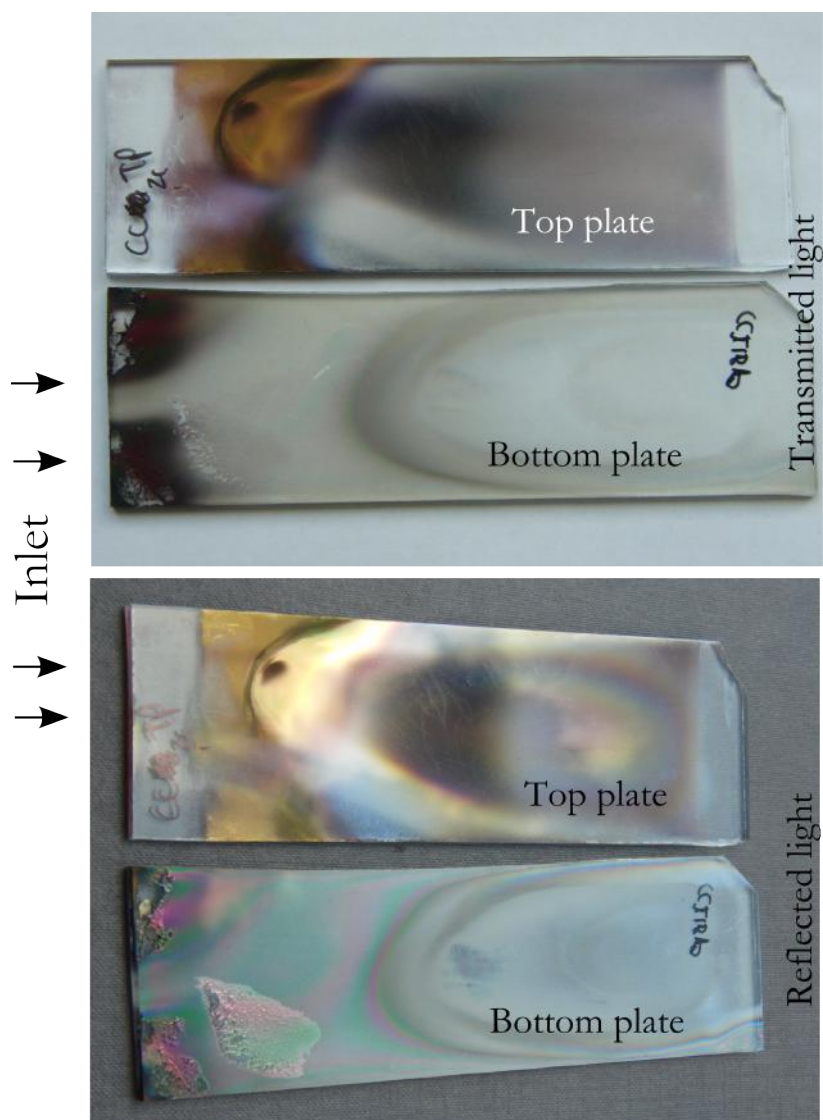


Figure 3.15: Photographs showing the top and bottom plate of a gold and tin dioxide composite film in transmittance and reflectance mode deposited at 450 °C from a one-pot solution of monobutyltin trichloride and auric acid in methanol.

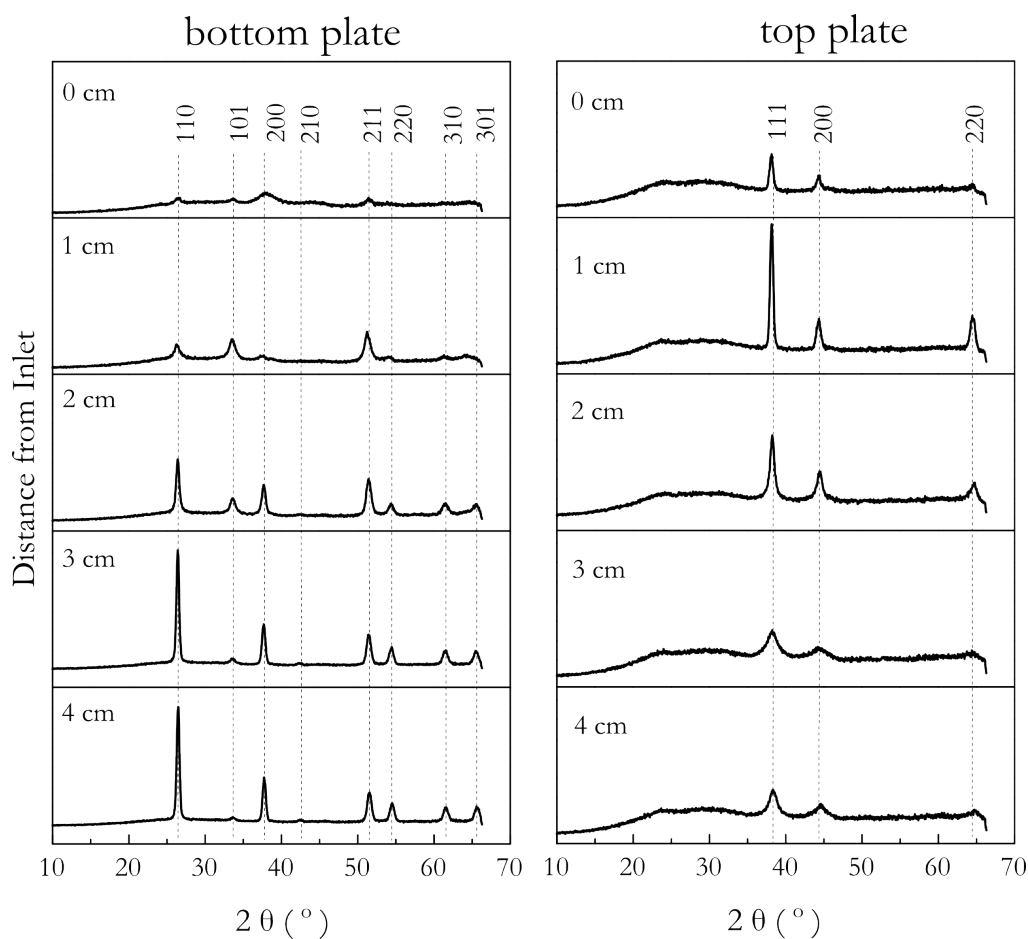


Figure 3.16: Intensities of XRD patterns taken at 0, 1, 2, 3 and 4 cm away from the inlet of a bottom and top plate deposited from a precursor solution of MBTC (2 mmol) and auric acid (0.12 mmol) in methanol (20 ml) at 450 °C with N₂ (g) carrier gas.

Table 3.4: Data measured at from different points of 0, 4 and 8 cm away from the inlet (Figure 3.17) on the bottom plate of films deposited from a 20 ml methanolic solution of 100 mM MBTC at 500 °C and together with 6 mM H₂AuCl₄ at 400, 450 and 500 °C. Deposited Au:Sn atomic ratios were determined using EDX and the corresponding SPR maximum where existent.

Precursor(s)	Temperature (°C)	Point	Au:Sn (at.%)	SPR maxima (nm)	XRD phase	SnO ₂ unit cell a = b; c (Å)	Unit cell volume (Å ³)
MBTC	500	-	-	-	SnO ₂	4.75 ; 3.19	72.03
MBTC and H ₂ AuCl ₄	500	a	47.1	559	Au/SnO ₂	4.73 ; 3.21	71.75
		b	14.3	555	SnO ₂	4.74 ; 3.18	71.40
		c	-	-	SnO ₂	4.77 ; 3.19	72.71
	450	a	53.5	570	Au	-	-
		b	11.5	551	Au/SnO ₂	4.77 ; 3.20	72.73
		c	8.3	558	SnO ₂	4.74 ; 3.16	71.21
	400	a	49.5	597	Au	-	-
		b	21.3	517	Au	-	-
		c	-	-	SnO ₂	4.78 ; 3.19	72.99

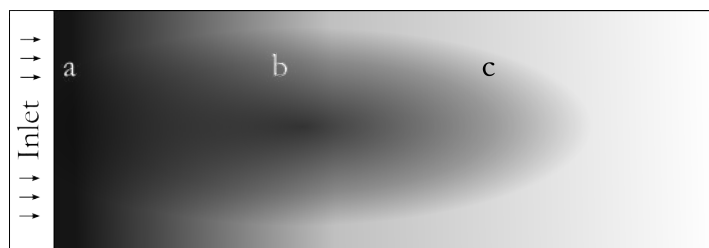


Figure 3.17: Points of 0, 4 and 8 cm away from inlet at which samples of bottom plate depositions at different temperatures from a one-pot precursor solution of auric acid and MBTC were measured for the values in Table 3.4.

Au:Sn atomic ratios of the deposited film were calculated from EDX. It showed a varied deposition of gold to tin ratios on the bottom and top plate. With low Au metal atomic deposition (around under 10 at.%), the Au peaks do not show up in the XRD. On the other hand films with high Au metal at.% (deposition over around 40 at.%) only peaks from cubic metallic Au were observed. Sometimes both peaks can be seen in the XRD pattern if the amount of Sn and Au is sufficiently high as in Figure 3.18. The lattice parameters were computed by fitting a Le Bail model to the patterns using the general structure analysis system (GSAS). Stoichiometric tin dioxide powder has a tetragonal rutile structure and crystallises in the space group $P4_2/mnm$. The cell parameters used for modelling were $a = b = 4.747 \text{ \AA}$ and $c = 3.185 \text{ \AA}$. The calculated unit cell are all similar to this as shown in Table 3.4.

An example XPS spectrum for a deposition at $500 \text{ }^\circ\text{C}$ is shown in Figure 3.19. The Sn 3d peaks display a spin orbit coupling of 8.4 eV and the binding energy of the $3d_{5/2}$ was observed at 486.8 eV, in good agreement to the reported range of 486.95-487.30 eV.^{205,210,211} XPS also confirmed that gold deposition occurred on both the bottom and top plate but the quantity was dependent on location (see Table 3.4). The Au $4f_{5/2}$ XPS peak from the nanoparticles was located at 84.1 eV, in good agreement with elemental gold reference values at 84.00 eV and 84.04 eV.^{212,213} On the bottom plates, XPS gave no evidence for Sn being incorporated into the gold nanoparticles or for gold substituting into

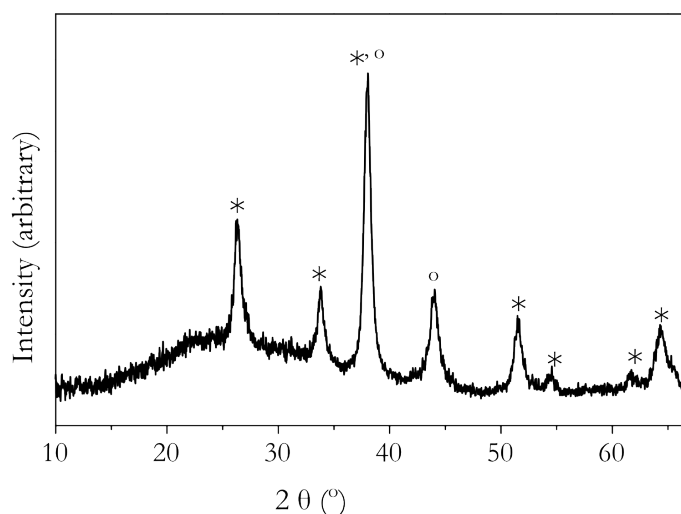


Figure 3.18: XRD pattern of a film deposited at 500 °C with a precursor solution of MBTC (2 mmol) and auric acid (0.12 mmol) in methanol (20 ml) with N₂ (g) carrier gas. This is an example of both the Au and SnO₂ peaks showing. The peaks labelled are for SnO₂ (*) and Au (°).

the SnO₂ lattice. The XPS data agreed with EDX and UV-Vis spectroscopy of the presence of mostly Au on the top plate as SnO₂ was only detected there for depositions at 500 °C.

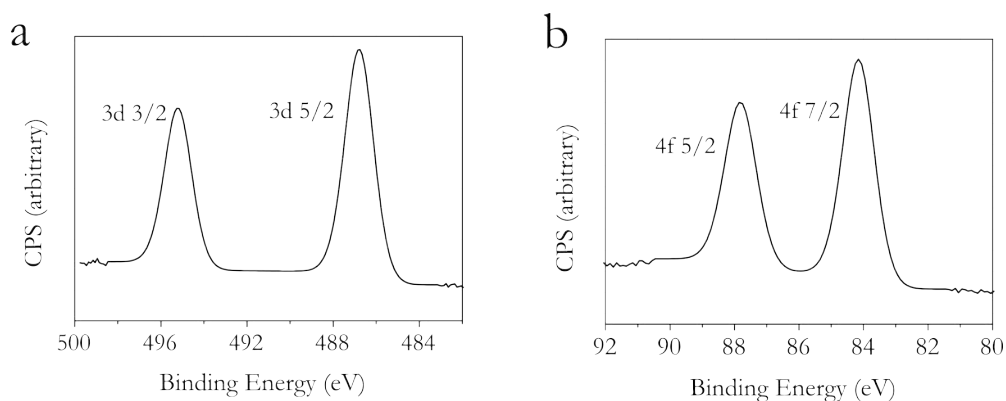


Figure 3.19: Photoemission spectra of the Sn 3d_{3/2} and 3d_{5/2} (left) and Au 4f_{5/2} and 4f_{7/2} binding energies of samples deposited at 400, 450 and 500 °C from a precursor solution of MBTC (2 mmol) and auric acid (0.12 mmol) in methanol (20 ml) with N₂ (g) as the carrier gas.

3.6.3 Surface morphology

SEM images in Figure 3.20 show a range of clustered to faceted structures which were taken from three regions investigated of a bottom plate deposition (Figure 3.17). The faceted structures corresponded to sharp SnO₂ peaks in the XRD pattern (Figure 3.18) and are found in other similarly polycrystalline SnO₂ thin films.⁷⁹ The films which were more cluster-like had a higher Au:Sn ratio which corresponded to less sharply defined XRD reflections as the presence of AuNPs within the SnO₂ disrupts the crystallinity. The morphological trend from faceted to clusters were observed to accompany decreasing deposition temperature and increasing gold precursor.

Films deposited on bottom plates at high temperatures were observed to have a more faceted crystalline SnO₂ morphology, possibly because the thermophoretic effect is larger and any AuNPs formed are moved upwards towards the top plate, as well as higher temperatures should produce more crystalline films as the atoms have more energy to move towards more stable sites. At a higher Au:Sn precursor ratio or at lower deposition temperatures, more gold nanoparticles or compounds will be present in the reactor by the bottom plate which might interrupt crystalline SnO₂ formation, resulting in clusters rather than crystalline facets. AuNPs were observed on the top plate of films, with less than a monolayer deposited at 400 and 450 °C, which increased to blanket coverage for films deposited at 500 °C (Figure 3.21). As mentioned before, thermophoresis has a larger effect on larger particles, which indicates that during the AACVD reaction gold atoms are aggregating and forming nanoparticles in between the plates prior to deposition. As with XRD patterns, the AuNPs cannot be seen in the SEM images of the bottom plates even when an SPR absorption was present, indicating they are embedded within the SnO₂ host matrix.

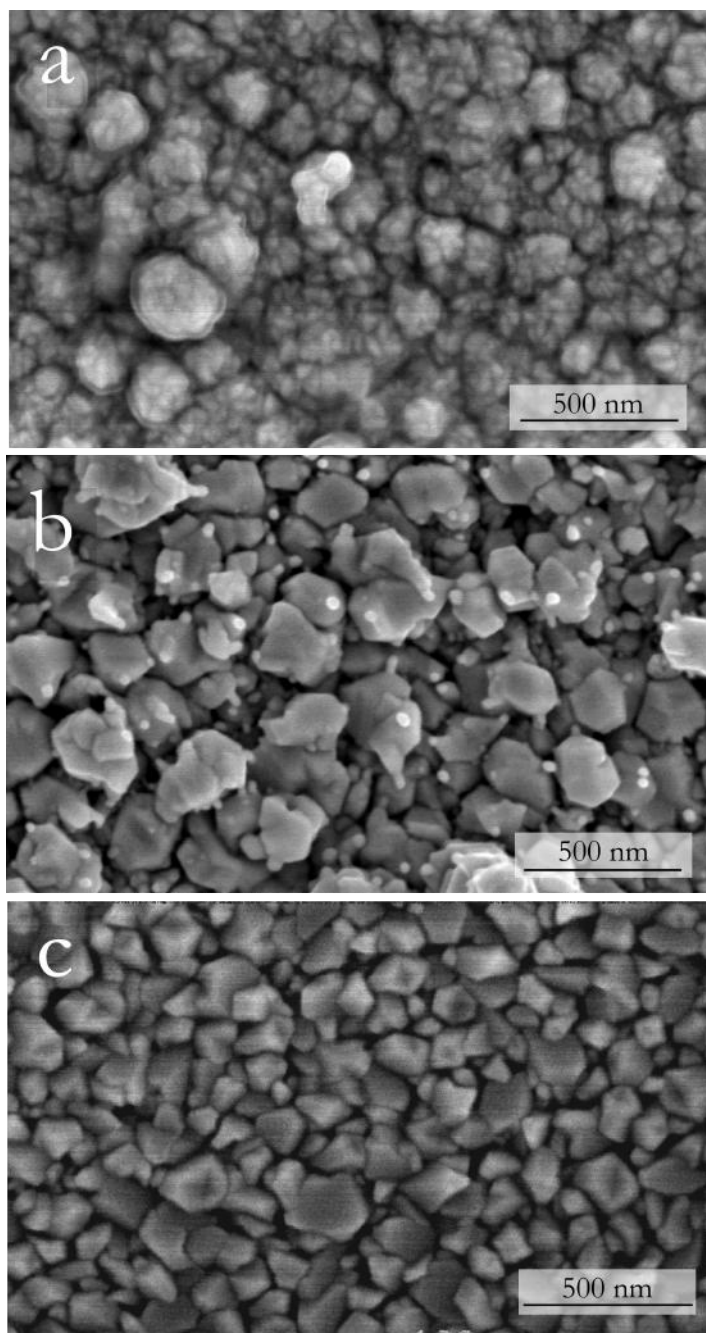


Figure 3.20: SEM images taken from different regions on the bottom plate of AuNP:SnO₂ composite deposited at 500 °C from a precursor solution of 5.6 at.% Au:Sn in 20 ml methanol at different distances from inlet of (a) 0 cm, (b) 4 cm and (c) 8 cm. EDX cannot determine if the white dot features in image (b) are nanoparticles because they are too small, however they are likely to be the uppermost features of the surface morphology.

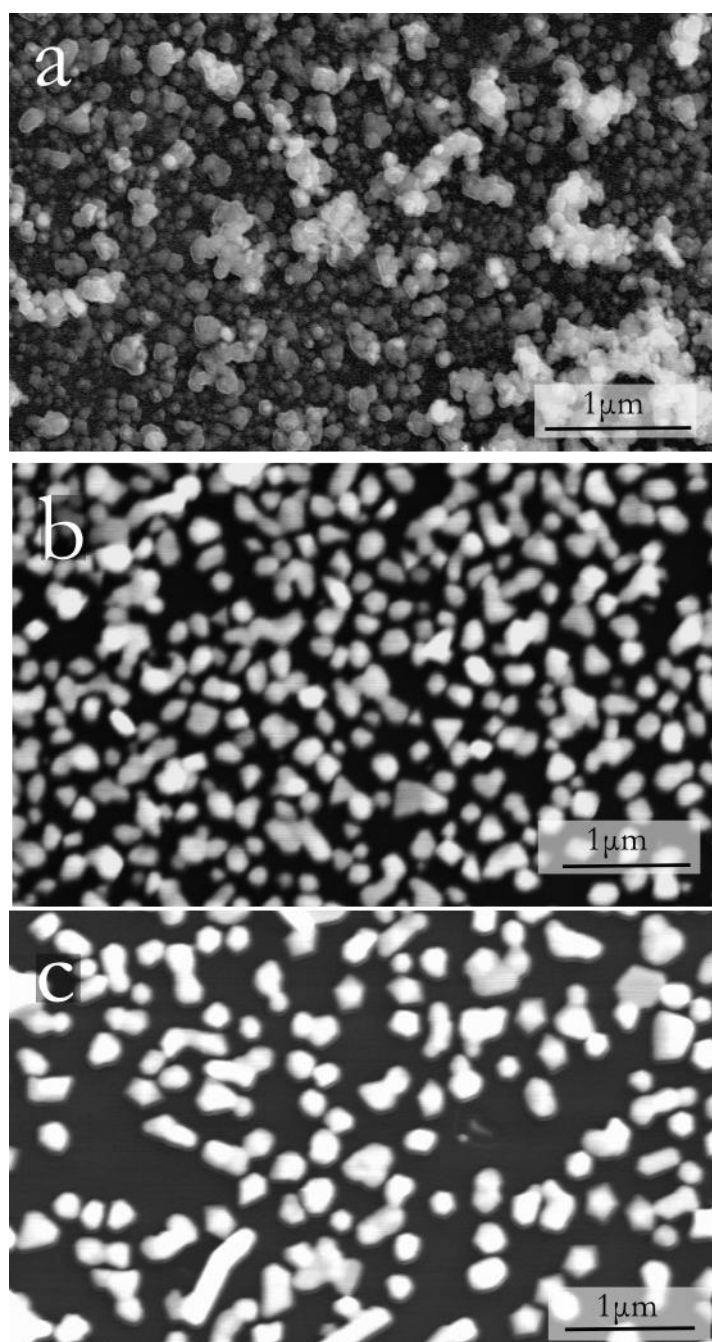


Figure 3.21: SEM images of gold nanoparticles deposited on the top plate from a precursor solution of $\text{HAuCl}_4 \cdot 3\text{H}_2\text{O}$ and BuSnCl_3 with an atomic ratio of 0.06 in 20 ml methanol at (a) 500 °C, (b) 450 °C, and (c) 400 °C.

3.6.4 Optical and electronic properties

UV/visible spectroscopy showed SPR absorption peaks in all the films but not all areas on the bottom and top plates. There were areas where the interference patterns were strong and so the SPR peaks could not be determined. From the observable SPR bands, the maxima ranged from 510 to 602 nm where the longer end of the range is red-shifted when compared with thin films of only AuNPs (Figures 3.14 & 3.10) either due to larger NPs size, a wider size range or due to the refractive index of the surrounding SnO₂. Previous observations of SPR absorbances measured from core AuNPs have been found to shift during the composite formation with a SnO₂.¹⁹² The reported AuNPs had an SPR absorption maxima at 522 nm, which increased to 545 nm after coating with SnO₂, then finally increased again to 554 nm after being spin coated into a thin film. These shifts in SPR are due to the refractive index of SnO₂ and also the final interparticle distance found in the thin film since the actual size of the AuNPs remained the same.¹⁹²

All conductance measurements were made on a 2-pt probe ammeter. The resistance of the films were on average in the 1 k Ω /□ range which is not optimum for conducting purposes and was less than depositions of just SnO₂.^{3.3}. However, the Drude-like reflectance in the far IR that is normally indicative of the presence of charge carriers seems to be unperturbed (Figure 3.22) leading us to think that the position of gold nanoparticles embedded within the SnO₂ matrix disrupted the conduction mechanism but retained the reflective character of the SnO₂. It is possible that the metallic gold deposits also contributed to this reflectance feature. Smaller areas of darker regions were reported to have much lower resistances around 2–3 Ω /□, probably due to high concentration of gold nanoparticles in the film reaching the percolation limit for metal conductivity. If it were needed for specific electronic applications, the electrical

conductance of SnO₂ could be increased introducing more oxygen vacancies and *n*-type doping.⁵

Bottom plate

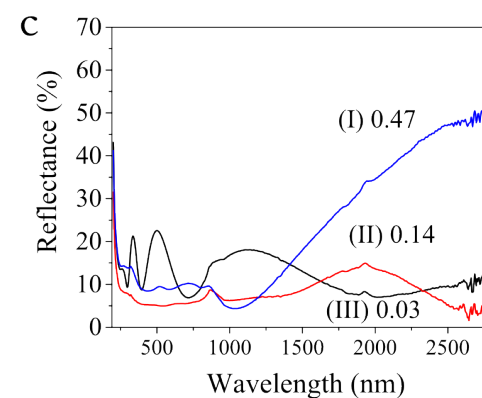
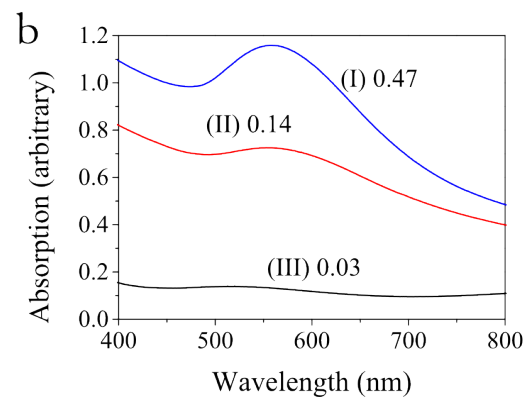
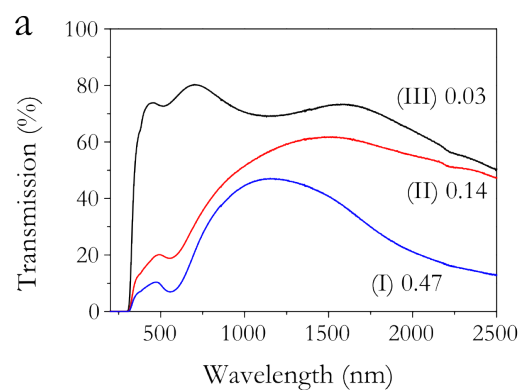
The transmittance percentages and the corresponding SPR band absorptions of films deposited on the bottom plates at 500 °C from an 5.6 at.% Au:Sn in the precursor solution at various points are shown in Figure 3.22. In general a higher Au:Sn ratio results in a lower transmittance and more prominent SPR absorbance. The width of the SPR band increases with Au:Sn ratio indicating a widening dispersion of the nanoparticles.²⁰⁹ Films with a lower Au:Sn content had lower SPR absorbance intensity and narrower SPR band, therefore lower dispersity of nanoparticles. The intensity of SPR absorbance can be used to indicate the relative amounts of gold nanoparticles. If there were less Au in the SnO₂ matrix the nanoparticles are less likely to agglomerate into larger nanoparticles and will also be more stabilised in the SnO₂ matrix. The SPR position changes according to the size of the nanoparticles, concentration and dielectric constant of the surrounding medium. However, due to the fact that the Au nanoparticles are embedded in the SnO₂ within the metal oxide matrix, the sizes and concentration of the nanoparticles could not be investigated and correlated with the SPR position.

Top plate

As EDX shows no Sn deposited and an Au atomic percentage of 100% for the film deposited on the top plate at 500 °C, the transmittance intensity or absorbance amount, was taken as a qualitative indicator of the amount of gold deposited. All areas displayed a clear SPR absorption indicating nanoparticulate rather than island or thin film morphology. There is a higher intensity of SPR and concentration of Au near the inlet, as the precursor is deposited and

used up the intensity decreases when moving away from the inlet (Figure 3.22).

Bottom plate



Top plate

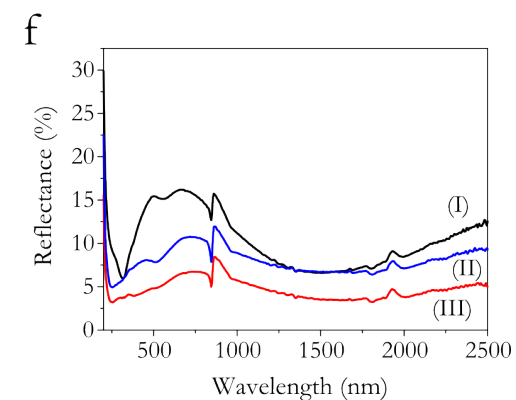
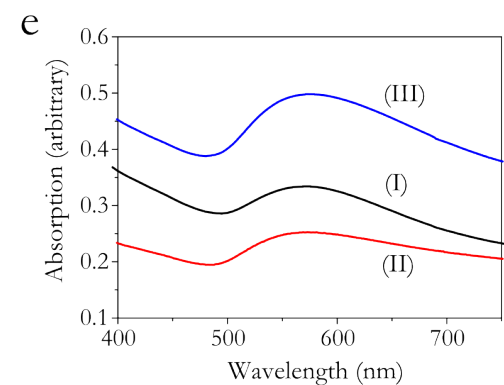
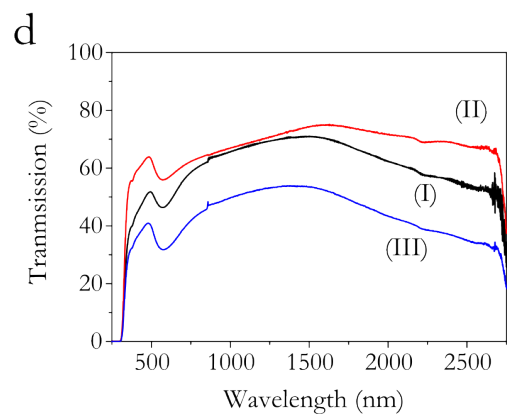


Figure 3.22: Optical properties from a deposition using a precursor solution of 5.6 at.% Au:Sn in 20 ml methanol at 500 °C. Transmittance (a), absorption (b) and reflectance (c) spectra correspond to bottom plate depositions. The observed ratios of deposited Au:Sn are labelled. The areas investigated as a function of distance from the inlet (I) 0 cm, (II) 4 cm and (III) 8 cm are labelled. (d), (e) and (f) correspond to transmittance, absorbance and reflectance top plate depositions with (I), (II) and (III) here referring to Au at.%.

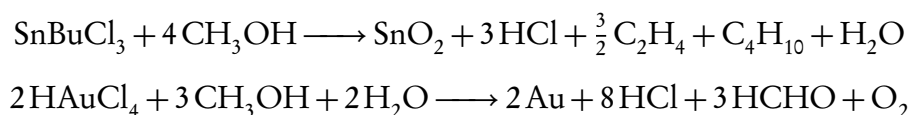
3.6.5 Reaction pathway

The formation of the gold nanoparticles in the reaction comes from the decomposition of auric acid in the gas phase during the CVD process. The tin dioxide host matrix deposited on the heated bottom plate substrate at all investigated temperatures but on the unheated top plate only during 500 °C depositions. Interestingly the gold nanoparticles were found embedded within the tin matrix, affording intense SPR generated colours, however the nanoparticles were predominantly within the bulk of the tin dioxide coating and could not be imaged by SEM at the surface.

The top plate regions that were investigated showed mostly gold nanoparticles. The fact that a significant amount of gold nanoparticles were observed on the top plate is a result of thermophoresis where the already formed nanoparticles in the gas phase find it difficult to diffuse through the diffusion layer at the heated surface and rebound, eventually settling on the cooler top plate.²⁰³ The observed top plate nanoparticles formed were of different sizes and shapes but showed triangular and hexagonal facets as well as spherical particles. Notably, the concentration of gold both within the tin dioxide film matrix on the heated substrate and on the top plate varied considerably with distance from the inlet to the reactor. This enabled the generation of a film with concentration gradients of Au:SnO₂, where the nanoparticle to host matrix ratios varied markedly down the film. This enabled us to explore the composite phase space rapidly and determine the best regions for colouration and reflective properties as well as for conductivity.

The methanol carrier solvent has a key effect on both reactions, in the formation of nanoparticles and host the metal oxide host. Methanol has been shown in a number of CVD reactions to promote the formation of elemental metals, especially for Cu²¹⁴, Ag²¹⁵ and Au.³⁸ It is thought that methanol de-

composes in the reactor forming an *in situ* source of hydrogen which may aid the formation of the nanoparticles. Conversely the methanol also acts as the source of oxygen for the formation of the tin oxide matrix as the reaction was conducted under a nitrogen atmosphere. One possible set of equations for the processes are schematically illustrated below;



Both top and bottom plates were analysed since there was Au deposition on both and so the reactions that occurred can be properly evaluated and understood. We see an increase in dispersity of the top plate nanoparticles when starting with a low Au precursor concentration. This is in contrast to bottom plate nanoparticles where the dispersity decreases with increasing gold content due to stabilisation of SnO₂ and the decrease in mobility of Au particles. The presence of the SPR and the elemental detection of gold (EDX/XPS) suggests the presence of gold nanoparticles despite not being able to readily image them in SEM images. The relationship between the SPR width and the Au content promises an ability to tune the characteristics of the nanoparticles with deposition conditions.

3.6.6 Summary

Composite films of AuNP:SnO₂ were grown from a simple one-pot solution using AACVD. Two types of films were generated, top plate films consisting of mostly gold, and bottom plate films which consisted of AuNP:SnO₂. The Au was incorporated into the film at different ratios and it was found that thin films of the composite that have between 3-15 at.% Au:Sn, optimum properties were found in terms of blue colouration, reasonable optical transparency and also reflectivity in the IR. The intensity and tint of the colouration depends on

the nanoparticles as well as the dielectric constant of the metal oxide matrix, which will be further explored in Chapter 4. In order to improve the TCO properties of the film, the SnO₂ can be F doped. It would also be ideal if the top plate nanoparticles could be utilised as they could be considered wasted in this process.

3.7 Layering to make conductive AuNP and SnO₂ composites

In this section thin films of AuNPs and FTO are layered and combined to create double layered composite thin films of either FTO on AuNPs (FTO/AuNP) or AuNPs on FTO (AuNP/FTO) as illustrated in Figure 3.23. By depositing one film at a time, optimum deposition conditions can first be determined before combining the materials, enabling us to tailor the product for specific desirable characteristics and avoid interactions between the Au and Sn precursor in the bubbler or in the reactor. Layering a composite also allows us the option of exposing either the AuNPs or the metal oxide to the outside surface. The deposition conditions of each layer is identical to the high quality single layer thin films described in Section 3.4 for FTO and Section 3.5.3 for AuNPs, therefore the composite films had good TCO properties (low sheet resistance, transparency) and a reproducible gold nanoparticle SPR.

In a CVD process metal oxides have no problem adhering to a glass substrate, on the other hand AuNPs are typically not adherent to glass³⁸ unless complicated methods such as pretreatment of the glass²¹⁶ or silanisation²¹⁷ are employed. Using the layering method, the AuNPs can be robustly adhered by overlaying FTO above it and also when overlaid on FTO, suggesting the presence of strong interactions between the gold nanoparticles and semiconducting

3. Functional Composites of Gold Nanoparticles and Tin Dioxide

FTO. All the composite films were adherent to the glass substrate, passing the Scotch[®] tape test, with no visible change after months of storage and only scratching off when using a steel scalpel with force.

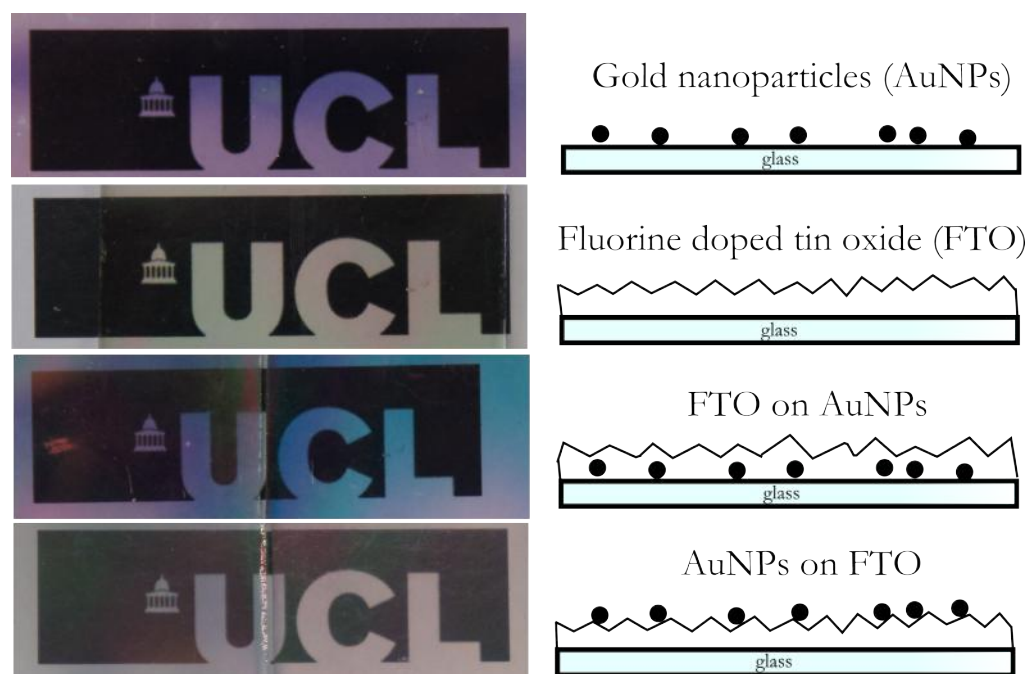


Figure 3.23: Photographs of films showing the colour and transparency. (a) AuNPs deposited from auric acid, (b) FTO deposited from butyltin trichloride and ammonium fluoride, (c) FTO deposited as an overlayer above AuNPs and (d) AuNPs overlaid above FTO.

3.7.1 FTO on Au

For layered films of FTO on AuNPs (FTO/AuNP) a range of AuNPs were deposited first, using the same precursor concentrations as in Table 3.2, with a subsequent FTO layer made using a 30 at.% F:Sn precursor solution of NH_4F to BuSnCl_3 in methanol.

Film appearance and morphology

The resulting FTO/Au films were blue and transparent with the FTO acting as a sealant, adhering the AuNPs to the glass (Figure 3.23). Most of the

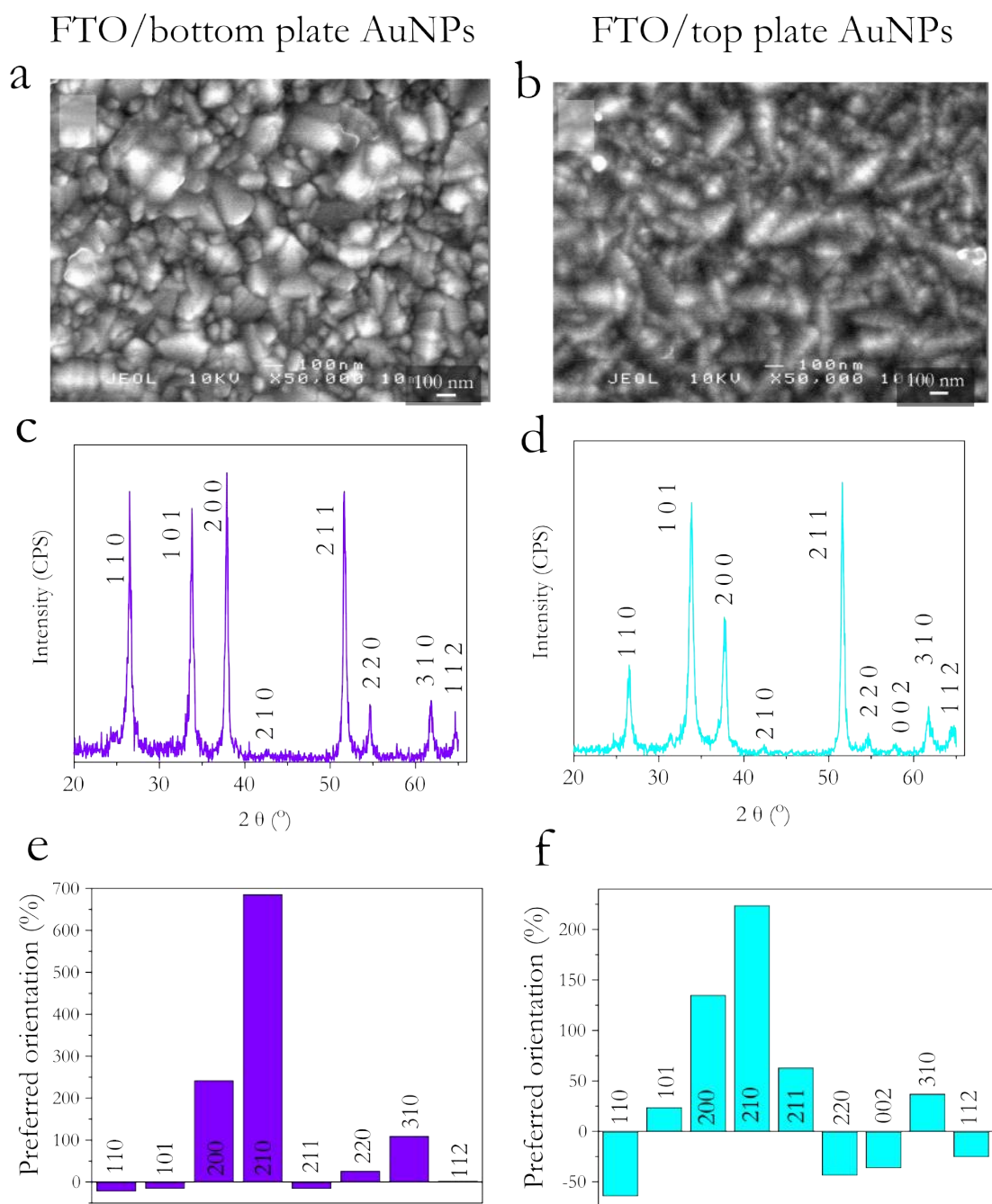


Figure 3.24: Comparing the properties of composite FTO (from a precursor solution of 30 at.% F:Sn) depositions on AuNP substrates from top and bottom plate positions. Different morphologies were observed from the SEM images of FTO on bottom plate (a) and top plate (b) and inserted are SEMs of the AuNP substrate.

FTO/AuNP films displayed SnO₂ reflection patterns in the XRD with preferred orientation in the (210) plane (Figure 3.24) the same as FTO deposited onto glass (Section 3.4). An exception was found for the layered films where FTO was deposited on a highly concentrated layer of AuNPs, from the highest auric acid precursor concentration investigated (1 mM), whereby the preferred orientation was solely (200). The change in preferred orientation is reflected in the broader particle morphology observed from SEM images (Figure 3.24) which could be due to a disturbance in the growth of the film from the shape of the underlying AuNPs.

Optical and electronic properties

The colour of the films change from pink/purple with just AuNPs to blue after overlaying with FTO (Figure 3.23), indicating that the absorption had moved towards the red end of the spectrum. This correlates with the location of the AuNPs' SPR maximum (Figure 3.25), which generally shifts to longer wavelengths after FTO deposition as a consequence of the change in surrounding dielectric constant by having the FTO in-fill the AuNP structure. The composite's transmittance and reflectance plots are simply a combination of the two individual films.

The measured electronic properties (Table 3.5) of the FTO/AuNPs were retained, with the reflection in the far IR due to the onset of the plasmon band not affected by a AuNP substrate (Figure 3.25) when compared to the reflection spectrum of the FTO (Figure 3.7) thin film. This could mean that no electron transfer is occurring in between the layers. It should be noted that the blue colouration from the SPR combined with the reflection in the far IR is an ideal one for window applications.

Table 3.5: Electronic properties of FTO on AuNPs layered thin film. Precursor solutions in methanol (20 ml) were composed of 30 at.% F:Sn for FTO and 2×10^{-2} mmol HAuCl_4 (1 mM) for AuNPs.

Substrate for FTO deposition	ρ , resistivity ($\times 10^{-4} \Omega \text{ cm}$)	R_{SH} , sheet resistance (Ω/\square)	μ , mobility ($\text{cm}^2(\text{Vs})^{-1}$)	N, carrier concentration (cm^{-3})
Glass	5	10	25.3	4.93×10^{20}
AuNPs (top plate)	-	-	28.44	4.26×10^{20}
AuNPs (bottom plate)	4.86	7.84	25.73	4.99×10^{20}

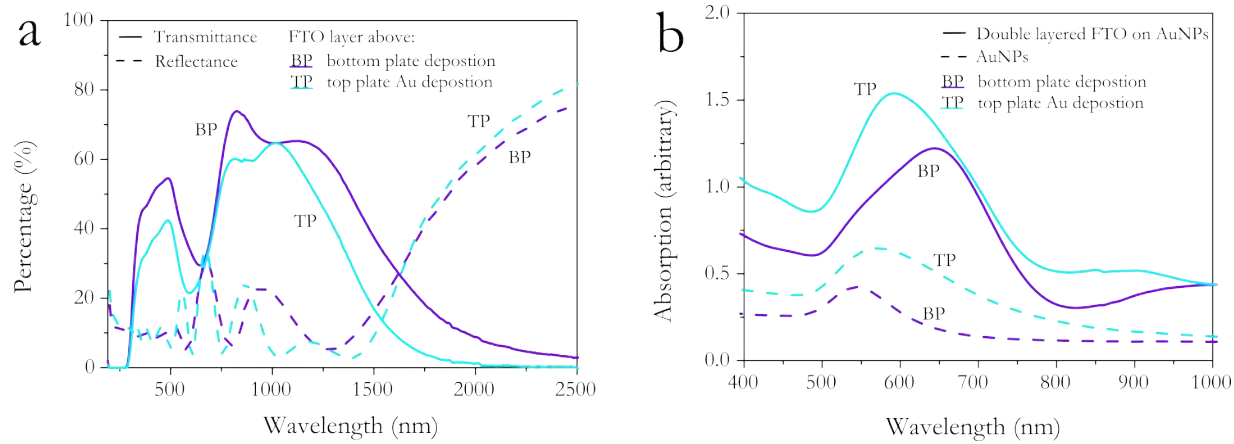


Figure 3.25: The (a) transmittance and reflectance spectra for FTO deposited on the bottom and top plate of a gold nanoparticle deposition. SPR absorptions were also observed as shown in (b).

3.7.2 Au on FTO

For AuNPs on FTO layered materials, the FTO was deposited first with a precursor concentration of 30 at.% F:Sn in methanol. The FTO films were then used as the top and bottom plate in the same auric acid deposition set up as described in the first section using precursor concentrations in Table 3.2.

Film appearance and morphology

The adherence of AuNPs was stronger to the FTO thin film compared to the glass substrate, where it withstood the Scotch[®] tape test rather than being rubbed off very easily upon slight touching. This suggests a strong intermolecular interaction between the AuNPs and the FTO, perhaps due to the fact that FTO is semiconducting whereas the silica barrier on the glass substrate is insulating. The preferred orientation of the FTO was found to be in the SnO₂ (200) and (210) plane (Figure 3.28) as expected from the FTO in Section 3.4. A small peak at around $2\theta = 45^\circ$ is attributed to the cubic gold (200) plane which was not observed in the XRD pattern of the FTO/AuNPs layered film since the XRD pattern was measured with a low angle of 0.5° and so is relatively surface sensitive.

The deposition of AuNPs nanoparticles on the FTO varied from a very dense layer of spherical NPs to a more decorative type when depositing at lower auric acid concentration shown in (Figure 3.26 and 3.27). However, the sizes of the nanoparticles do not seem to vary much and ranged from 30 to 70 nm. AuNPs can be observed in the SEM image even where the SPR was not easily detectable indicating depositing them onto FTO is less efficient than onto glass. In general the electronic properties of the AuNPs on FTO thin films were the same as FTO on glass with the resistivities around $5 \times 10^{-4} \Omega \text{ cm}$.

Bottom plate AuNPs/FTO

Top plate AuNPs/FTO

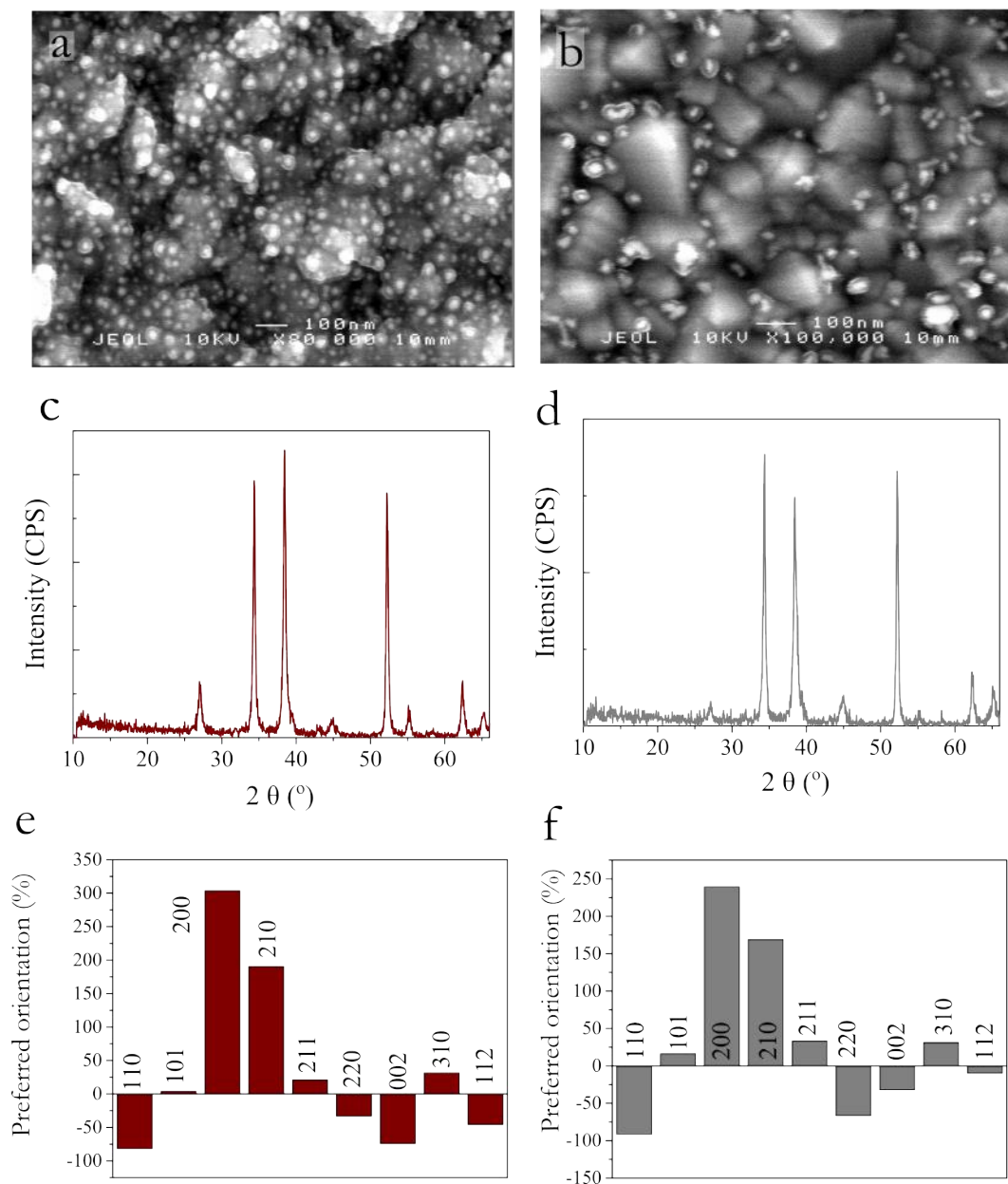


Figure 3.26: Comparing the properties of composite films from AuNP top and bottom plate depositions onto a substrate of FTO (30 at.% precursor ratio of F:Sn). Different amounts and sizes of nanoparticles were observed from the SEM (a & b), slightly different XRD patterns (c & d) and preferred orientation (e & f).

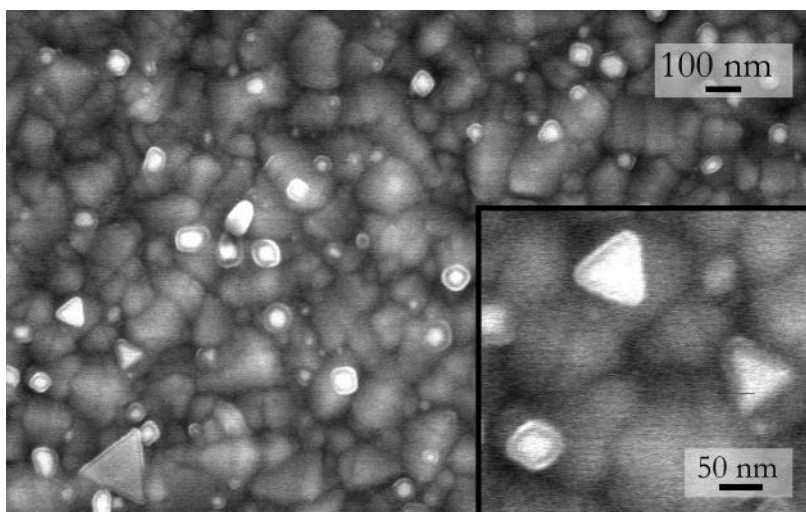


Figure 3.27: SEM image of AuNPs (brighter parts of image) with decorative shapes on FTO.

Optical and electronic properties

Only the films deposited with a high auric acid concentration (1 mM) have small but detectable SPR absorption maxima at 528 and 562 nm for bottom and top plate films respectively (arrows Figure 3.28). Despite the lack of visible SPR, all the films still have a light pink purple colouration indicating that there was indeed a layer of AuNPs (Figure 3.23). The position of the visible SPR maxima follows the trend of previous films whereby the position of the bottom plate AuNPs maximum is at a shorter wavelength compared to the top plate AuNP film, again indicating that top plate depositions result in larger AuNPs. When comparing the detectable SPR maxima of AuNP/FTO and AuNP/glass, a slight shift to lower wavelengths was observed. This is a combination of the dielectric character of the FTO as well as different substrate conditions for AuNP formation and deposition.

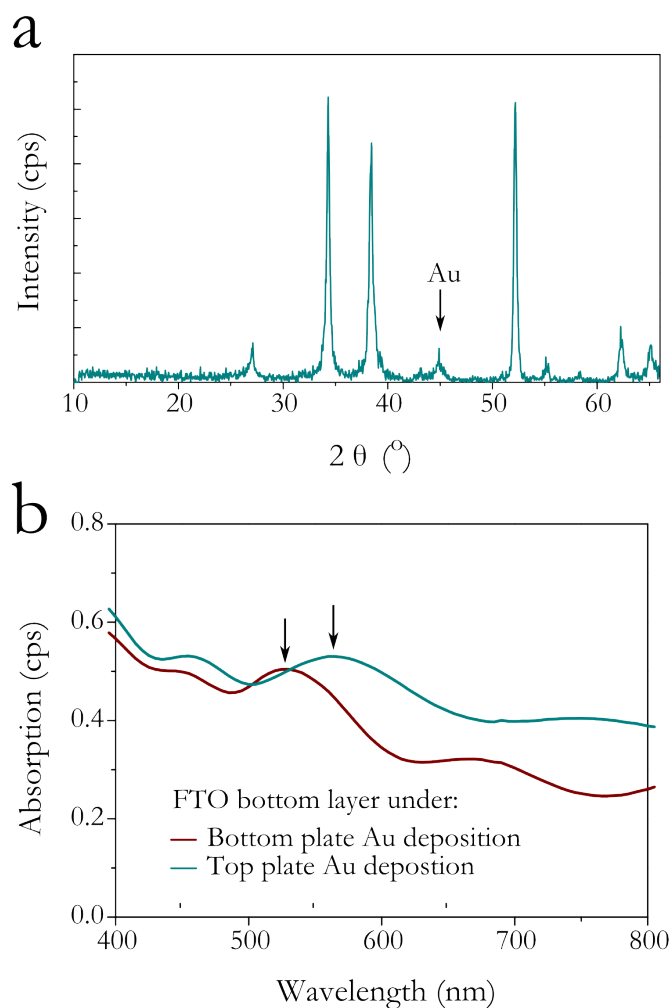


Figure 3.28: XRD and optical spectra of AuNPs deposited onto fluorine doped tin oxide thin film. (a) XRD pattern is standard for all the FTO on AuNPs thin film. (b) The SPR absorption (arrows) of FTO overlaid above top and bottom plate gold nanoparticles.

Summary

The SPR properties of AuNPs and TCO properties from FTO have been successfully combined into composite materials and characterised. The composite gold nanoparticle and FTO films were deposited using aerosol-assisted chemical vapour deposition in a layered structure. The highly transparent and conducting character of the FTO was not altered even when depositing above a layer of AuNPs with all the films achieving excellent sheet resistances of between $8\text{-}10 \Omega/\square$. The layered thin film took on the optical character of both

layers, combining the SPR absorption (500-700 nm), blue/pink colouration and reflection (onset at 1500 nm) in the IR due to the high charge carrier concentration. The refractive index of the FTO film is higher than air at around 2,^{130,205} and this shifts the SPR absorption towards longer wavelengths.¹⁴⁹

Considering the *in situ* AACVD method for making AuNPs without surfactants, the deposition still managed to produce AuNPs homogeneously on the surface at approximately the same sizes as each other which were dependent on precursor concentration given identical deposition temperature. This method is to our knowledge the first report of making layered films of TCO with enhanced colouration properties, and can be further studied in terms of a tunable system with easier deposition of composite AuNP:metal oxide system without the need for an extra *ex situ* nanoparticle synthesis step.

3.8 Conclusion

There have already been various reports of AuNP composites with other metal oxides TiO₂, WO₃, MoO₃, and VO₂ synthesised from AP (atmospheric pressure) and AACVD.^{12,38,188,203} This work in this chapter expands on the previous reports with the synthesis of composite functional thin films with very good industrial standard TCO properties by using FTO. The majority of previously reported AuNP and SnO₂ based composites have the AuNPs pre-synthesised using some version of the Turkevich method before being loaded onto a metal oxide.^{183,192,195,196} The AACVD has shown to be a flexible choice for metal oxide noble nanoparticle composite formation as the AuNPs can be formed directly from auric acid using heat and decomposition reactions rather than having to be preformed or thermally activated in a two-step reaction.^{112,192,218}

AuNPs and SnO₂ were first deposited separately using AACVD reactions. F doping using the NH₄F precursor effectively improved the properties of the

SnO₂ thin film, producing a high quality film combining the typical low resistance and high visible transparency as expected from previous reports.⁷⁹ A one-pot precursor solution of auric acid and MBTC was shown to be able through CVD to deposit composite films although the electronic properties were not up to TCO standards. However, depositing AuNPs from auric acid by themselves produced a more controlled and efficient reaction not seen with previous CVD methods of Au synthesis,^{38,203} with some predictability about NP size and dispersion. Therefore, the AuNPs and FTO films were instead deposited layer by layer, allowing the choice of either film being exposed to the environment. This method can be expanded to other metal oxide nanoparticulate composite systems and it can be easily seen that this will be a useful way of tailoring the deposition procedure and composite properties for various specific application.

Table 3.6: A comparison of the preferentially orientated planes of SnO₂ and FTO deposited using AACVD with MBTC and NH₄F.

Material	Conditions (temperature, carrier gas)	Preferred orientations
SnO ₂	400-500 °C, N ₂	(210), (111), (110)
FTO	450 °C, air	(200), (210)
AuNP/FTO	450 °C, air	(200), (210)
FTO/AuNP	450 °C, air	(210), (200)

The preferred orientation growth for the SnO₂ thin films were similar to other CVD and spray deposition methods, with an increasing and preferential growth in the (200) plane correlating with F-doping or increasing conductivity.^{78,116} As Table 3.6 shows, when the FTO is deposited onto AuNPs instead of the silica coated barrier glass, there is an increase in the (210) and a decrease in the (200) plane, although these both are still the preferred growth planes. This is probably due to the rough structure of the substrate AuNP film, as the sizes of the NPs were quite substantial at 20-60 nm diameter when compared

to a flat substrate.

Since the refractive index of the metal oxide seems to be an important factor in the final SPR of the composites, the next chapter will report on the optical properties of various composites comprised of AuNPs and multiple other metal oxides. The relationship between the refractive index of the various metal oxides, measured with ellipsometry and shifts in SPR absorbances are discussed.

Chapter 4

Effect of Metal Oxide Character on the SPR in Composites with AuNPs

4.1 Introduction

It is well known that the peak positions and character of the SPR absorption alters with size, shape and the surrounding media of the noble metal nanoparticles.^{149,219,220} Results from Chapter 3 showed a variety of AuNP depositions, with different nanoparticle sizes and within an SnO₂ matrix using different layering structures. We found that the colours and SPR absorbances were different for a range of AuNP sizes, and for the different structures of the composite; FTO overlaid onto AuNPs or AuNPs overlaid onto FTO. In order to be able to analyse the effect of the refractive index of the metal oxide on the SPR, we needed to be able to compare with other metal oxide composites. The AACVD method is well established for depositing various metal oxides²²¹ and has been shown in this thesis able to deposit AuNP thin films, was used to prepare various composites of AuNPs and different metal oxides. This can give

us some insight into the way the metal oxides deposit on the nanoparticles and give us an idea of how to tune the SPR. We chose to structure the layers so that the metal oxide is overlaid above the AuNPs. This ensures that the AuNPs deposit in the same environment on the same substrate, resulting in a similar SPR absorbances and nanoparticle character. The optical properties of the metal oxide/AuNP composites were investigated and compared. There have been studies on the effect of the surrounding refractive index on the plasmon character of nanoparticles, however it has to be noted that any effect seen is very dependent on the specific system being investigated, not only on the size and shape of the nanoparticles, but also the surfactant being used or the acidity of the solution. So in order to discuss about the effect of the refractive index of the surrounding media on the SPR of AuNPs, it is necessary to investigate it in terms of using the system of deposition used in this thesis.

Using an optical darkfield microscope, the SPRs of individual AgNPs can be measured allowing investigation into their dependence on different local refractive index environments. The local refractive index of a system with 70 nm Ag nanoparticles was varied from 1.44 to 1.56 using index oils and a red shifting of 1.16 nm per 0.01 index change was found.²²² Since the shift depends on the interface between the NP and the index oil, different sizes of NP will be affected to a different degree, and indeed it was found for AgNPs that different sizes had different sensitivities to the solvent refractive index.²²³ Furthermore, the same authors also reported different shapes having varying sensitivities to the change in refractive index, with ellipsoidal particles being less sensitive than angular truncated tetrahedrals.

Within a solid it is harder to linearly change the refractive index easily but, by varying the ratios of SiO₂ to TiO₂, in SiO₂-TiO₂ mixed metal composites different refractive index environments can be produced. Using sol-gel, AuNPs were embedded within these films producing composites film colours

that ranged from pink to blue, where the SPR was red-shifted with increasing refractive index.²²⁴ The increased wavelength of the SPR maxima compared relatively well to calculations performed using Mie theory, taking an average spherical particle diameter of 10 nm which was confirmed by TEM. Within a AuNP-metal oxide composite, as the metal oxide changes from being amorphous to crystalline, the refractive index can also be affected and so any observed SPR.²²⁵

4.2 Objectives

In this chapter, the refractive index of the environment surrounding the AuNPs is changed through the use of different metal oxides. All the materials discussed here were deposited using the AACVD method as described in Section 2.1. The metal oxides (TiO_2 , ZnO , Al_2O_3 , Ga_2O_3 and MgO) were overlaid above AuNP films to form the composite with a layered structure. The refractive index was measured with ellipsometry so the specific character of the metal oxide character, such as phase and growth morphology, which is affected by deposition method can be discounted. From this it would be ideal if there was a relationship or correlation found between the refractive index and the SPR absorption so the optical absorption of thin films deposited in the future can be tuned.

4.3 Experimental details

4.3.1 AACVD of composite films

All depositions were performed in an AACVD reactor as described in Chapter 2. Gold nanoparticles were deposited first using a 0.02 mmol auric acid solution (HAuCl_4 in dilute HCl solution dissolved in 20 ml methanol) at 450 °C.

4. Effect of Metal Oxide Character on the SPR in Composites with AuNPs

The reactor was left heating at the deposition temperature for a further hour after the precursor solution was exhausted before being turned off and finally left to cool to room temperature. The cooled gold nanoparticle plates were removed from the reactor and the bottom plate returned to be used as a substrate for further metal oxide deposition thus forming a composite thin film of gold nanoparticles and said metal oxide (Figure 4.1).

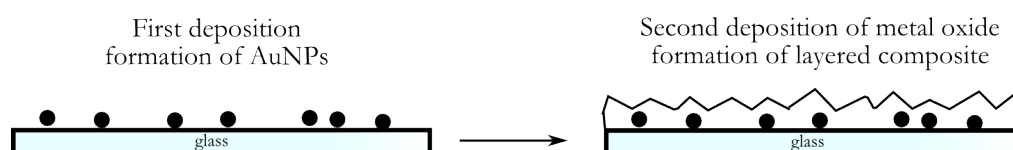


Figure 4.1: Schematic showing the 2-step deposition process of layered AuNP and metal oxide composite formation.

Precursor solutions were made up from monobutyltin trichloride, gallium acetylacetonate, titanium ethoxide, aluminium acetylacetonate, magnesium acetate and zinc acetate, left to stir till fully dissolved before using in the reaction. All AACVD reactions of the metal oxides took roughly 30-40 minutes for the precursor solution to be completely depleted. Composites were formed from the following metal oxides: SnO_2 , Ga_2O_3 , TiO_2 , ZnO , MgO and Al_2O_3 . The deposition details for each metal oxide are displayed in Table 4.1.

Table 4.1: Deposition details for the various metal oxides. All precursor solutions were made with 20 ml methanol, with the exception of titanium ethoxide which was dissolved in 15 ml toluene. All depositions occurred at 450 °C.

Material	Precursor	Concentration (mM)	Carrier gas	Flow rate (Lmin ⁻¹)
SnO ₂	monobutyl tintrichloride	24	air	0.5
Ga ₂ O ₃	gallium acetylacetonate	89	air	1.5
TiO ₂	titanium ethoxide	292	nitrogen	0.5
ZnO	zinc acetate	139	nitrogen	1
Al ₂ O ₃	aluminium acetylacetonate	77	air	2
MgO	magnesium acetate	82	air	1

4.4 Results

4.4.1 AuNP deposition

Using the auric acid precursor in a solution with dilute hydrochloric acid, instead of hydrated hydrogen tetrachloroaurate crystals that was used in Chapter 3, resulted in a different AACVD reaction as there is extra acidity present in the precursor solution. The gold first deposits as a rough film with a broad SPR absorption and was observed to have a blue colouration (seen from 30 minute absorption spectrum in Figure 4.2), which is attributed to a rough surface with nanofeatures similar to previous reports.³⁸ After the blue film is returned to the reactor and heated up again to the deposition temperature of 450 °C, the broad feature gradually narrows into a clear peak where the majority of the absorption shifts towards the blue, correlating with a change in colour to purple and pink (see 60 minute absorption spectrum in Figure 4.2). After reheating the pink/purple AuNP film to 450 °C again for another hour, the colour and pattern remained the same, therefore leading to the conclusion that there

4. Effect of Metal Oxide Character on the SPR in Composites with AuNPs

would be no further major change in SPR or NP size from heating once the NP shapes have been stabilised. Throughout heating the pattern of deposition on the glass remained the same with no net migration of Au on the substrate and just a change in morphology. This progression of SPR features are shown in Figure 4.2 labelled with the duration of additional heating after the films were deposited. At 60 minutes the rough surface had been fully developed into nanoparticles, the narrowing of the absorption was not accompanied by a shift in the position of the SPR absorption maximum indicating that there might be an ideal AuNP shape and size that was dependent on the initial Au concentration and temperature. At 450 °C it seems that the thermodynamically favoured morphology of Au is made up of disconnected nanoparticles rather than a thin film. Further heating will probably result in a narrowing of the SPR but without change in SPR maximum.

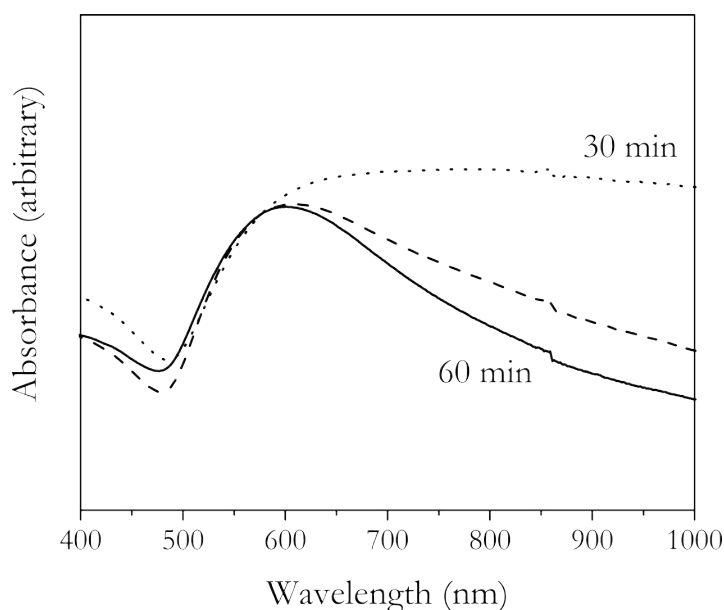


Figure 4.2: The absorbances of AuNP depositions after different deposition durations (30-60 min) from a precursor solution of HAuCl_4 (solution with dilute HCl) dissolved in methanol. As the additional heating duration is extended, the AuNP film transforms from a rough surface to nanoparticles resulting in a narrowing of the SPR absorption. The general flat absorbance between 600-1000nm develops into an SPR peak and maximum as the deposition time increases.

The AuNP films used in this chapter have all been heated for a further 60 minutes in order to get fully nanoparticulate films. A layer of AuNPs in a range of sizes of mostly between 10 to 40 nm can be observed from the SEM and TEM images in Figure 4.3. There were also some much smaller NPs of sizes 5 nm which could be absorbed into the larger nanoparticles, perhaps towards the optimum size, during the second step of metal oxide deposition during composite formation (Figure 4.1).

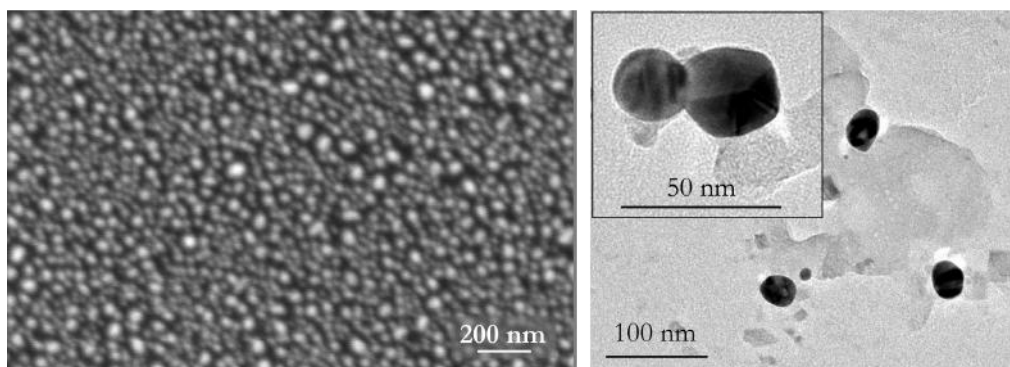


Figure 4.3: SEM and TEM images showing the AuNPs deposited using a precursor solution of 0.02 mmol HAuCl_4 at 450 °C.

4.4.2 Metal oxide deposition

Phase and morphology

Tin oxide, anatase titanium oxide, zinc oxide and magnesium oxide displayed crystalline peaks in the XRD pattern (Figure 4.4). Gallium and aluminium oxide were both amorphous at the investigated deposition temperature of 450 °C, as they only form polycrystalline thin films at temperatures of 700 °C and above.^{226,227} Crystallinity was not important for the reasons investigated here so the films were chosen not to be annealed or deposited at a higher temperature, since heating it any further will increase the temperature to above that which the gold nanoparticles were deposited at could possibly further change their morphology. Being amorphous might affect the morphology and defects

in the film and therefore change the refractive index of the material when compared to reference values of crystalline films in the literature, however this was negated since the refractive index was directly calculated from ellipsometric data taken on the actual films (discussed in Section 4.4.3).

From SEM images in Figure 4.5 magnesium oxide and gallium oxide were observed to have relatively flat surface morphologies. Despite depositing as an amorphous thin film at 450 °C, the aluminium oxide thin film still seems to have a systematic growth pattern since its surface possesses distinctive spherical shapes similar to previously reported amorphous alumina films.²²⁸ As expected from Chapter 3, the surface of tin oxide was faceted, covered with a square based pyramidal structure and resulting in a rough surface. The surface of titanium oxide had semi-spherical shapes which were relatively smooth and featureless. Zinc oxide's surface had the presence of clumpy clusters leading to the roughest film when observing the side-on SEM images (Figure 4.6). The side-on SEMs and Filmetrics measurements were used to determine the film thicknesses.

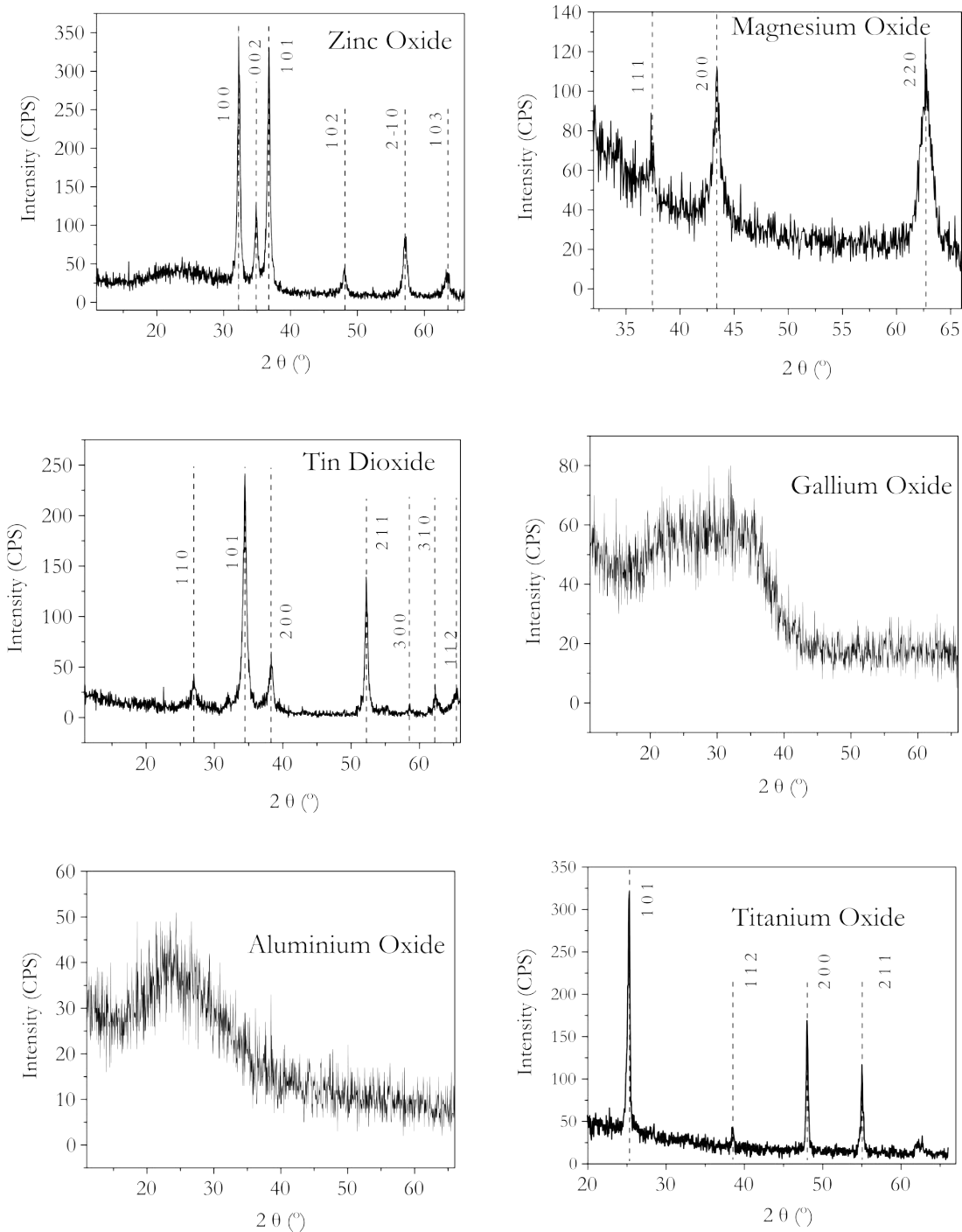


Figure 4.4: X-ray diffraction patterns of various metal oxides deposited using AACVD.

4. Effect of Metal Oxide Character on the SPR in Composites with AuNPs

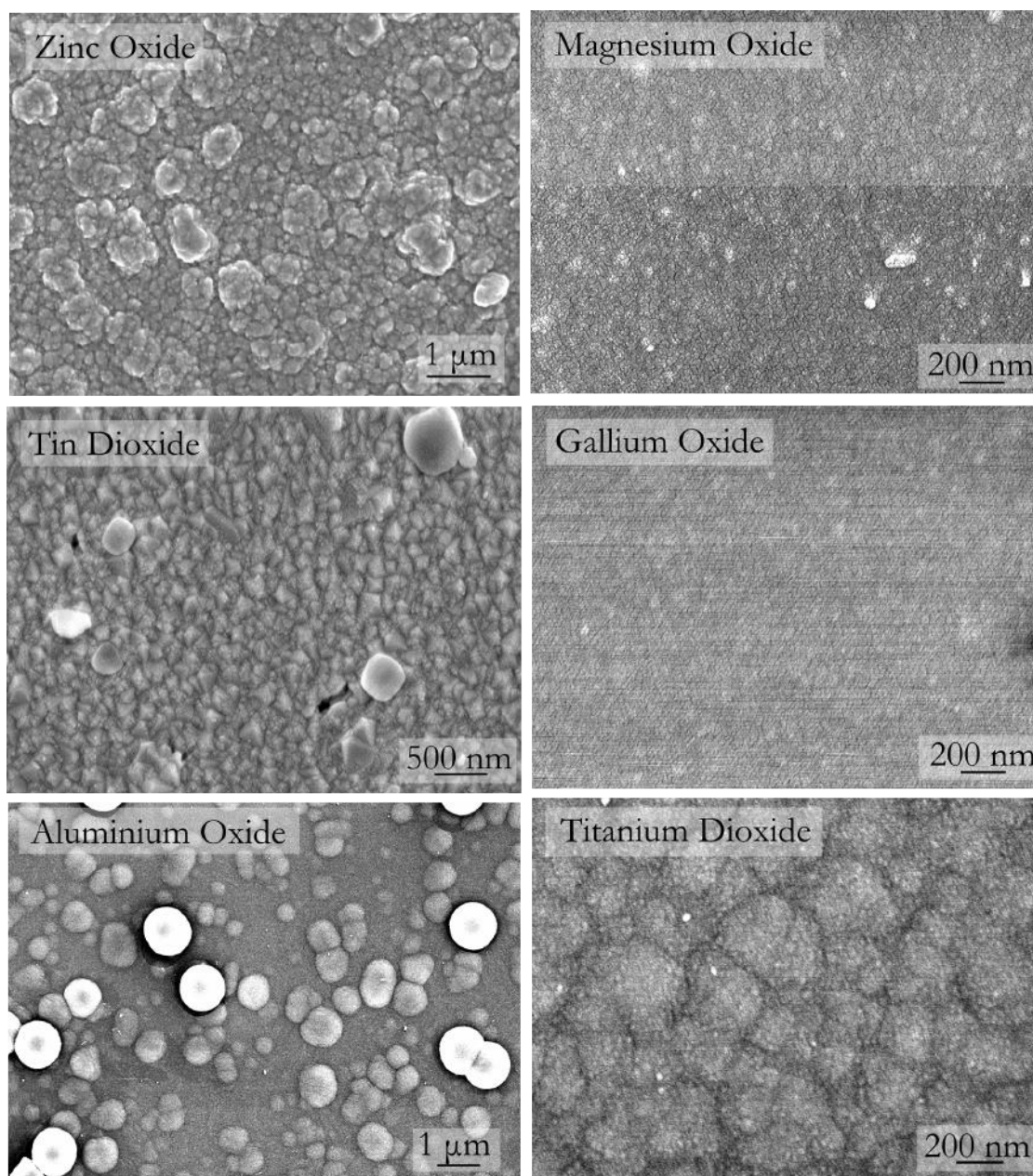


Figure 4.5: SEM images of various metal oxides deposited using AACVD.

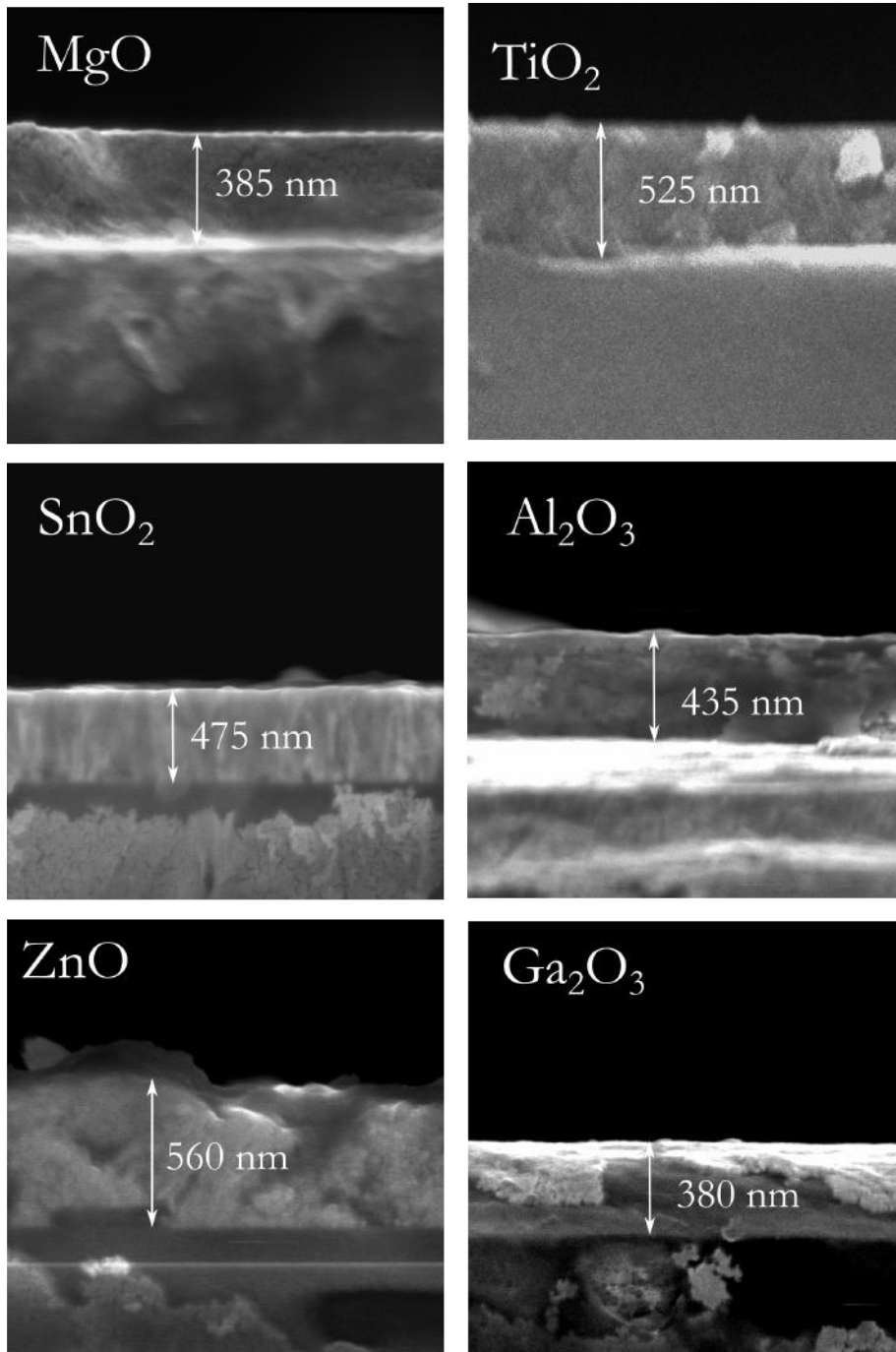


Figure 4.6: Side-on SEM images of the various metal oxides deposited using AACVD.

Optical properties of the metal oxides

All the films have a high transparency in the visible region with over 70% transmittance between 300-800 nm, apart from TiO_2 which suffered from slight brown tinges due to carbon contamination, though it still had a relatively high transparency of around 60% (Figure 4.7). Since all the films have thicknesses in the visible range, interference patterns could be seen in all the transmittance and reflectance data. Zinc oxide, tin oxide and titanium oxide thin films show a slight increase in reflectance in the far infra-red due to the increase in electron carriers, although it was not enough for the films to be appreciably conductive. Even though the films investigated here do not possess good conductor properties, they have the potential to be doped to make them suitable for TCOs or other applications, however this is not within the scope of this investigation.⁵⁴

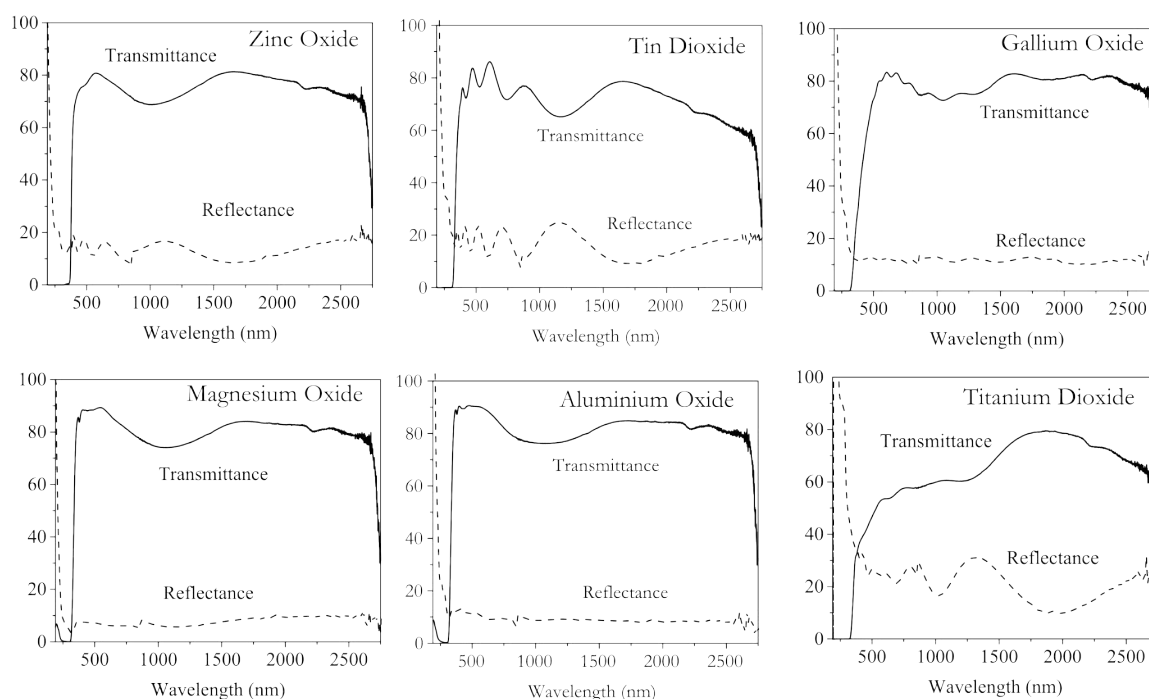


Figure 4.7: Transmittance and reflectance spectra of various metal oxides deposited using AACVD.

4.4.3 Ellipsometry and the determination of refractive index

Spectroscopic ellipsometry measures the polarization that an incident light beam experiences after being reflected off a surface. The measurements of polarization can then be used to calculate some optical properties of the thin film. The refractive indices (n) and extinction coefficients (k) of the metal oxide thin films and silica barrier glass were extracted using models based on ellipsometry measurements of ψ and δ over 300 - 1300 nm from angles of incidence 64° , 67° , 70° , 73° and 76° (Figure 4.9). Analysis of the raw data was performed using the Spectroscopic Ellipsometry Analysis (SEA) software. The models for the fittings were based on a simple structure of the material surfaces, including the 50 nm silica barrier layer which was fitted separately and then incorporated into the metal oxide models. Additional diffusion layers between the distinct layers accounting for the rough surfaces and voids at the interfaces (see Figure 4.8) were inserted if the model did not fit well with the experimental data.

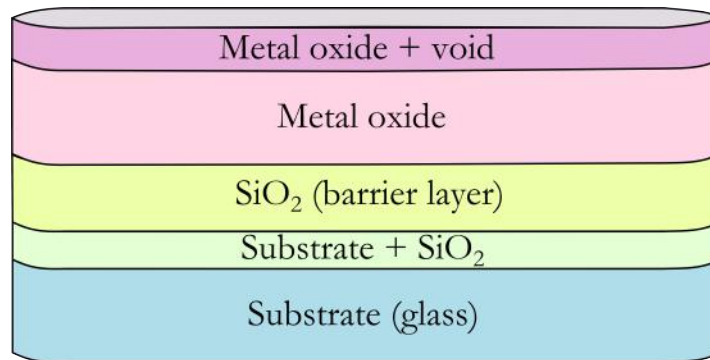


Figure 4.8: Simple diagram showing the basic model used to calculate ψ and δ from ellipsometry measurements

The surfaces were modelled from basic dispersion laws whereby the calculations were inputted with initial thicknesses obtained from side-on SEM that had been correlated with Filmetrics measurements - ZnO (Tanguy and Drude), Ga_2O_3 (Cauchy), SnO_2 (Tauc-Lorentz, Sellmeier and Lorentz), Al_2O_3 (Cauchy), MgO (Cauchy) and TiO_2 (Tauc-Lorentz, Sellmeier and Lorentz).

The range of ellipsometric data modelled (Figure 4.9) was narrowed to focus on the points of interest (visible range) since the dispersion laws do not describe the materials' response well within the whole wavelength range measured. Fudge factors such as effective medium approximations were not used to prevent false-fitting of data.

The roughness of the thin film surfaces did not detrimentally affect the reflectance with a sufficient intensity being detected for measurement of the ellipsometric data, ψ and δ . Measurements were fitted at wavelengths below the band gap energy where interference patterns were observed due to internal reflections between the thin films and the substrate. At energies above the band gap, absorption occurs from interband transitions and this is where the fitted model deviates from experimental measurements.²²⁹ Any significant structural inhomogeneity can be modelled by treating the films as separate layers (Figure 4.8).²³⁰ The selection of incident angle for the ellipsometric measurement is critical for a textured surface, since it leads to scattering and self-absorption in the TCO which could lead to inaccurate measurements. Errors can also be introduced since the films are not as atomically smooth as, say if the metal oxides were deposited with molecular beam epitaxy. However, deviation from the fit due to sample structural inhomogeneity was overcome by measuring ellipsometric data and fitting the model over a range of angles.^{230,231}

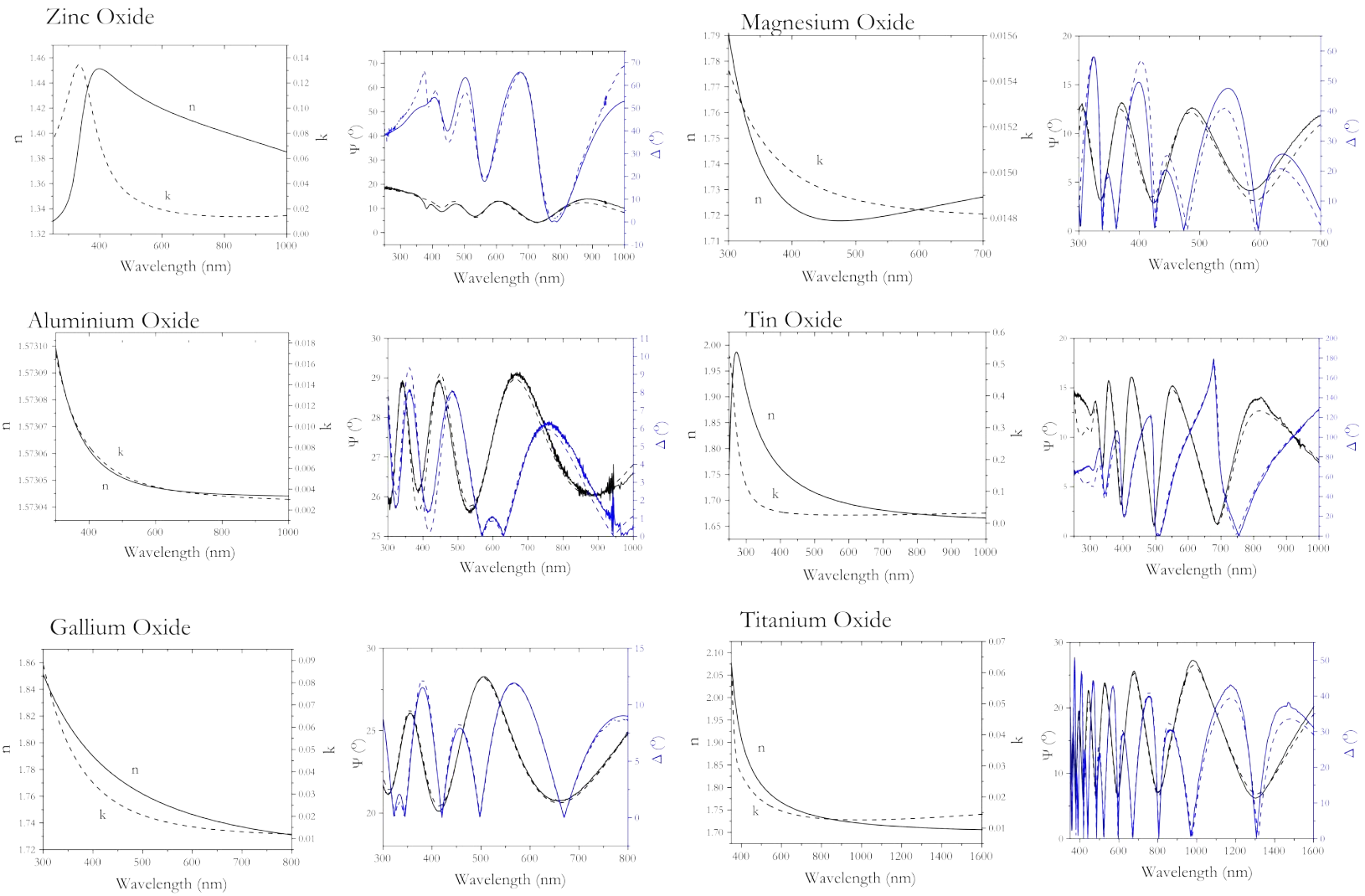


Figure 4.9: Refractive index, n , extinction coefficient, k , and the observed and fit of ψ and δ from ellipsometry measurements.

Refractive index values based on calculations from the models are displayed in Table 4.2 with n values quoted at 550 nm (within the range of the AuNPs' SPR maxima) and 632.8 nm (HeNe laser wavelength) along with some references from the literature. Most of the calculated n are similar to ellipsometrically based data in the literature apart from the titanium oxide where our measured value differed from the reference at 650 nm by -0.32, with differences arising probably because of deposition method since the reference refers to a sol-gel deposited film whilst the film discussed here was generated from AACVD. The fit for all the models were good, all fitting with an R^2 value of above 90 %, apart from MgO where the best obtained $R^2 = 87$ %.

Table 4.2: Calculated refractive indices of various metal oxides modelled from ellipsometric data.

Material	Film thickness (nm)	n at 550 & 632.8 nm	reference n
SnO ₂	385	2.10 & 2.08	2.12 at 650 nm ⁷⁶
Ga ₂ O ₃	380	1.79 & 1.78	1.92 at 632 nm ²³¹
TiO ₂	525	2.53 & 2.49	2.17 at 650 nm ²³²
ZnO	560	1.79 & 1.77	1.95 at 650 nm ²²⁹
Al ₂ O ₃	435	1.57 & 1.57	1.64 at 632.8 nm ²³³
MgO	385	1.72 & 1.72	1.73 at 650 nm ²³⁰

4.4.4 SPR of gold nanoparticles and composites

It is appreciated that the size and shape of the nanoparticles will affect the SPR as has been discussed earlier in this thesis in Chapter 3, however the discussion here on SPR mainly relates to the differences in the metal oxide character of the composite since it is assumed that the all the gold nanoparticle films are identical and undergo identical processing conditions during composite layer formation. All SPR absorbances observed from the AuNP films were red-shifted

after composite formation through overlaying with metal oxides (Figure 4.10). From some of the optical spectra, the interference pattern from the metal oxide can be misleading in that it looks like a double maxima from two SPR absorptions. The largest shift was seen with the AuNP:MgO at 79.6 nm and the smallest shift was seen with the AuNP:ZnO at 17.9 nm (see Table 4.3). From the graph in Figure 4.11, no direct correlation was found between the refractive index of the metal oxide and the amount of SPR shift.

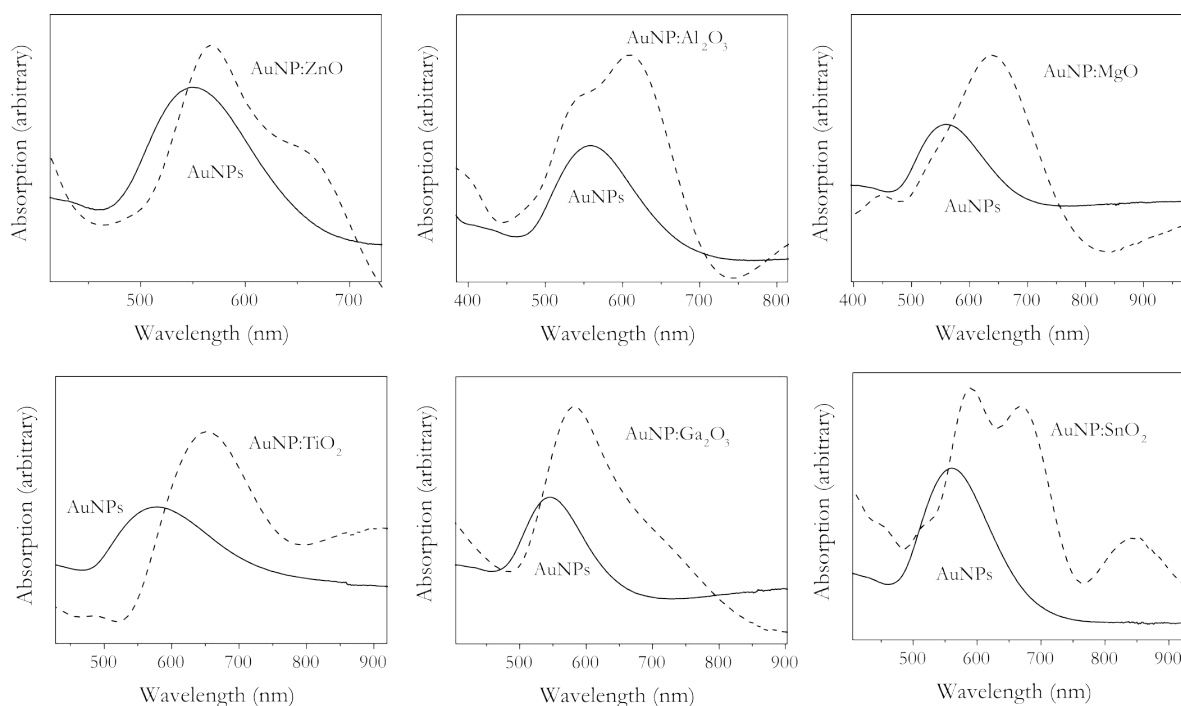


Figure 4.10: The shifts in SPR absorption before and after forming composites with various metal oxides.

Individual NP measurements of SPR have shown to display an increasing SPR shift with increasing refractive index of surrounding media.²²² The experimental set up here is drastically different and measurements could be assumed cruder since the SPR was measured collectively from all the AuNPs. However, the results here are still of interest as it relates more closely to industrial deposition processes. In CVD synthesis there will exist non-uniform contact between the nanoparticles and the different metal oxide thin films due to the roughness

4. Effect of Metal Oxide Character on the SPR in Composites with AuNPs

of both the gold nanoparticles and the metal oxide surfaces. The types of CVD reactions that occur and where, in the gas phase or on the surface of the gold nanoparticles, will determine whether the metal oxide is in close proximity to the gold nanoparticles, and therefore the extent to which the changes in metal oxide refractive index will affect the SPR of the composite film.

There is also the possibility that the size and shapes of the AuNPs might have been altered during the second stage deposition of the metal oxide due to the high temperature environments.¹⁵³ However, the temperature used for metal oxide depositions were all at 450 °C which was the same temperature as for the AuNP deposition and it was discussed in Section 4.4.1 that it was unlikely that the AuNPs would change to become red shifted because of an increase in size. On the other hand, because during the second deposition the reactor contained other reactants, i.e. metal oxide precursors and solvent, these could react and affect the final size of the AuNPs, and therefore shift the observed SPR.

Table 4.3: Shift in SPR of AuNPs before after composite formation with metal oxide.

Material	SPR maximum of AuNPs (nm)	SPR maximum of composite (nm)	SPR red shift (nm)
SnO ₂	560.6	591.0	30.4
Ga ₂ O ₃	545.3	582.2	36.9
TiO ₂	579.0	652.9	73.9
ZnO	549.8	567.7	17.9
Al ₂ O ₃	559.5	609.9	50.4
MgO	559.5	639.1	79.6

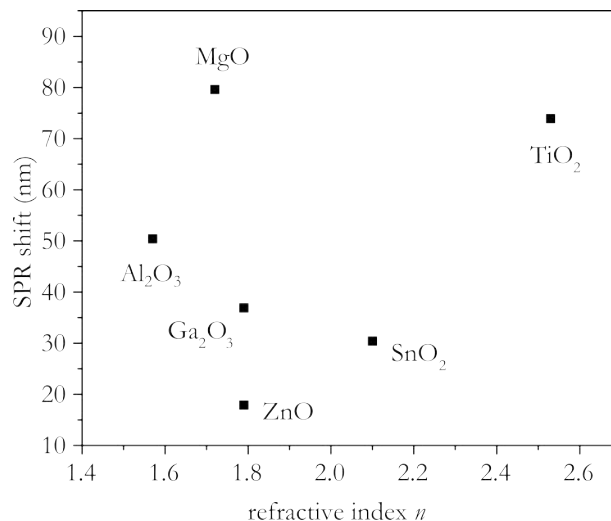


Figure 4.11: Graph showing the SPR shift of composites formed with gold nanoparticles and various oxides: Al_2O_3 , MgO , Ga_2O_3 , ZnO , SnO_2 and TiO_2 and the corresponding refractive indices as measured from the individual metal oxides.

4.5 Conclusion

Using AACVD gold nanoparticle and metal oxide composites were synthesised by layering various metal oxides onto AuNP films. The optical properties such as refractive index and extinction coefficient of the individual metal oxides (SnO_2 , TiO_2 , ZnO , MgO , Al_2O_3 and Ga_2O_3) were analysed using spectroscopic ellipsometry. After overlaying the metal oxides onto the AuNPs, there was found to be a change in the SPR, red-shifting the maxima, but without direct correlation to the refractive index of the metal oxides. The reactions that occur to form the different metal oxides can vary wildly in terms of rate and location, and therefore resulting in a different structure and interface between the gold nanoparticles and the metal oxides.

The lack of correlation between the refractive index of the surrounding media, i.e. between the metal oxide and the SPR shift, as has been found for previous reports,^{222,223} was attributed to the imperfections and differences between the AACVD deposition of the metal oxides as well as potential changes

4. Effect of Metal Oxide Character on the SPR in Composites with AuNPs

in the AuNPs themselves. The AuNPs could have been altered during the second heating stage, either due to Ostwald's ripening, melting or from further reactions.

Nevertheless, this chapter shows the adaptability of the AACVD system through layering to create composites of AuNPs with a wide range of metal oxides. Further improvements to the metal oxide for functional properties can be made from adjusting the reaction conditions.

Chapter 5

Gold Nanoparticles on Silica Wool

5.1 Introduction

One of the main applications for gold nanoparticles are as catalysts used in the industrial production of chemicals and vehicular catalytic converters.²³⁴ The AuNPs are normally dispersed and supported on a surface which is typically made up of a metal oxide as the observed catalytic activity is inherently linked to these support structures.²³⁵ Despite this, unsupported gold nanoparticles do still show significant activity in many other different important catalytic reactions.²³⁶

In Chapter 4, AACVD was shown to simply and effectively deposit gold nanoparticles from auric acid without the need for surfactants or additional reducing agents onto silica-coated flat glass surfaces which means there are no carbonaceous surfactants or residues. For applications such as catalysis, immobilisation of catalysts onto a substrate with a high surface area is beneficial as it will allow for an increase number of available active sites and ease of removal and recycling. We therefore proposed to deposit on a high surface area substrate of glass wool, where the silicon dioxide can also act as the support metal oxide increasing the overall activity of the catalytic system. This is anal-

ogous to the work in Chapter 3 where the auric acid is deposited onto silica barrier coated glass. AACVD's advantage of being a non line-of-sight deposition method is utilised here as the substrate is not flat. In the results from this chapter, we describe the AACVD route used to deposit gold nanoparticles onto glass wool substrates. Preliminary experiments involving the oxidation of benzyl alcohol were also performed to test the catalytic activity of the gold nanoparticles deposited in this way.

5.2 AACVD of gold onto glass wool

Experimental

AACVD set up

Glass (silica) wool was purchased from Sigma Aldrich. About 1 g of glass wool (GW) was placed in between the top and bottom plates of the reactor as in Figure 5.1. The amount of GW was chosen so that it was the maximum amount able to fit in the reactor without hindering the flow of auric acid. Too much GW resulted in highly concentrated depositions near the inlet, whereas too little GW and the majority of gold aerosol just flowed through the wool finally depositing on the top and bottom plates. Air was used as the carrier gas with flow rates of $3\text{-}4\text{ Lmin}^{-1}$.

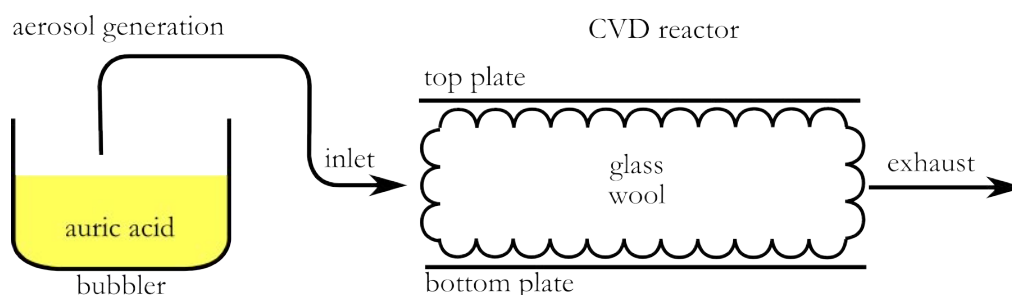


Figure 5.1: Aerosol-assisted chemical vapour deposition set up of gold nanoparticle deposition onto glass wool.

Precursor solutions

Hydrogen tetrachloroaurate(III) hydrate solution (Alfa Aesar) was dissolved in methanol and used immediately. A range of concentrations were investigated consisting of 0.01-1 mmol of auric acid in 20-100 ml methanol.

5.2.1 Results

Precursor concentration

Typically 1 g of glass wool was used for a deposition (weighed prior to deposition) which amounts to a surface area of 6.72 m² as measured from BET (Brunauer–Emmett–Teller) experiments. A typical sheet of float glass substrate used in this AACVD reactor has an area of 0.065 m² (4.5 × 14.5 cm), comparably the glass wool has about 100 more times the surface area. For the coverage of AuNPs on the wool to be the same as on flat float glass, then precursor concentrations would have to increase 100-fold. However, increasing the amount of auric acid in the precursor solution only resulted in larger sized gold particle deposits. For example when increasing the auric acid amount from 0.2 to 1 mmol, the colour of Au deposits changed from pink/purple (Figure 5.5) to orange (Figure 5.2), especially near the inlet. It normally requires less energy for the auric acid aerosol droplets that enter the reactor to undergo reduction onto sites where gold nanoparticles have already formed which act as seeds, rather than forming new gold nanoparticle sites. Therefore, increasing the auric acid concentration does not increase the amount of AuNPs but just the size of the particles.



Figure 5.2: Photograph of gold particles deposited by aerosol-assisted chemical deposition from auric acid (1 mmol) in 100 ml methanol with air (4 Lmin^{-1}) at $350 \text{ }^\circ\text{C}$.

Phase and adherence

SEM images of the blank GW substrate (Figure 5.3) showed a relatively smooth surface with a few dust particles attached. Overall, all the substrate strands were quite uniform in terms of diameter and surface morphology.

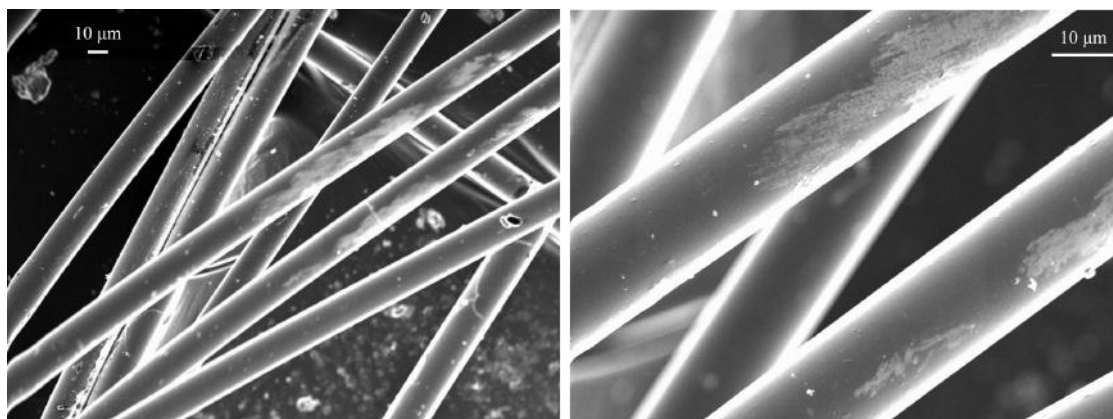


Figure 5.3: SEM of blank glass wool.

In a normal AACVD set up using float glass as a substrate the aerosol flows in a laminar fashion between the top and bottom plates. However in this set up the presence of glass wool disrupts the flow and higher flow rates were needed

to force the aerosol in between glass wool, 3-4 Lmin⁻¹ instead of 1-2 Lmin⁻¹ for flat substrates as described in Chapter 3 and 4. The AuNP:GW was ground up in a pestle and mortar and an XRD taken from a capillary tube. The XRD pattern shown in Figure 5.4 displayed cubic metallic peaks with a high background because of the nanoparticulate nature of the gold combined with the amorphous particles of glass wool.

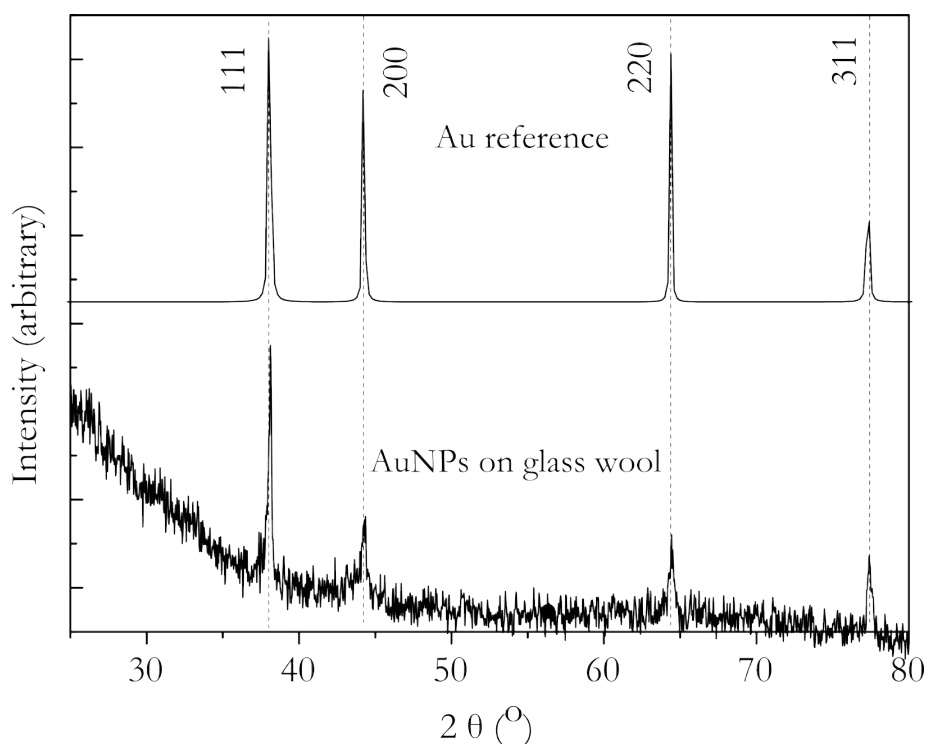


Figure 5.4: XRD pattern of AuNPs deposited onto glass wool showing cubic Au reflections with reference.¹⁹

The gold nanoparticle deposits were robustly adhered to the glass wool, not becoming detached even when placed in hexane, decane or acetone which is promising for reusability in solution based catalytic reactions. They also remain unchanged for long periods of time of up to two years, even when kept in an ambient temperature and environment.

Deposition pattern and colouration

Photographs in Figure 5.5 compare AuNP depositions onto glass wool using the same concentration of auric acid (0.2 mmol in 50 ml methanol) but at different flow rates of (a) 3 Lmin⁻¹ and (b) 4 Lmin⁻¹. When auric acid is reduced to metallic gold, the product is always coloured (except for nanoparticles less than 2 nm in size), which enables us to utilise colouration and intensity of colour as an indication of deposition. In general, gold nanoparticles were observed to have a coloured appearance ranging from blue to red, with the SPR shifting towards the red with increasing particle size.^{209,237} CVD of AuNPs onto float glass also results in a pink/purple appearance (see Chapter 3), and as the nanoparticles agglomerate to larger bulk-like particles, the SPR absorption starts to decrease leaving the typical gold metal absorptions from the d to conduction band²³⁸ giving rise to an orange coloured appearance similar to depositions from high auric concentrations as described in Section 3.5.4.

The depositions described here were of a pink and purple colour as seen from the photographs (Figure 5.5). They clearly show a more even spread of AuNPs along all of the glass wool when depositions had taken place at a higher flow rate. The aerosol was better able to travel down the reactor when the flow rate was higher as at a lower flow rate the loss of momentum in the aerosol will be greater, leading reactions and agglomerated depositions by the inlet. A higher flow rate gives the unreacted auric acid droplets a chance to travel further down the reactor before depositing on the glass wool. By the inlet bigger particles were formed with sizes larger than 1 μm , instead of the desired nanoparticulate morphology of less than 1 μm .

Gold depositions were also detected on the glass top and bottom plates (Figure 5.1), particularly around the outside edges wherever the aerosol was able to come in contact with them. These depositions consisted of pink/purple

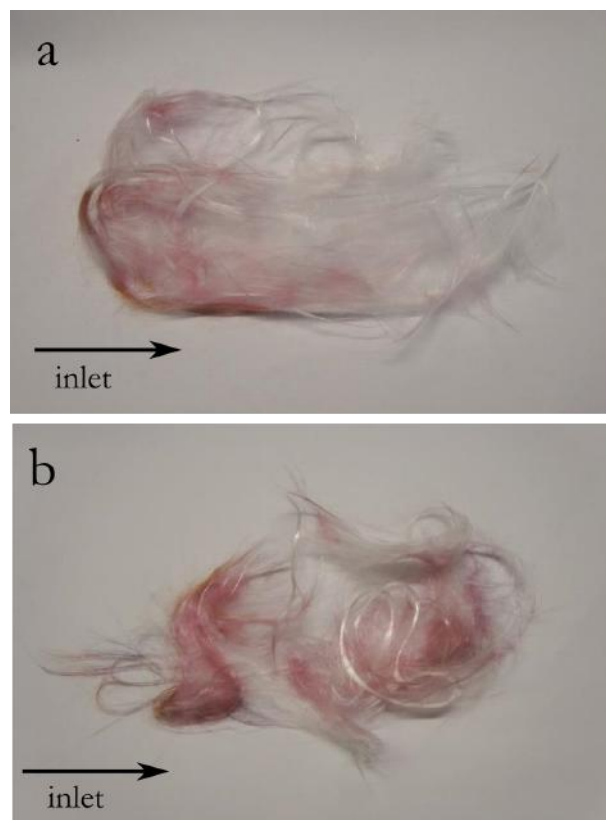


Figure 5.5: Differences of gold nanoparticles deposited onto glass wool by aerosol-assisted chemical deposition from auric acid (0.2 mmol) in 50 ml methanol with air at (a) 3 and (b) 4 Lmin⁻¹ at 350 °C.

nanoparticles as well as highly concentrated metallic yellow gold. There seems to be a preference for gold to deposit on the plates since all the areas that were exposed to the aerosol from lack of GW were covered in gold. As the glass plates are denser than the GW, they were able to absorb more and lose less heat, resulting in a hotter surface than the GW where it is easier for auric acid to break down. Depositions were even found on the top plate which indicates that even though it was further away from the heating element compared to the GW, their denser structure meant it was efficient at retaining heat radiating from the carbon block, again resulting in a higher temperature and more gold deposition reactions. On the other hand, the deposition efficiency might have been identical for both substrates but since the surface area of the GW is about 100 times more than the glass plates per sample used in the deposition,

the gold amount per area would be higher and look more intense on the glass plates.

Particle sizes

Large dispersions of nanoparticle sizes were observed from all auric acid depositions on glass wool (see example TEM in Figure 5.7), regardless of precursor concentration. The large dispersions indicate that the nanoparticle formation processes were not as uniform as depositions onto flat substrates, whereby there was a trend for deposits from lower auric acid concentrations to result in smaller nanoparticles with a narrower dispersion (Section 3.5). The substrate orientation in relation to the aerosol inlet was random for each deposition because the fluffy nature of the glass wool made it difficult to arrange the wool in a perfectly identical manner for each and every deposition. This resulted in a slightly different flow path of aerosol and heat distribution in the reactor for every deposition. However, on average AuNPs with a largely pink/purple colouration were able to be repeatedly deposited on a large area of glass wool.

Figure 5.6 displays SEM images comparing between a red/orange and a pink coloured sample obtained from a single glass wool deposition using 0.2 mmol of auric acid and a flow rate of 3 Lmin⁻¹. As photographs of the deposition pattern show (Figure 5.5, the red/orange deposits were found near the inlet and around the edges, whilst the pink deposits were found in the majority of the central areas, fading out towards the outlet as the precursor was depleted. The red/orange colouring of the deposits indicate gold in the form of larger particle sizes and indeed corresponded to platelet shaped gold particles of sizes 500 nm to 1 µm in the SEM images (Figure 5.6). Pink areas indicate nanoparticulate gold which agrees with the SEM images where particles of 100-500 nm were observed.

TEM images reemphasise the large dispersion of AuNPs found when auric

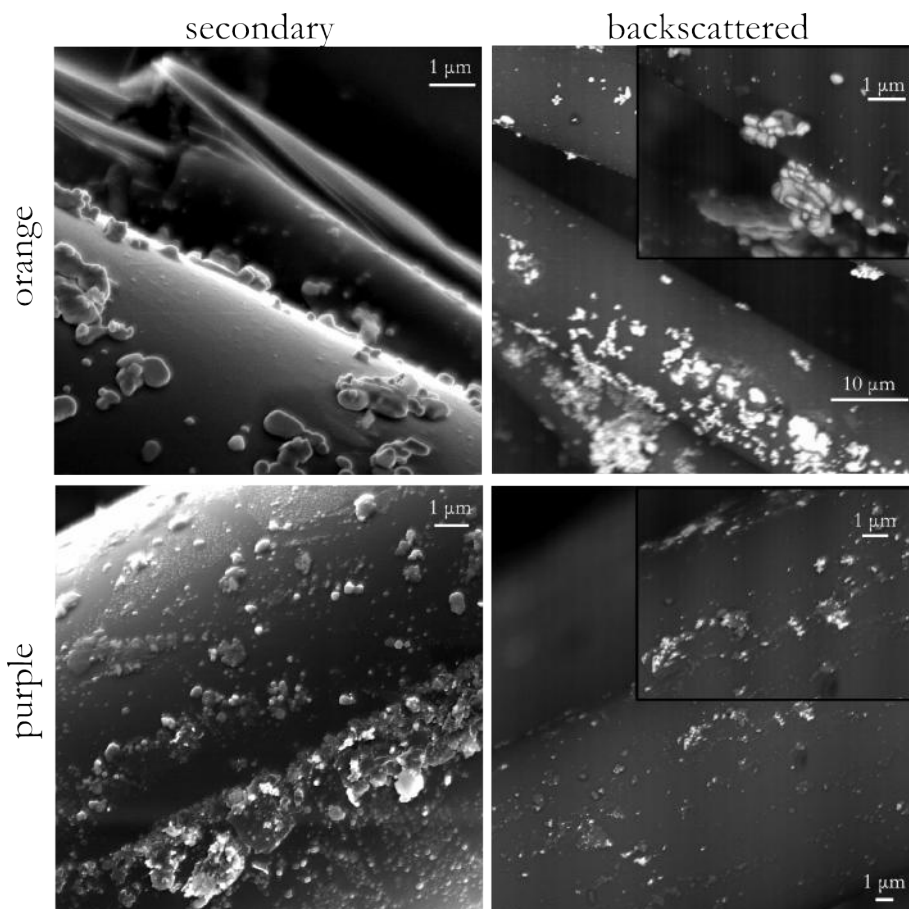


Figure 5.6: Secondary and backscattered electron SEM images of AuNPs deposited on glass wool showing a more agglomerated and larger particle sizes from the orange areas using and smaller individual gold nanoparticles from the purple areas. The AuNPs are imaged as whiter and lighter shades on the backscattered images. The AuNPs were synthesised from an aerosol-assisted chemical deposition using a precursor solution of auric acid (1 mmol) in 100 ml methanol with air (4 Lmin^{-1}) at $350 \text{ }^\circ\text{C}$.

acid was deposited onto glass wool substrates. TEM images in Figure 5.7 show that particles of more than 500 nm as well as nanoparticles down to sizes of 25 nm can be produced in a single deposition. The shape of the larger particles (about 500 nm to $1 \mu\text{m}$) suggest that some of them were formed from agglomeration of smaller particles. For gold particle depositions on a flat substrate, the larger particles are pushed upwards by thermophoresis, acting as a filter for the bottom plate where smaller gold nanoparticles with a smaller dispersion can settle and deposit. Since the glass wool occupied all the space between the

5. Gold Nanoparticles on Silica Wool

bottom and top plates, the screening effect of thermophoresis was not felt by the AuNPs resulting in depositions regardless of size variations.

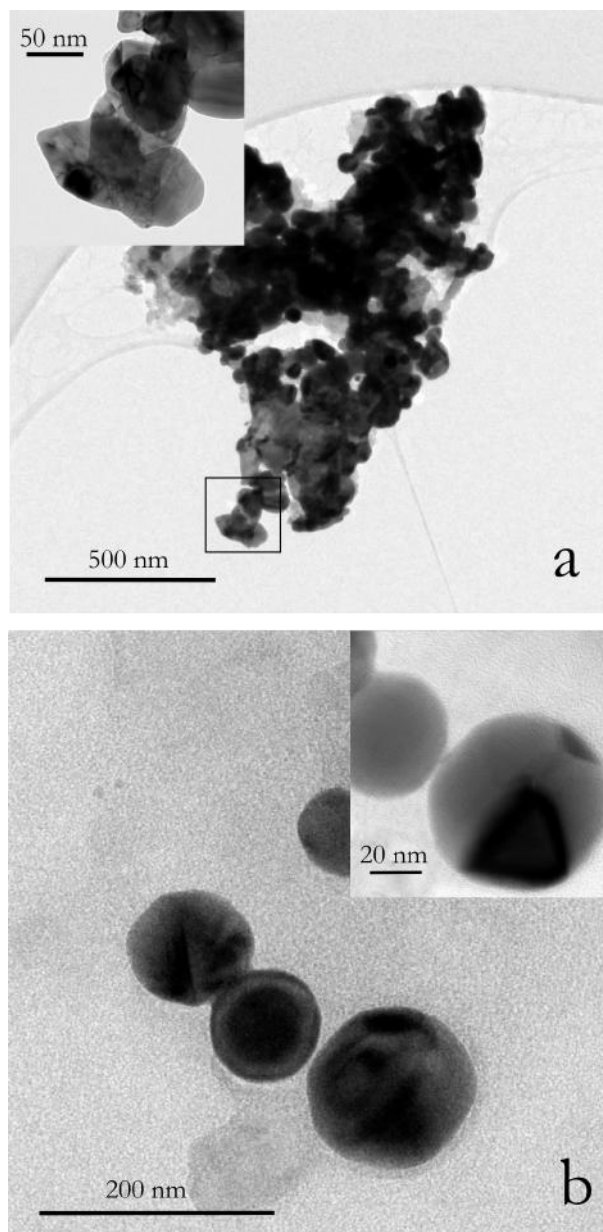


Figure 5.7: TEM images showing agglomerated and individual gold nanoparticles that were deposited by aerosol-assisted chemical deposition from auric acid (1 mmol) in 100 ml methanol with air (4 Lmin^{-1}) at $350 \text{ }^\circ\text{C}$.

5.2.2 Summary

Aerosol-assisted chemical vapour depositions is a viable way to deposit gold nanoparticles onto glass wool. The size dispersion of AuNPs were large however, and fine tuning of the AACVD set up needs to be conducted in order to be able to have a more controlled deposition that results in a narrower AuNP size dispersion. Even though the specific locations of deposition on the glass wool might be slightly unpredictable, in general the colour and area covered by Au can be reliably repeated. A separate set up of spray deposition rig was also found effective at depositing AuNPs which will be discussed in Section 5.4.

5.3 Benzyl alcohol catalytic reaction

AuNPs acts as catalysts for many reactions and the oxidation of alcohol activity is reported here.²³⁹ In general for reactions involving gold nanoparticles as the catalyst, when using the same weight the smaller the nanoparticles, the more surface area would be exposed and so the more active the catalyst.²⁴⁰ The reaction tested here to confirm the catalytic activity of the gold deposited on glass wool involves the selective oxidation of benzylalcohol to benzaldehyde without over-oxidation to benzoic acid and benzyl benzoate (Figure 5.8). The formation of the aldehyde is an important step in many pharmaceutical, agrochemical and perfume industries. A good catalyst has to be efficient, effective and selective, achieving a high percentage of desired product in the least amount of time.

Normally benzaldehyde undergoes autoxidation in the presence of oxygen to benzoic acid very easily in ambient conditions and with increased rate in the presence of a catalyst.²⁴¹⁻²⁴⁴ However, there have been numerous reports of over 99 % selective catalytic conversion reactions to benzaldehyde from benzyl

alcohol, and other such analogous reactions, even within highly oxygenated environments.²⁴⁵⁻²⁴⁷ EPR studies have shown that the presence of molecules with activated hydrogen atoms, such as the C-H bond in benzyl alcohol, can inhibit the autoxidation by hydrogen transfer, intercepting the free radicals involved in the radical chain reaction.²⁴⁸ Other molecules such as allylic alcohols can also inhibit in a similar way, but toluene or methanol do not as they have less activated hydrogen atoms.

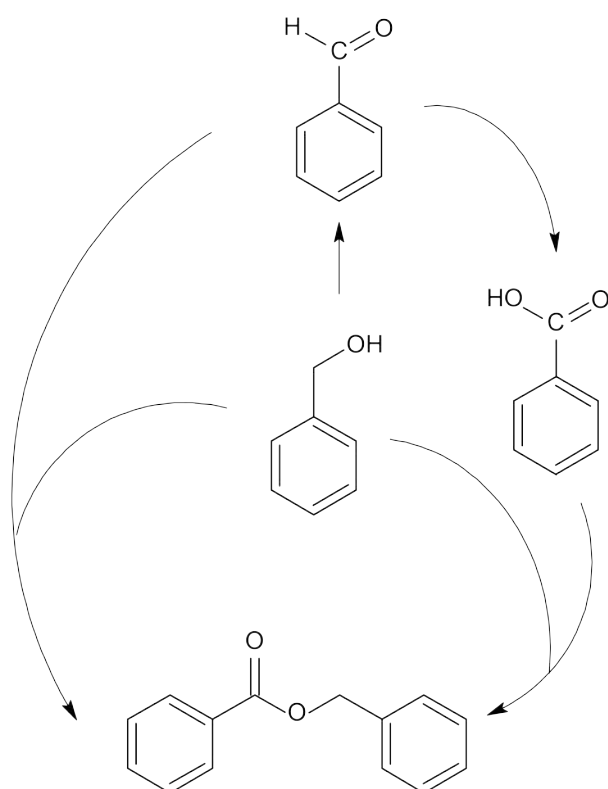


Figure 5.8: Reaction scheme showing the oxidation of benzyl alcohol to benzaldehyde and further oxidation to benzoic acid and benzyl benzoate.

5.3.1 Experimental

Reaction mixture

Benzyl alcohol, tert-butyl hydroperoxide, dodecane and decane were placed in a glass container which fits into the heating element. 0.1 g of an orange and a

purple area of gold deposited glass wool were tested separately, both deposited from 1 mmol of auric acid in methanol (50 ml) at 350 °C with an air flow of 4 Lmin⁻¹.

Technical details

A mechanical stirrer was fitted into the glass vessel containing the reaction solution to try and ensure even distribution of reactants and catalyst (Figure 5.9). Firstly, the chemicals were added sequentially into the vessel as in Table 5.1, then the stirring mixture was slowly heated to 90 °C, maintained and left for 4 hours in a Mettler Toledo Multimax RB-04 that was programmed with computer software. A condenser was placed above the reactor in order to prevent loss of reaction mixture. Aliquots (0.2 µl) of solution were extracted, before the addition of the AuNP:GW (0.1 g), every 15 minutes during the first hour, then every consequent hour. The aliquots were stored in a fridge and analysed in a flame ionisation detector (FID) gas chromatographer (GC). Dodecane was used as the internal standard for quantitative calculations as it wasn't involved in any reactions.

Table 5.1: Chemicals in the reaction mixture for the catalytic oxidation of benzyl alcohol.

Chemicals in order of addition	Amount ($\times 10^{-2}$ moles)
Benzyl alcohol	4.4
Tert-butyl hydroperoxide	10.3
Dodecane	2.0
Decane	2.6

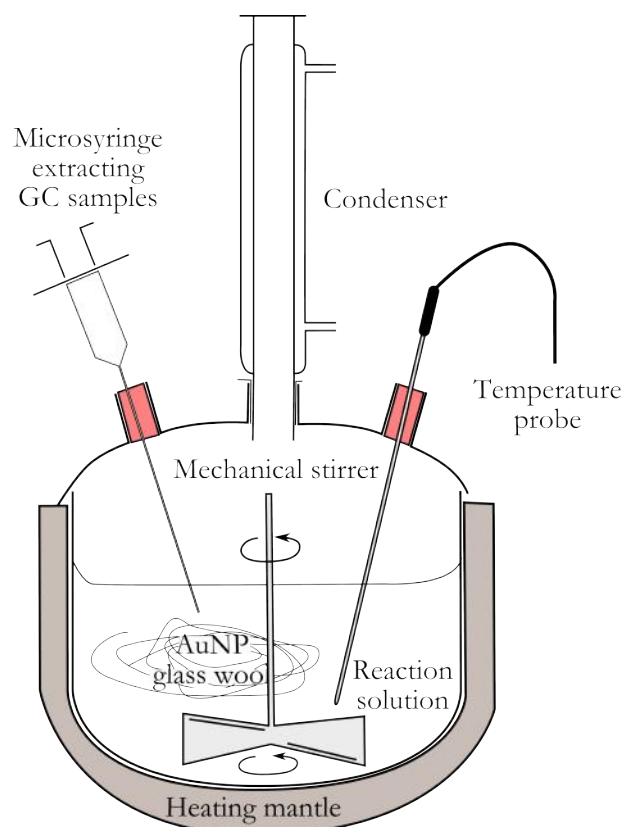


Figure 5.9: The reaction vessel showing the reaction solution and AuNP (gold nanoparticle deposited) glass wool inside it being stirred by a mechanical stirrer. The temperature probe informs the power of the heating mantle, and the microsyringe is inserted into the reaction vessel in order to extract samples for gas chromatography (GC) measurements.

5.3.2 Results

The reaction mixture (Table 5.1) was heated to 90 °C and maintained at this temperature for four hours. Two different sets of gold depositions were tested, one from an orange area and the other a pink/purple area of gold deposition. As determined from the discussion in Section 5.2.1, the orange colouring indicate areas with high concentrations of larger particles where nanoparticles have agglomerated, and the pink/purple colour indicated areas where and at a lower concentration.

The GC spectrum in Figure 5.10 was taken from the reaction mixture prior to heating and it shows the time of flight peak positions for the individual com-

ponents. The progress of the reaction is followed by the decrease in benzyl alcohol peak as well as the formation of benzaldehyde, benzoic acid and benzyl benzoate. The quantities were calculated using the internal standard of dodecane.

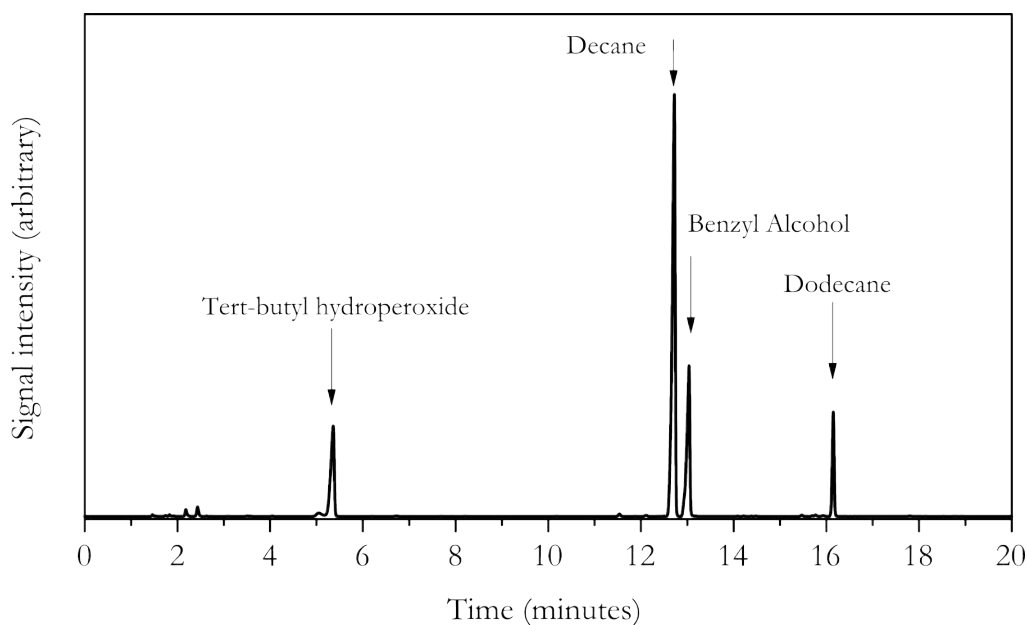


Figure 5.10: Gas chromatography signals of mixture prior to reaction showing the time of flight peaks of the different components.

Both the orange and purple areas showed catalytic activity although not very high conversion percentages. After four hours, the orange wool catalyst had oxidised benzyl alcohol to benzaldehyde with a 37% yield and 94% selectivity whilst the purple wool had only converted 16% at a similar selectivity of 97%. The high selectivity of these catalysts are in line with reports of gold catalysts in the literature which also show that selectivity is unaffected by particle size.²⁴⁹

When looking at the activity of the orange wool (Figure 5.11), a high conversion rate was measured at the beginning of the reaction period, with over half the total yield being produced in the first 15 minutes. The orange wool was clearly catalytically active even though the average particle size was more

than 1 μm . However, since there was a large dispersion in nanoparticle sizes even though the average particle size might not be small enough to be catalytically active, there would have been present smaller nanoparticles to carry out the reaction (see SEM in Figure 5.6). After this initial burst of catalytic activity, the conversion rate rapidly decreases and only a further 17% was converted in the following period up to the final reading taken at the 4 hour mark. The conversion did not reach 100%, and so it was postulated that if the catalyst had remain unchanged, the active sites must have become blocked in some way either by the presence of reactants or products during the reaction. This could be due to the nature of the strands of glass wool being in close proximity to each other and not allowing for sufficient reaction mixture agitation even with mechanical stirring in place.

A larger percentage yield might be expected from the purple wool since the colouring indicates smaller nanoparticles which have been shown to be better catalysts,²⁵⁰ however the final yield of benzaldehyde only reaches 16% after the four hour reaction period. Even though the smaller particles from the purple areas should be more catalytically active due to increase surface area, when looking at the SEM images in Figure 5.6 there was an actual reduction in the number of nanoparticles, resulting in a smaller number of active sites when compared to the orange wool. The purple wool would also suffer from blockage of the active sites due to the nature of the glass wool and so the conversion rate would further decrease.

5.3.3 Summary

The catalytic activity of two different areas of gold nanoparticle deposition on glass wool were tested with an important alcohol oxidation reaction. The areas were differentiated by colour and therefore roughly divided by nanoparticle

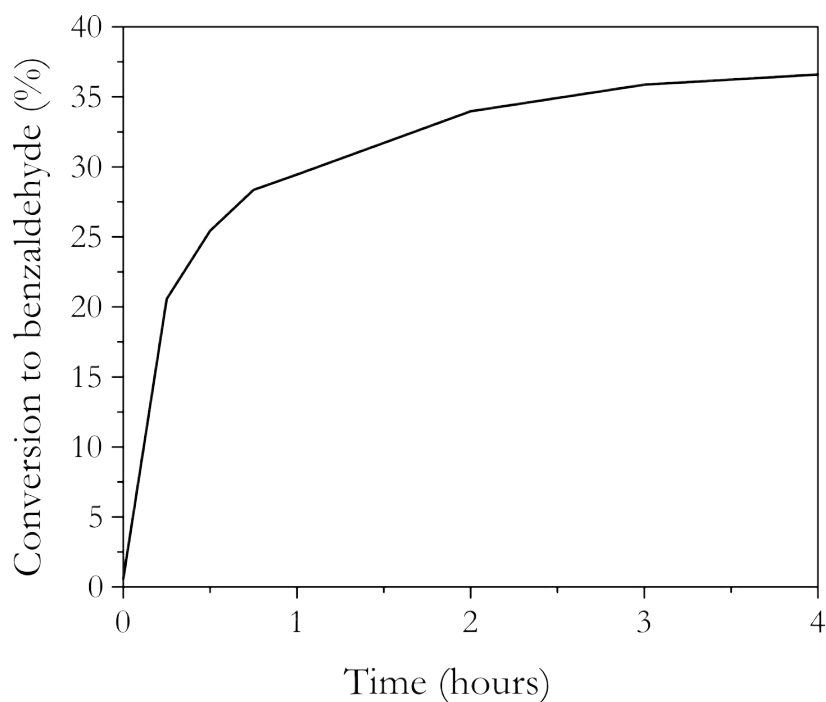


Figure 5.11: Conversion rate of benzyl alcohol oxidising to benzaldehyde with tert-butyl hydroperoxide catalysed by gold nanoparticles immobilised on glass wool with an orange colouring.

sizes. The selectivities of the tested AuNP:GW were high at 96-97% conversion of benzyl alcohol to benzaldehyde agreeing well with previous studies.^{170,251} However the yield was quite low when compared to the literature, possibly due to active sites being blocked by products or by-products during the reaction. As was discussed in more depth in Section 5.2.1, the AACVD of gold on glass wool resulted in a large dispersion of AuNP sizes. So even though the orange wool had on average larger particles, there were actually large amounts of catalytically active nanoparticles of below 50 nm present. As expected, the purple areas of glass wool which had nanoparticles of lower than 50 nm were also catalytically active. The differences in catalytic activity was in this case dependent on the amount of Au not the size of the nanoparticles as the orange wool achieved a higher yield than the purple wool.

5.4 Spray deposition of gold nanoparticles onto glass wool

In order to try and avoid the large dispersion of gold nanoparticles obtained from the AACVD of auric acid onto glass wool (Section 5.2) depositions using a spray rig were also tested. The formation of nanoparticles should be less dependent on the nature of the glass wool substrate since most of the path travelled by the aerosol is not affected by the substrate, unlike an AACVD reactor where the aerosol comes into contact with the glass wool upon entering the reactor (Figure 5.1). The particles of gold deposited using the spray rig suggest that the auric acid undergoes a spray pyrolysis mechanism, as the shape suggests that the spray droplets only vapourise and react after landing on the heated substrate.

5.4.1 Experimental

Spray set up

The precursor solution of auric acid (0.01-0.02 mmol) dissolved in a mixture of methanol and acetone (1:5) was injected into a chamber where a high pressure stream of N₂ pushed the solution through a pneumatic atomizing nozzle creating a downward flow of aerosol towards the substrate which was heated to 350 °C (see Figure 2.2). Pyrex[®] glass wool (Corning[®]) was obtained as long strands and wrapped around a piece of 2.5 × 2.5 cm float glass weighing it down and securing it on the carbon block. On a macroscopic level the Pyrex[®] glass wool looks different to the glass wool used in Sections 5.2 and 5.3, however when comparing SEM images (Figure 5.3 and 5.12), on a microscopic level they are actually identical, with uniform width (about 12 nm in diameter) and a smooth surface.

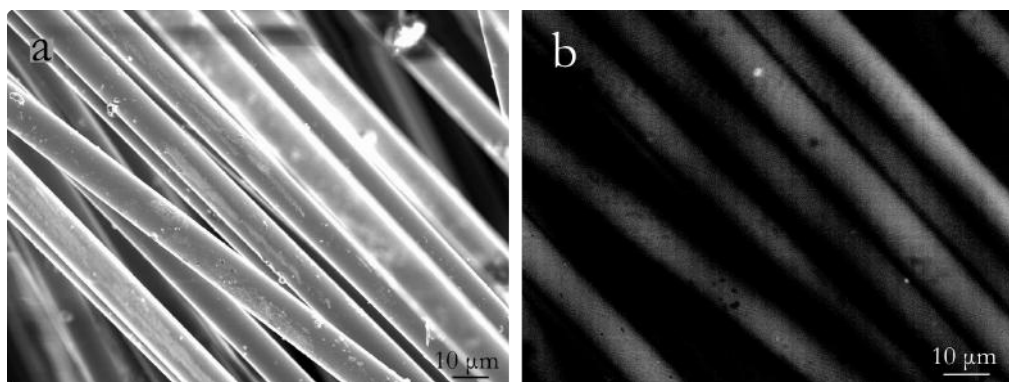


Figure 5.12: Secondary (a) and backscattered (b) SEM image of Corning glass wool.

5.4.2 Results

Colour

The auric acid deposits in nanoparticulate form as seen from the pink and purple colouration of the photographs in Figure 5.13. The colour of the deposit outlines the shape of the spray pattern on the top of the glass wool substrate which leads us to assume that the reduction of auric acid happens on or very close to the substrate, with the aerosol remaining unreacted as auric acid when travelling through the reactor making it a spray pyrolysis¹⁰⁶ rather than a chemical vapour deposition process. The coloured depositions were present wherever the spray stream hit the substrate and this makes the depositions easily predictable, reproducible and controllable. There were no areas of highly concentrated orange deposits, indicating a lack of agglomeration of the nanoparticles. Photographs in Figure 5.13 compare depositions from (a) 0.02 mmol and (b) 0.01 mmol of auric acid in the precursor solutions. No colour changes can be seen with increasing concentration, only an increase of purple colour intensity again confirming the lack of agglomeration of the nanoparticles compared with the AACVD method (Section 5.2). The nanoparticles can only be seen on the very top most layer of glass wool as the aerosol could not penetrate the layers of wool. This factor makes the rig inefficient at depositing large amounts

of AuNPs on a large fraction of the glass wool.

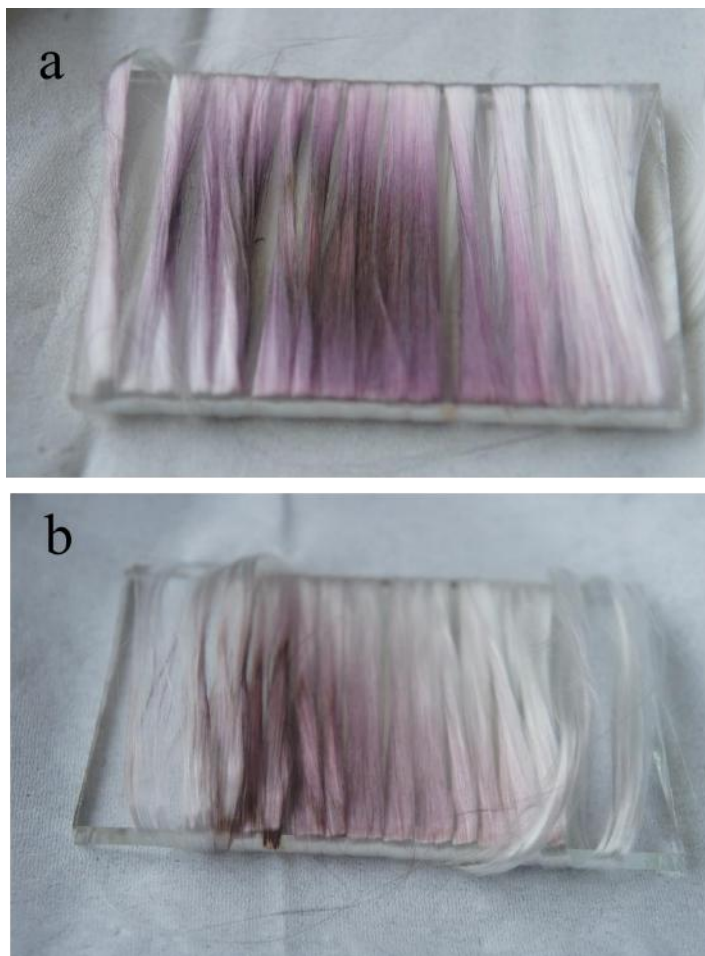


Figure 5.13: Photograph of gold nanoparticles deposited using a spray deposition method with (a) 0.02 mmol and (b) 0.01 mmol of auric acid in a mixture of methanol (5 ml) and acetone (20 ml).

Phase and morphology

The size and distribution of the gold nanoparticles on glass wool were investigated using SEM and TEM. Cubic gold nanoparticles with sizes ranging from 50-200 nm were found evenly distributed on areas of the glass wool where the spray hit and the purple colour was observed (Figure 5.14 and 5.15). The nanoparticles were all of a rounded nature but not of a uniform shape. This agrees with the theory that they form at a high rate upon arriving on the heated

substrate, rather than during their passage to the substrate, which might result in uniform and spherical nanoparticles. When comparing these with the nanoparticles deposited with AACVD (Section 5.3), we can assume that these might also be catalytically active.

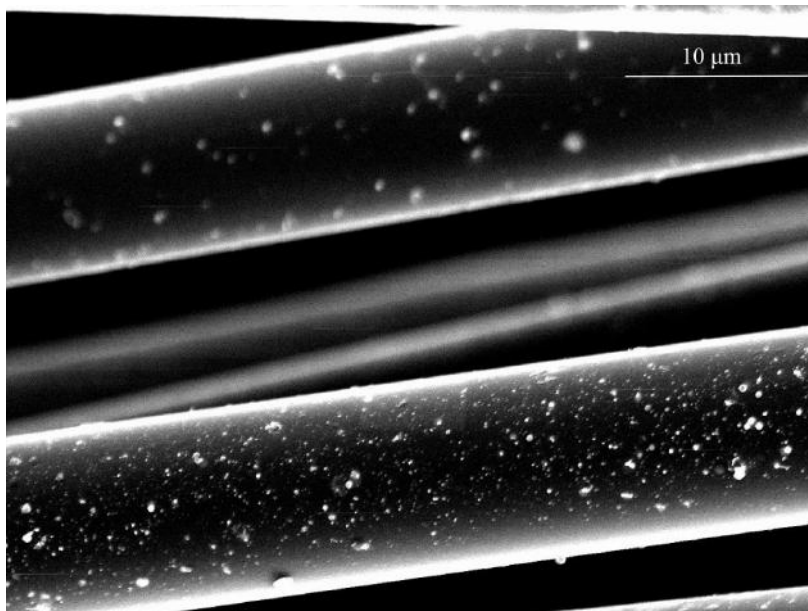


Figure 5.14: Scanning electron microscope image of gold nanoparticles (confirmed by EDX) on glass wool deposited by a spray deposition method.

5.4.3 Summary

Gold nanoparticles were formed quickly and easily using the spray deposition method. The formation of gold nanoparticles differed slightly with the AACVD method, as the aerosol comes into contact with the hot substrate before reduction into elemental gold. This resulted in the apparent visibility of the spray pattern formed from purple nanoparticulate deposits on the glass wool. The particles were all on the nanoscale 200 nm or less, but not of uniform shape. The rounded and flat nature of the nanoparticles suggest that the gold particles form upon impacting on the glass wool substrate rather than reacting first in the droplet suggesting a pyrolytic rather than a CVD process.

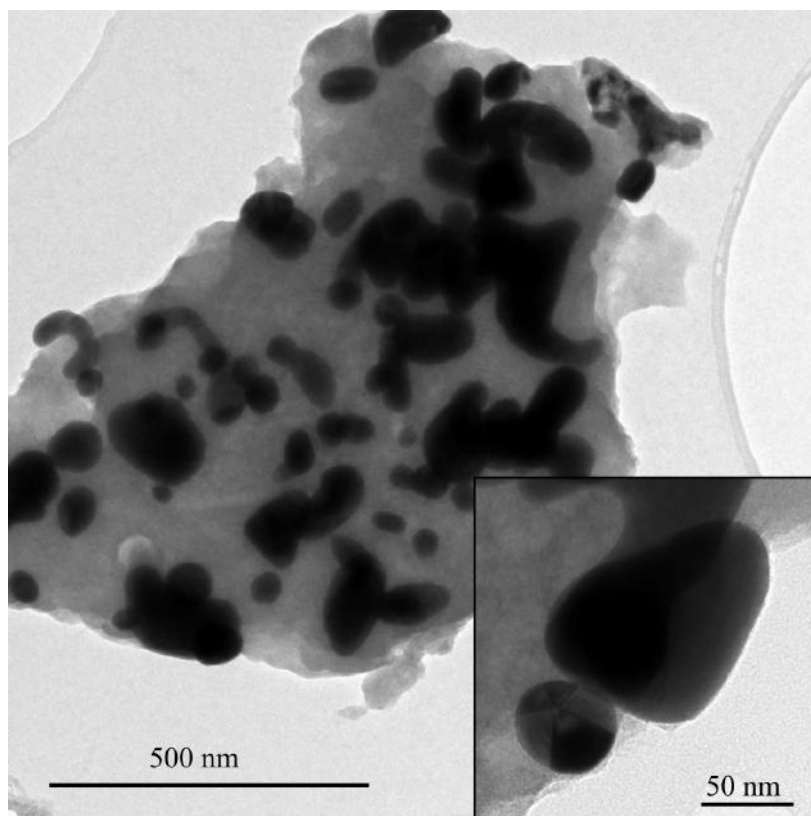


Figure 5.15: Transmission electron microscope image of gold nanoparticles on glass wool deposited by a spray deposition method.

5.5 Conclusions

Glass wool is a useful substrate for immobilisation of catalysts due to its large surface area. Here we report the first deposition of gold nanoparticles onto glass wool using two deposition methods differing in terms of aerosol generation and set up as shown in Figures 5.1 and 2.2.

In aerosol-assisted chemical vapour deposition (AACVD) the aerosol is formed by an ultrasonic humidifier and carried into the reactor with air flowing at 3-4 Lmin^{-1} , the speed and velocity of the aerosol droplets are relatively low compared with the travel path of the aerosol droplets from the spray rig. It was concluded that the gold was deposited through a spray pyrolysis method when using the spray rig as the spray aerosol did not seem to react prior to contacting with the surface. The pressure at which the aerosol droplets enter the reactor is

higher for the spray rig since the precursor solution is being forced through the nozzle head with a diameter of 0.4 mm. This force on the droplets combined with gravity ensures that the droplets flow in a downwards direction towards the substrate countering any convection forces that might be felt due to the temperature gradient found within the reactor. The downwards movement of the droplets will cause the droplet to alter its shape as it impacts on the surface. The shape of the landing droplet affects the final shape of the deposited nanoparticle and since non-uniform shapes of sizes smaller than 200 nm were observed we can assume that the reduction of auric acid happens quickly and more importantly, the nanoparticles are not subject to further reactions since further agglomeration into larger particles were not found.

From AACVD of auric acid onto glass wool, we observe nanoparticles of a larger dispersion between the sizes of 20 nm and 1 μm than from the spray rig. In AACVD the droplets travelling to the substrate do not feel the same pressure as if generated in the spray set up even though the flow rate is much higher at 3-4 Lmin^{-1} . The momentum from the carrier gas is reduced as the already formed aerosol has to be pushed upwards then laterally into the reactor through a wider inlet compared to the spray nozzle. The duration that the aerosol spends at a higher temperature before undergoing reduction is longer in an AACVD reactor and so the reduction of the auric acid can occur within the droplet itself before depositing on the substrate, leading to more spherical particles. The larger particles seem to have resulted from longer reaction times within the droplet, as there is a longer time before deposition, which were further encouraged because of the higher overall temperature found in the AACVD reactor since the reactor volume is much smaller when compared to the spray rig.

The large size dispersion of AACVD AuNPs can be observed from the variety of colour seen from the depositions. Pink and purple correlated to

nanoparticles smaller than 500 nm, and orange to nanoparticles larger than 500 nm up to 1 μm and above. These two areas were tested to see if they display any catalytic activity for the oxidation of benzyl alcohol to benzaldehyde. Both coloured areas was seen to have high selectivity to the desired product, 96-97% as expected from gold.²⁴⁹ However, the yield was low compared to other AuNP catalysts reported, with the pink/purple wool achieving a lower yield at 16% compared to 46% for the orange wool because of the closely packed nature of glass wool and catalyst immobilisation.

Since the Au particles formed from the spray deposition are in general smaller and with a narrower dispersion when compared to AuNPs from AACVD, they show promise for future work as they are expected to have greater catalytic activity which unfortunately due to time restraints we were unable to investigate. It was concluded that the Au particles were deposited via a spray pyrolysis method as from SEM images it can be seen that the shape of the particles were influenced by the way the droplet splashes on the surface. The one drawback of using this deposition process compared to AACVD would be the smaller surface area covered each deposition run, however this spray mechanism is more similar to industrial CVD glass coating processes.

Chapter 6

Conclusions

6.1 Summary of work

Reports in this thesis have shown that aerosol-assisted chemical vapour deposition reactor is a versatile tool for investigating a range of functional materials. Chapter 3 describes how SnO₂ can be consistently deposited and doped with F to make a high quality transparent conducting oxide material with a sheet resistance of around 10 Ω/□ and a visible transmittance of around 75-80% comparable to industrial standards and previous reports.^{69,79} Additional functionality can be added to the metal oxide films by way of making a composite with AuNPs.^{12,38,112} The full range of materials deposited and their important characteristics are shown in Table 6.1.

Detailed investigations into the depositions of AuNPs with auric acid are described in Section 3.5. It was observed that by adjusting the concentration of the starting solution, the size of resultant nanoparticles can be altered without the use of additional surfactants. This can be observed in a visible change in colour due to the shift in SPR absorption.²⁰⁹ Further to this, the auric acid was reduced without the use of any additional reducing agents but from a combination of thermal decomposition and reactions with the by-products of sol-

Table 6.1: Materials that have been deposited and described for this thesis and their selected properties.

Material	Properties and character
SnO ₂	Polycrystalline and transparent (>70% over 400-800 nm)
FTO	Polycrystalline, transparent (>70% over 400-800 nm) and low sheet resistance(8 Ω/□)
AuNP on silica coated float glass	Crystalline, SPR absorption but not adhesive
AuNP on silica (glass) wool	Crystalline, SPR absorption and catalytic activity
AuNP/FTO and FTO/AuNP composites	Transparent (>70% over 400-800 nm), low sheet resistance(8 Ω/□), SPR absorption and adhesive AuNPs
Other metal oxides/AuNP composites (TiO ₂ , ZnO, MgO, Al ₂ O ₃ and Ga ₂ O ₃)	Metal oxides were poly crystalline or amorphous, adhesive AuNPs and SPR absorption

vent breakdown. This work furthers previous reports of CVD synthesis of AuNPs,³⁸ by showing that some control can be exerted on the final nanoparticle thin film.

A one-pot solution of Au and Sn precursors managed to produce a composite thin film of AuNPs and SnO₂, however these thin films suffered from high C contamination and poor conductivity. As had been shown with AuNPs, depositions of the thin films individually might be more useful as it allows the user to tailor their material to meet specific application design needs. A layered structure was thus proposed and deposited, resulting in a material with high quality TCO properties and SPR absorbances. Further to this, the adherence problem to glass substrate encountered by AuNPs had been overcome^{112,160} without resorting to harsh treatments involving piranha solutions which are needed for silanisation reactions.^{37,161,162} Compared to previous AuNP:SnO₂

composites¹⁹² the materials produced here had far superior optical and electronic properties for transparent conducting applications not reported prior to publication generated from this thesis.

In Chapter 4, the depositions of AuNP composites expanded to other metal oxides, with the effect of the SPR observed based on the refractive index character of the metal oxide. The SPR of AuNPs have been widely reported to shift according to the refractive index of the surrounding media.^{12,166,222} The adaptability and rich background of metal oxide AACVD²²¹ was taken advantage of by the depositions of SnO₂ as well as MgO, Al₂O₃, TiO₂, ZnO, and Ga₂O₃ and their composites with AuNPs. The refractive indices were measured using ellipsometric results as multiple factors in the synthesis of the metal oxide thin films can affect the optical properties, and so accuracy with regards to any discussion about the optical character is maintained. Through the AACVD method a "bank" of new composites have been created. Even though no correlation was observed between the refractive index and the AuNPs' SPR, reports in this chapter highlight the tunability of the optical properties of the thin film, without the need to change the shape, size or concentration of the AuNPs. The SPR of AuNPs composites were found to have red-shifted but the lack of correlation sheds light on the importance of film and growth morphology on the interface between the metal oxide and AuNPs, and resulting plasmon physics. This was due to either the inconsistencies of how each precursor reacted and deposited, assumed from the different surfaces of each metal oxide, or a change in the AuNPs during the second deposition. The results from this chapter will be important to those that use nanoparticles as a colourant for coatings since the only experimental studies performed for this relationship only takes into account local refractive index and the CVD technique used here is analogous to current coating technologies.^{222,224,252}

As AACVD can be used to deposit of silica coated float glass, in Chapter 5

it is used to deposit Au particles onto silica (glass) wool. This high surface area support is ideal for catalytic purposes. There is reusability and recyclability potential since the glass wool can be easily recovered from a reactor. Although there were some loss of precursor due to depositions on the walls of the reactor, these depositions still showcase AACVD's versatility in the lab for its ability to deposit on different substrates. Catalytic experiments on the oxidation of benzyl alcohol showed that it has over 90% selectivity, as expected this is lower than the >99% reported nanoparticles specially synthesised to be catalysts²⁵³ since the size of the Au particles are much larger than the reported optimum.²⁴⁹ The yield is relatively low compared to the literature, however we think this can be improved by changing the reaction set up - the active sites might be blocked due to the tangled up nature of the glass wool. In order to counter the loss of precursor during deposition, several preliminary investigations were carried out using a spray deposition set up, which seems promising giving a more targeted area of deposition.

Overall, this thesis really showcases AACVD's strength for depositing a range of functional properties materials (catalysis, TCO, SPR) onto a variety of substrates (float glass and glass wool) allowing us to explore the properties of many materials.

6.2 Forward look

In a more general tone, the tools described in this thesis relating to the structures of nanocomposite films can be developed and tested for other functional properties, and as part of device development. This is an area that has not been explored here. Expansion into a range of catalytic systems other than the oxidation of alcohols and further work into recyclability of the AuNPs deposited onto glass wool, by aerosol-assisted chemical vapour deposition and spray de-

position, would be interesting in terms of potential applicability within industry. A wider study into the effects of refractive index on the SPR absorption can be further expanded to include different growth strategies and give a more complete understanding of the relationship between the metal oxide and gold nanoparticles in a composite. More specifically to each piece of work, the thesis can be carried forward with the following suggestions.

6.2.1 Functional composites of gold and tin dioxide

Investigating and comparing the use of MBTC with other Sn precursors. TGA can be used to study the breakdown of MBTC, HAuCl_4 and MBTC with HAuCl_4 , all dissolved in methanol. A simple benchtop reaction can perhaps elucidate the reactivity of the precursors with each other.

6.2.2 Effect of metal oxide character on the SPR in composites of AuNPs

Detailed SEM and TEM studies to further confirm whether the AuNPs change shape while being heated a second time during the second deposition. A comparison can be made for the metal oxide deposition and preferred orientation between the thin films deposited on glass and on the AuNPs. Further the functionality testing of each metal oxide composite. The interface between the metal oxide and gold nanoparticles using side-on SEM analysis can reveal the bonding that exists between the metal oxide and gold.

6.2.3 Gold nanoparticles on silica wool

In order to complete the catalytic studies, a catalytic test of blank glass wool should be performed with this set up. It would be interesting to compare the catalytic activity of the NPs produced in the AACVD reactor with the ones

from the spray rig. Always important to industry, recycling the catalyst and checking the activity will also be valuable to see if loading AuNPs on glass wool is actually viable. Lastly, more experiments of tuning the various factors of the reactions can be done to see if smaller NPs can be achieved through either the AACVD or the spray rig.

Bibliography

- [1] A. E. Ennos, *British Journal of Applied Physics*, 1957, **8**, 113–117.
- [2] P. Lee, J. Lee, H. Lee, J. Yeo, S. Hong, K. H. Nam, D. Lee, S. S. Lee and S. H. Ko, *Advanced Materials*, 2012, **24**, 3326–3332.
- [3] W. Gaynor, G. F. Burkhard, M. D. McGehee and P. Peumans, *Advanced Materials*, 2011, **23**, 2905–2910.
- [4] J. C. C. Fan and J. B. Goodenough, *Journal of Applied Physics*, 1977, **48**, 3524.
- [5] P. P. Edwards, A. Porch, M. O. Jones, D. V. Morgan and R. M. Perks, *Dalton Transactions*, 2004, 2995–3002.
- [6] Ç. Kiliç and A. Zunger, *Physical Review Letters*, 2002, **88**, 7–10.
- [7] G. Sanon, R. Rup and A. Mansingh, *Physical Review B*, 1991, **44**, 5672–5680.
- [8] K. Hitchman and K. Jensen, *Chemical Vapour Deposition: Principles and Applications*, Academic Press, 1st edn., 1993.
- [9] D. I. Fotiadis and K. F. Jensen, *Journal of Crystal Growth*, 1990, **102**, 743–761.
- [10] S. Link and M. a. El-Sayed, *The Journal of Physical Chemistry B*, 1999, **103**, 4212–4217.
- [11] P. Senthil Kumar, I. Pastoriza-Santos, B. Rodríguez-González, F. Javier García de Abajo and L. M. Liz-Marzán, *Nanotechnology*, 2008, **19**, 015606.
- [12] G. Walters and I. P. Parkin, *Journal of Materials Chemistry*, 2009, **19**, 574.
- [13] J. M. Cowley, *Diffraction Physics*, North-Holland Pub. Co, 1975.
- [14] E. Ramsden, *Hall-Effect Sensors*, Newnes, 2006.
- [15] D. C. Joy, *Scanning Electron Microscope (SEM)*, 2016, <http://www.britannica.com/technology/scanning-electron-microscope>.

-
- [16] S. Hofmann, *Auger- and X-Ray Photoelectron Spectroscopy in Materials Science: A User Orientated Guide*, Springer Science and Business Media, 2012.
- [17] H. M. McNair and J. M. Miller, *Basic Gas Chromatography*, Wiley, 2nd edn., 2009.
- [18] W. H. Baur, *Acta Crystallographica*, 1956, **9**, 515–520.
- [19] W. P. Davey, *Physical Review*, 1925, **25**, 753–761.
- [20] C. Granqvist and A. Hultåker, *Thin Solid Films*, 2002, **411**, 1–5.
- [21] G. Haacke, *Annual Review of Materials Science*, 1977, **7**, 73–93.
- [22] S. Bidwell, *Proceedings of the Physical Society of London*, 1885, **7**, 129–145.
- [23] W. von Uljanin, *Annalen der Physik und Chemie*, 1888, **XXXIV**, 242–273.
- [24] R. Groth, *Physica Status Solidi B*, 1966, **14**, 69–75.
- [25] C. Granqvist, *Solar Energy Materials and Solar Cells*, 2000, **60**, 201–262.
- [26] J. Zou, C. Z. Li, C. Y. Chang, H. L. Yip and A. K. Y. Jen, *Advanced Materials*, 2014, **26**, 3618–3623.
- [27] B. O’Connor, C. Haughn, K. H. An, K. P. Pipe and M. Shtein, *Applied Physics Letters*, 2008, **93**, 1–4.
- [28] K. Chopra, S. Major and D. Pandya, *Thin Solid Films*, 1983, **102**, 1–46.
- [29] D. Jeannot, J. Pinard, P. Ramoni and E. Jost, *IEEE Transactions on Components, Packaging, and Manufacturing Technology: Part A*, 1994, **17**, 17–23.
- [30] J. J. Thomson, *Proceedings of the Cambridge Philosophical Society*, 1901, **11**, 120–122.
- [31] E. Sondheimer, *Advances in Physics*, 1952, **1**, 1–42.
- [32] K. Fuchs and N. F. Mott, *Mathematical Proceedings of the Cambridge Philosophical Society*, 1938, **34**, 100.
- [33] D. Aspnes, *Thin Solid Films*, 1982, **89**, 249–262.
- [34] J. D. Porter, A. Heller and D. E. Aspnes, *Nature*, 1985, **313**, 664–666.
- [35] M. J. Tierney and C. R. Martin, *The Journal of Physical Chemistry*, 1989, **93**, 2878–2880.

- [36] J. Y. Lee, S. T. Connor, Y. Cui and P. Peumans, *Nano Letters*, 2008, **8**, 689–692.
- [37] C. A. Goss, D. H. Charych and M. Majda, *Analytical Chemistry*, 1991, **63**, 85–88.
- [38] R. G. Palgrave and I. P. Parkin, *Chemistry of Materials*, 2007, **19**, 4639–4647.
- [39] S. De, T. M. Higgins, P. E. Lyons, E. M. Doherty, P. N. Nirmalraj, W. J. Blau, J. J. Boland and J. N. Coleman, *ACS Nano*, 2009, **3**, 1767–1774.
- [40] X. Y. Zeng, Q. K. Zhang, R. M. Yu and C. Z. Lu, *Advanced Materials*, 2010, **22**, 4484–4488.
- [41] M. Theuring, V. Steenhoff, S. Geißendörfer, M. Vehse, K. von Maydell and C. Agert, *Optics Express*, 2015, **23**, A254.
- [42] M. W. Rowell, M. A. Topinka, M. D. McGehee, H. J. Prall, G. Dennler, N. S. Sariciftci, L. Hu and G. Gruner, *Applied Physics Letters*, 2006, **88**, 86–89.
- [43] J. Van De Lagemaat, T. M. Barnes, G. Rumbles, S. E. Shaheen, T. J. Coutts, C. Weeks, I. Levitsky, J. Peltola and P. Glatkowski, *Applied Physics Letters*, 2006, **88**, 3–6.
- [44] M. A. Contreras, T. Barnes, J. V. D. Lagemaat, G. Rumbles, T. J. Coutts, C. Weeks, P. Glatkowski, I. Levitsky, J. Peltola and D. A. Britz, *The Journal of Physical Chemistry C*, 2007, **111**, 14045–14048.
- [45] G. Helwig, *Zeitschrift für Physik*, 1952, **132**, 621–642.
- [46] A. J. Varkey and A. Fort, *Thin Solid Films*, 1994, **239**, 211–213.
- [47] Y.-S. Choi, C.-G. Lee and S. Cho, *Thin Solid Films*, 1996, **289**, 153–158.
- [48] R. Maity and K. K. Chattopadhyay, *Solar Energy Materials and Solar Cells*, 2006, **90**, 597–606.
- [49] B. Saha, R. Thapa and K. K. Chattopadhyay, *Solid State Communications*, 2008, **145**, 33–37.
- [50] O. Mryasov and A. Freeman, *Physical Review B*, 2001, **64**, 2–4.
- [51] J. A. Van Vechten and C. D. Thurmond, *Physical Review B*, 1976, **14**, 3539–3550.
- [52] Z. M. Jarzebski and J. P. Marton, *Journal of The Electrochemical Society*, 1976, **123**, 199C–205C.
- [53] Z. M. Jarzebski, *Journal of The Electrochemical Society*, 1976, **123**, 199C.

-
- [54] B. J. Ingram, G. B. Gonzalez, D. R. Kammler, M. I. Bertoni and T. O. Mason, *Journal of Electroceramics*, 2004, **13**, 167–175.
- [55] G. Zhang, C. Xie, S. Zhang, S. Zhang and Y. Xiong, *The Journal of Physical Chemistry C*, 2014, **118**, 18097–18109.
- [56] A. K. Singh, A. Janotti, M. Scheffler and C. G. Van De Walle, *Physical Review Letters*, 2008, **101**, 1–4.
- [57] Y. Mizokawa and S. Nakamura, *Japanese Journal of Applied Physics*, 1975, **14**, 779–788.
- [58] P. Di Nola, F. Morazzoni, R. Scotti and D. Narducci, *Journal of the Chemical Society, Faraday Transactions*, 1993, **89**, 3711–3713.
- [59] S. F. J. Cox, E. A. Davis, S. P. Cottrell, P. J. C. King, J. S. Lord, J. M. Gil, H. V. Alberto, R. C. Vilao, J. P. Duarte, N. A. De Campos, A. Weidinger, R. L. Lichti and S. J. C. Irvine, *Physical Review Letters*, 2001, **86**, 2601–2604.
- [60] D. M. Hofmann, A. Hofstaetter, F. Leiter, H. Zhou, F. Henecker, B. K. Meyer, S. B. Orlinskii, J. Schmidt and P. G. Baranov, *Physical Review Letters*, 2002, **88**, 045504.
- [61] P. D. C. King, R. L. Lichti, Y. G. Celebi, J. M. Gil, R. C. Vilão, H. V. Alberto, J. Piroto Duarte, D. J. Payne, R. G. Egdell, I. McKenzie, C. F. McConville, S. F. J. Cox and T. D. Veal, *Physical Review B - Condensed Matter and Materials Physics*, 2009, **80**, 1–4.
- [62] J. Kane, H. P. Schweizer and W. Kern, *Journal of The Electrochemical Society*, 1975, **122**, 1144–1149.
- [63] J. A. Aboaf, V. C. Marcotte and N. J. Chou, *Journal of The Electrochemical Society*, 1973, **120**, 701.
- [64] H. Kim and H. a. Laitinen, *Journal of the American Ceramic Society*, 1975, **58**, 23–25.
- [65] I. Austin and N. Mott, *Advances in Physics*, 1969, **18**, 41–102.
- [66] H. L. Tuller and A. S. Nowick, *Journal of Physics and Chemistry of Solids*, 1977, **38**, 859–867.
- [67] D. H. Zhang and H. L. Ma, *Applied Physics A*, 1996, **62**, 487–492.
- [68] D. Belanger, J. P. Dodelet, B. A. Lombos and J. I. Dickson, *Journal of the Electrochemical Society*, 1985, **132**, 1398–1405.
- [69] D. S. Bhachu, M. R. Waugh, K. Zeissler, W. R. Branford and I. P. Parkin, *Chemistry - A European Journal*, 2011, **17**, 11613–21.
-

- [70] D. S. Bhachu, D. O. Scanlon, G. Sankar, T. D. Veal, R. G. Egdell, G. Cibin, A. J. Dent, C. E. Knapp, C. J. Carmalt and I. P. Parkin, *Chemistry of Materials*, 2015, **27**, 2788–2796.
- [71] S. Goldsmith, E. Çetinörgü and R. L. Boxman, *Thin Solid Films*, 2009, **517**, 5146–5150.
- [72] C. G. Granqvist, *Solar Energy Materials and Solar Cells*, 2007, **91**, 1529–1598.
- [73] E. Burstein, *Physical Review*, 1954, **93**, 632–633.
- [74] I. Hamberg, C. Granqvist, K. Berggren, B. Sernelius and L. Engström, *Physical Review B*, 1984, **30**, 3240–3249.
- [75] G. D. Cody, T. Tiedje, B. Abeles, B. Brooks and Y. Goldstein, *Physical Review Letters*, 1981, **47**, 1480–1483.
- [76] F. Atay, V. Bilgin, I. Akyuz, E. Ketenci and S. Kose, *Journal of Non-Crystalline Solids*, 2010, **356**, 2192–2197.
- [77] C. Agashe and S. S. Major, *Journal of Materials Science*, 1996, **31**, 2965–2969.
- [78] J. T. Wang, X. L. Shi, W. W. Liu, X. H. Zhong, J. N. Wang, L. Pyrah, K. D. Sanderson, P. M. Ramsey, M. Hirata and K. Tsuru, *Scientific Reports*, 2014, **4**, 3679.
- [79] N. Noor and I. P. Parkin, *Journal of Materials Chemistry C*, 2013, **1**, 984.
- [80] A. I. Martínez, L. Huerta, J. M. O-Rueda de León, D. Acosta, O. Malik and M. Aguilar, *Journal of Physics D: Applied Physics*, 2006, **39**, 5091–5096.
- [81] S. V. Pepper, *Journal of Applied Physics*, 1974, **45**, 2947.
- [82] R. Asomoza, A. Maldonado, J. Rickards, E. P. Zironi, M. H. Farias, L. Cota-Araiza and G. Soto, *Thin Solid Films*, 1991, **203**, 195.
- [83] B. Gottlieb, R. Koropecski, R. Arce, R. Crisalle and J. Ferron, *Thin Solid Films*, 1991, **199**, 13–21.
- [84] K. Nietering, C. Mason and R. Carter III, *Analytica Chimica Acta*, 1986, **186**, 279–282.
- [85] H. Liu, V. Avrutin, N. Izyumskaya, Ü. Özgür and H. Morkoç, *Superlattices and Microstructures*, 2010, **48**, 458–484.
- [86] E. Pedrueza, J. Sancho-Parramon, S. Bosch, J. L. Valdés and J. P. Martinez-Pastor, *Nanotechnology*, 2013, **24**, 065202.

-
- [87] J. Hu and R. G. Gordon, *Journal of Applied Physics*, 1992, **71**, 880.
- [88] R. G. Gordon, J. Proscia, F. B. Ellis and A. E. Delahoy, *Solar Energy Materials*, 1989, **18**, 263–281.
- [89] J. I. Pankove, *Optical Processes in Semiconductors*, Dover Publications: New York, 1971.
- [90] G. Boschloo and D. Fitzmaurice, *The Journal of Physical Chemistry B*, 1999, **103**, 3093–3098.
- [91] U. zum Felde, M. Haase and H. Weller, *The Journal of Physical Chemistry B*, 2000, **104**, 9388–9395.
- [92] M. Batzill and U. Diebold, *Progress in Surface Science*, 2005, **79**, 47–154.
- [93] X. Hou and K.-L. Choy, *Chemical Vapor Deposition*, 2006, **12**, 583–596.
- [94] G. Korotcenkov and S. D. Han, *Materials Chemistry and Physics*, 2009, **113**, 756–763.
- [95] C. Agashe, B. Marathe, M. Takwale and V. Bhide, *Thin Solid Films*, 1988, **164**, 261–264.
- [96] F. M. Amanullah, K. J. Pratap and V. H. Babu, *Materials Science and Engineering B-Solid State Materials for Advanced Technology*, 1998, **52**, 93–98.
- [97] A. G. Zawadzki, C. J. Giunta and R. G. Gordon, *The Journal of Physical Chemistry*, 1992, **96**, 5364–5379.
- [98] a. N. Vorob'ev, S. Y. Karpov, M. V. Bogdanov, a. E. Komissarov, O. V. Bord, a. I. Zhmakin and Y. N. Makarov, *Computational Materials Science*, 2002, **24**, 520–534.
- [99] R. N. Ghoshtagore, *Journal of The Electrochemical Society*, 1978, **125**, 110.
- [100] K. Choy, *Progress in Materials Science*, 2003, **48**, 57–170.
- [101] A. Gamard, B. Jousseume, T. Toupance and G. Campet, *Inorganic Chemistry*, 1999, **38**, 4671–4679.
- [102] M. Epifani, M. Alvisi, L. Mirengi, G. Leo, P. Siciliano and L. Vasanelli, *Journal of the American Ceramic Society*, 2001, **84**, 48–54.
- [103] X. Du and S. M. George, *Sensors and Actuators, B: Chemical*, 2008, **135**, 152–160.
- [104] X. Li, X. Meng, J. Liu, D. Geng, Y. Zhang, M. N. Banis, Y. Li, J. Yang, R. Li, X. Sun, M. Cai and M. W. Verbrugge, *Advanced Functional Materials*, 2012, **22**, 1647–1654.
-

BIBLIOGRAPHY

- [105] M. S. Hwang, B. Y. Jeong, J. Moon, S. K. Chun and J. Kim, *Materials Science and Engineering B: Solid-State Materials for Advanced Technology*, 2011, **176**, 1128–1131.
- [106] J. B. Mooney and S. B. Radding, *Annual Review of Materials Science*, 1982, **12**, 81–101.
- [107] B. P. Jelle, A. Hynd, A. Gustavsen, D. Arasteh, H. Goudey and R. Hart, *Solar Energy Materials and Solar Cells*, 2012, **96**, 1–28.
- [108] T. D. Manning, I. P. Parkin, M. E. Pemble, D. Sheel and D. Vernardou, *Chemistry of Materials*, 2004, **16**, 744–749.
- [109] N. Noor, C. K. T. Chew, D. S. Bhachu, M. R. Waugh, C. J. Carmalt and I. P. Parkin, *Journal of Materials Chemistry C*, 2015, **3**, 9359–9368.
- [110] L. Popova, M. Michailov, V. Gueorguiev and A. Shopov, *Thin Solid Films*, 1990, **186**, 107–112.
- [111] D. W. Cooper, *Aerosol Science and Technology*, 1986, **5**, 287–299.
- [112] R. G. Palgrave and I. P. Parkin, *Journal of the American Chemical Society*, 2006, **128**, 1587–97.
- [113] S. Ponja, S. Sathasivam, N. Chadwick, A. Kafizas, S. M. Bawaked, A. Y. Obaid, S. Al-Thabaiti, S. N. Basahel, I. P. Parkin and C. J. Carmalt, *Journal of Materials Chemistry A*, 2013, **1**, 6271.
- [114] T. Larsson, H. O. Blom, C. Nender and S. Berg, *Journal of Vacuum Science & Technology A: Vacuum, Surfaces, and Films*, 1988, **6**, 1832.
- [115] A. Martel, F. Caballero-Briones, P. Bartolo-Pérez, A. Iribarren, R. Castro-Rodríguez, A. Zapata-Navarro and J. Peña, *Surface and Coatings Technology*, 2001, **148**, 103–109.
- [116] C. Agashe, M. G. Takwale, V. G. Bhide, S. Mahamuni and S. K. Kulkarni, *Journal of Applied Physics*, 1991, **70**, 7382.
- [117] K. Takahashi, A. Kunz, D. Woiki and P. Roth, *The Journal of Physical Chemistry A*, 2000, **104**, 5246–5253.
- [118] A. van Mol, Y. Chae, A. McDaniel and M. Allendorf, *Thin Solid Films*, 2006, **502**, 72–78.
- [119] C. Borman and R. Gordon, *Journal of The Electrochemical Society*, 1989, **136**, 3820.
- [120] C. J. Giunta, D. A. Strickler and R. G. Gordon, *The Journal of Physical Chemistry*, 1993, **97**, 2275–2283.

-
- [121] J. Dutta, J. Perrin, T. Emeraud, J. M. Laurent and A. Smith, *Journal of Materials Science*, 1995, **30**, 53–62.
- [122] M. Vernon, T. R. Hayes and V. M. Donnelly, *Journal of Vacuum Science & Technology A: Vacuum, Surfaces, and Films*, 1992, **10**, 3499–3506.
- [123] T. Maruyama and Y. Ikuta, *Solar Energy Materials and Solar Cells*, 1992, **28**, 209–215.
- [124] K.-M. Chi, C.-C. Lin, Y.-H. Lu and J.-H. Liao, *Journal of the Chinese Chemical Society*, 2000, **47**, 425–431.
- [125] M. Verdenelli, S. Parola, L. G. Hubert-Pfalzgraf and S. Lecocq, *Polyhedron*, 2000, **19**, 2069–2075.
- [126] T. T. Stoycheva, S. Vallejos, R. G. Pavelko, V. S. Popov, V. G. Sevastyanov and X. Correig, *Chemical Vapor Deposition*, 2011, **17**, 247–252.
- [127] M. E. Warwick, C. W. Dunnill and R. Binions, *Chemical Vapor Deposition*, 2010, **16**, 220–224.
- [128] R. G. Dhere, H. R. Moutinho, S. Asher, D. Young, X. Li, R. Ribelin and T. Gessert, *AIP Conference Proceedings*, 1999, pp. 242–247.
- [129] E. Shanthi, V. Dutta and K. L. Banerjee, A. Chopra, *Journal of Applied Physics*, 1980, **51**, 6243–6251.
- [130] C. F. Wan, R. D. McGrath, W. F. Keenan and S. N. Frank, *Journal of The Electrochemical Society*, 1989, **136**, 1459.
- [131] T. Maruyama and K. Tabata, *Journal of Applied Physics*, 1990, **68**, 4282.
- [132] C. Ristoscu, L. Cultrera, A. Dima, A. Perrone, R. Cutting, H. Du, A. Busiakiewicz, Z. Klusek, P. Datta and S. Rose, *Applied Surface Science*, 2005, **247**, 95–100.
- [133] K. Yoon and J. Song, *Thin Solid Films*, 1993, **224**, 203–208.
- [134] Y. Farber, F. Khonsari-Arefi and J. Amouroux, *Thin Solid Films*, 1994, **241**, 282–286.
- [135] J. Geurts, S. Rau, W. Richter and F. Schmitte, *Thin Solid Films*, 1984, **121**, 217–225.
- [136] M. M. Reddy, S. Jawalekar and A. Chandorkar, *Thin Solid Films*, 1989, **169**, 117–126.
- [137] W. K. Choi, H. Sung, K. H. Kim, J. S. Cho, S. C. Choi, H.-J. Jung, S. K. Koh, C. M. Lee and K. Jeong, *Journal of Materials Science Letters*, 1997, **16**, 1551–1554.
-

- [138] K. Kim and J. Chun, *Thin Solid Films*, 1986, **141**, 287–295.
- [139] Y. Matsui, M. Mitsuhashi, Y. Yamamoto and S. Higashi, *Thin Solid Films*, 2007, **515**, 2854–2859.
- [140] H. Cachet, A. Gamard, G. Campet, B. Jousseume and T. Toupance, *Thin Solid Films*, 2001, **388**, 41–49.
- [141] K. Subba Ramaiah and V. Sundara Raja, *Applied Surface Science*, 2006, **253**, 1451–1458.
- [142] M. Fantini and I. Torriani, *Thin Solid Films*, 1986, **138**, 255–265.
- [143] K. C. Molloy and J. E. Stanley, *Applied Organometallic Chemistry*, 2009, **23**, 62–67.
- [144] R. von Wagner, *Manual of Chemical Technology*, D. Appleton & co., 1987, p. 452.
- [145] R. Zsigmondy, *Justus Liebig's Annalen der Chemie*, 1898, **301**, 361–387.
- [146] J. D. Ruye, *US Patent US4339541 A*, 1982.
- [147] U. Kreibig and M. Vollmer, *Optical Properties of Metal Clusters*, Springer, 1995.
- [148] M. Faraday, *Philosophical Transactions of the Royal Society of London*, 1857, **147**, 145–181.
- [149] S. Underwood and P. Mulvaney, *Langmuir*, 1994, **10**, 3427–3430.
- [150] G. Mie, *Annalen der Physik*, 1908, **330**, 377–445.
- [151] C. Chen and E. Burstein, *Physical Review Letters*, 1980, **45**, 1287–1291.
- [152] S. Link and M. A. El-Sayed, *The Journal of Physical Chemistry B*, 1999, **103**, 8410–8426.
- [153] R. H. Doremus, *Langmuir*, 2002, **18**, 2436–2437.
- [154] J. A. Creighton, C. G. Blatchford and M. G. Albrecht, *Journal of the Chemical Society, Faraday Transactions 2*, 1979, **75**, 790.
- [155] N. Félidj, J. Aubard, G. Lévi, J. R. Krenn, A. Hohenau, G. Schider, A. Leitner and F. R. Aussenegg, *Applied Physics Letters*, 2003, **82**, 3095–3097.
- [156] B. R. Cuenya, *Thin Solid Films*, 2010, **518**, 3127–3150.
- [157] B. V. Enustun and J. Turkevich, *Journal of the American Chemical Society*, 1963, **85**, 3317–3328.

-
- [158] M. A. Uppal, A. Kafizas, M. B. Ewing and I. P. Parkin, *New Journal of Chemistry*, 2010, **34**, 2906.
- [159] M. Brust, M. Walker, D. Bethell, D. J. Schiffrin and R. Whyman, *Journal of the Chemical Society, Chemical Communications*, 1994, 801.
- [160] B. G. Prevo, J. C. Fuller and O. D. Velev, *Chemistry of Materials*, 2005, **17**, 28–35.
- [161] Y. Jin, X. Kang, Y. Song, B. Zhang, G. Cheng and S. Dong, *Analytical Chemistry*, 2001, **73**, 2843–2849.
- [162] O. Seitz, M. M. Chehimi, E. Cabet-Deliry, S. Truong, N. Felidj, C. Peruchot, S. J. Greaves and J. F. Watts, *Colloids and Surfaces A: Physicochemical and Engineering Aspects*, 2003, **218**, 225–239.
- [163] N. L. Rosi, D. A. Giljohann, C. S. Thaxton, A. K. R. Lytton-Jean, M. S. Han and C. A. Mirkin, *Science*, 2006, **312**, 1027–1030.
- [164] D. H. M. Dam, J. H. Lee, P. N. Sisco, D. T. Co, M. Zhang, M. R. Wasielewski and T. W. Odom, *ACS Nano*, 2012, **6**, 3318–26.
- [165] V. P. Zharov, K. E. Mercer, E. N. Galitovskaya and M. S. Smeltzer, *Biophysical Journal*, 2006, **90**, 619–627.
- [166] I. H. El-Sayed, X. Huang and M. A. El-Sayed, *Cancer Letters*, 2006, **239**, 129–135.
- [167] S. Perni, C. Piccirillo, J. Pratten, P. Prokopovich, W. Chrzanowski, I. P. Parkin and M. Wilson, *Biomaterials*, 2009, **30**, 89–93.
- [168] S. Nath, C. Kaittanis, A. Tinkham and J. M. Perez, *Analytical Chemistry*, 2008, **80**, 1033–1038.
- [169] V. Aguilar-Guerrero and B. C. Gates, *Catalysis Letters*, 2009, **130**, 108–120.
- [170] M. D. Hughes, Y.-J. Xu, P. Jenkins, P. McMorn, P. Landon, D. I. Enache, A. F. Carley, G. A. Attard, G. J. Hutchings, F. King, E. H. Stitt, P. Johnston, K. Griffin and C. J. Kiely, *Nature*, 2005, **437**, 1132–1135.
- [171] W. Deng, A. I. Frenkel, R. Si and M. Flytzani-Stephanopoulos, *Journal of Physical Chemistry C*, 2008, **112**, 12834–12840.
- [172] A. Ueda, T. Oshima and M. Haruta, *Applied Catalysis B: Environmental*, 1997, **12**, 81–93.
- [173] C. D. Pina, E. Falletta, M. L. Faro, M. Pasta and M. Rossi, *Gold Bulletin*, 2009, **42**, 27–33.

- [174] Z. Chen, C. Della Pina, E. Falletta, M. Lo Faro, M. Pasta, M. Rossi and N. Santo, *Journal of Catalysis*, 2008, **259**, 1–4.
- [175] M. Boualleg, K. Guillois, B. Istria, L. Burel, L. Veyre, J.-M. Basset, C. Thieuleux and V. Caps, *Chemical Communications*, 2010, **46**, 5361.
- [176] H. Tsunoyama, H. Sakurai, Y. Negishi and T. Tsukuda, *Journal of the American Chemical Society*, 2005, **127**, 9374–9375.
- [177] S. Cho, S. Lee, S.-g. Oh, S. J. Park, W. M. Kim, B.-k. Cheong, M. Chung, K. B. Song, T. S. Lee and S. G. Kim, *Thin Solid Films*, 2000, **377-378**, 97–102.
- [178] J. Deng, M. Gu and J. Di, *Applied Surface Science*, 2011, **257**, 5903–5907.
- [179] M. Aramendía, A. Marinas, J. Marinas, J. Moreno and F. Urbano, *Catalysis Today*, 2005, **101**, 187–193.
- [180] C. Gomes Silva, R. Juárez, T. Marino, R. Molinari and H. García, *Journal of the American Chemical Society*, 2011, **133**, 595–602.
- [181] Z. Liu, W. Hou, P. Pavaskar, M. Aykol and S. B. Cronin, *Nano Letters*, 2011, **11**, 1111–6.
- [182] M. Haruta, *CATTECH*, 2002, **6**, 102–115.
- [183] D. Zhang, M. Wang, A. G. Brolo, J. Shen, X. Li and S. Huang, *Journal of Physics D: Applied Physics*, 2013, **46**, 024005.
- [184] M. Okumura, S. Nakamura, S. Tsubota, T. Nakamura, M. Azuma and M. Haruta, *Catalysis Letters*, 1998, **51**, 53–58.
- [185] a. Patra, V. Damodara Das and S. Kasiviswanathan, *Thin Solid Films*, 2009, **518**, 1399–1401.
- [186] J.-A. Jeong and H.-K. Kim, *Solar Energy Materials and Solar Cells*, 2009, **93**, 1801–1809.
- [187] a. Roguska, a. Kudelski, M. Pisarek, M. Lewandowska, K. Kurzydłowski and M. Janik-Czachor, *Surface Science*, 2009, **603**, 2820–2824.
- [188] S. Vallejos, P. Umek, T. Stoycheva, F. Annanouch, E. Llobet, X. Correig, P. De Marco, C. Bittencourt and C. Blackman, *Advanced Functional Materials*, 2013, **23**, 1313–1322.
- [189] N. Tarwal, R. Devan, Y. Ma, R. Patil, M. Karanjkar and P. Patil, *Electrochimica Acta*, 2012, **72**, 32–39.
- [190] M. Saeli, R. Binions, C. Piccirillo, G. Hyett and I. P. Parkin, *Polyhedron*, 2009, **28**, 2233–2239.

-
- [191] H. Y. Y. Ko, M. Mizuhata, A. Kajinami and S. Deki, *Thin Solid Films*, 2005, **491**, 86–90.
- [192] S. H. Lee, D. M. Hoffman, A. J. Jacobson and T. R. Lee, *Chemistry of Materials*, 2013, **25**, 4697–4702.
- [193] S. Kundu, A. Kafizas, G. Hyett, A. Mills, J. A. Darr and I. P. Parkin, *Journal of Materials Chemistry*, 2011, **21**, 6854.
- [194] H. Fan, K. Yang, D. M. Boye, T. Sigmon, K. J. Malloy, X. Huifang, G. P. Lopez and C. Brinker, *Science*, 2004, **304**, 567–571.
- [195] J. Zhang, X. Liu, S. Wu, M. Xu, X. Guo and S. Wang, *Journal of Materials Chemistry*, 2010, **20**, 6453.
- [196] P. Manjula, S. Arunkumar and S. V. Manorama, *Sensors and Actuators B: Chemical*, 2011, **152**, 168–175.
- [197] R. Swanepoel, *Journal of Physics E: Scientific Instruments*, 1983, **16**, 1214–1222.
- [198] J. Tauc, *Materials Research Bulletin*, 1968, **3**, 37–46.
- [199] Y. Huang, D. Li, J. Feng, G. Li and Q. Zhang, *Journal of Sol-Gel Science and Technology*, 2010, **54**, 276–281.
- [200] M.-S. Hu, H.-L. Chen, C.-H. Shen, L.-S. Hong, B.-R. Huang, K.-H. Chen and L.-C. Chen, *Nature Materials*, 2006, **5**, 102–106.
- [201] T. Ung, L. M. Liz-Marzán and P. Mulvaney, *The Journal of Physical Chemistry B*, 2001, **105**, 3441–3452.
- [202] T. Miller, S. Bakrania, C. Perez and M. Wooldridge, *Journal of Materials Research*, 2011, **20**, 2977–2987.
- [203] R. Binions, C. Piccirillo, R. G. Palgrave and I. P. Parkin, *Chemical Vapor Deposition*, 2008, **14**, 33–39.
- [204] Y. Chae, W. G. Houf, A. H. McDaniel and M. D. Allendorf, *Journal of The Electrochemical Society*, 2006, **153**, C309.
- [205] W. K. Choi, *Journal of Vacuum Science & Technology A: Vacuum, Surfaces, and Films*, 1996, **14**, 359.
- [206] P. Rajaram, Y. C. Goswami, S. Rajagopalan and V. K. Gupta, *Materials Letters*, 2002, **54**, 158–163.
- [207] A. E. Rakhshani, Y. Makdisi and H. A. Ramazaniyan, *Journal of Applied Physics*, 1998, **83**, 1049–1057.

- [208] F. Simonis, M. van der Leij and C. Hoogendoorn, *Solar Energy Materials*, 1979, **1**, 221–231.
- [209] M. A. Uppal, A. Kafizas, T. H. Lim and I. P. Parkin, *New Journal of Chemistry*, 2010, **34**, 1401.
- [210] S. Badrinarayanan, A. B. Mandale, V. G. Gunjekar and A. P. B. Sinha, *Journal of Materials Science*, 1986, **21**, 3333–3338.
- [211] S. Süzer, T. Voscoboinikov, K. R. Hallam and G. C. Allen, *Analytical and Bioanalytical Chemistry*, 1996, **355**, 654–656.
- [212] M. P. Seah, G. C. Smith and M. T. Anthony, *Surface and Interface Analysis*, 1990, **15**, 293–308.
- [213] T. Thomas and P. Weightman, *Physical Review B*, 1986, **33**, 5405–5413.
- [214] C. R. Crick and I. P. Parkin, *Journal of Materials Chemistry*, 2011, **21**, 14712.
- [215] A. Panneerselvam, M. A. Malik, P. O’Brien and J. Raftery, *Journal of Materials Chemistry*, 2008, **18**, 3264.
- [216] X. Xu, M. Stevens and M. B. Cortie, *Chemistry of Materials*, 2004, **16**, 2259–2266.
- [217] O. Seitz, M. M. Chehimi, E. Cabet-Deliry, S. Truong, N. Felidj, C. Peruchot, S. J. Greaves and J. F. Watts, *Colloids and Surfaces A: Physicochemical and Engineering Aspects*, 2003, **218**, 225–239.
- [218] A. Primo, A. Corma and H. García, *Physical Chemistry Chemical Physics*, 2011, **13**, 886–910.
- [219] C. Bernard, I. Lyon and R. Berjoan, *Journal of SolGel Science and Technology*, 1997, **81**, 75–81.
- [220] J. Xiao and L. Qi, *Nanoscale*, 2011, **3**, 1383–96.
- [221] C. E. Knapp and C. J. Carmalt, *Chemical Society Reviews*, 2016, Advance Article.
- [222] J. J. Mock, D. R. Smith and S. Schultz, *Nano Letters*, 2003, **3**, 485–491.
- [223] T. R. Jensen, M. L. Duval, K. L. Kelly, A. A. Lazarides, G. C. Schatz and R. P. Van Duyne, *The Journal of Physical Chemistry B*, 1999, **103**, 9846–9853.
- [224] S. K. Medda, S. De and G. De, *Journal of Materials Chemistry*, 2005, **15**, 3278.

-
- [225] Y. K. Mishra, S. Mohapatra, R. Singhal, D. K. Avasthi, D. C. Agarwal and S. B. Ogale, *Applied Physics Letters*, 2008, **92**, 043107.
- [226] G. Battiston, R. Gerbasi, M. Porchia, R. Bertoniello and F. Caccavale, *Thin Solid Films*, 1996, **279**, 115–118.
- [227] A. Dillon, A. Ott, J. Way and S. George, *Surface Science*, 1995, **322**, 230–242.
- [228] C. E. Knapp, P. Marchand, C. Dyer, I. P. Parkin and C. J. Carmalt, *New Journal of Chemistry*, 2015, **39**, 6585–6592.
- [229] Y. Liu, J. Hsieh and S. Tung, *Thin Solid Films*, 2006, **510**, 32–38.
- [230] K. Vedam and S. Y. Kim, *Applied Optics*, 1989, **28**, 2691.
- [231] M. Rebien, W. Henrion, M. Hong, J. P. Mannaerts and M. Fleischer, *Applied Physics Letters*, 2002, **81**, 250–252.
- [232] K. Jiang, A. Eitan, L. S. Schadler, P. M. Ajayan, R. W. Siegel, N. Grobert, M. Mayne, M. Reyes-Reyes, H. Terrones and M. Terrones, *Nano Letters*, 2003, **3**, 275–277.
- [233] C. Dhanavantri, R. Karekar and V. Rao, *Thin Solid Films*, 1985, **127**, 85–92.
- [234] C. T. Campbell, *Science*, 2011, **234**, 234–235.
- [235] J. Schwank, *Gold Bulletin*, 1983, **16**, 103–110.
- [236] Y. Mikami, A. Dhakshinamoorthy, M. Alvaro and H. García, *Catalysis Science & Technology*, 2012, 58–69.
- [237] S. Eustis and M. A. El-Sayed, *Chemical Society Reviews*, 2006, **35**, 209–17.
- [238] K. E. Saeger and J. Rodies, *Gold Bulletin*, 1977, **10**, 10–14.
- [239] M. Haruta, *Gold Bulletin*, 2004, **37**, 27–36.
- [240] S. Panigrahi, S. Basu, S. Praharaj, S. Pande, S. Jana, A. Pal, S. K. Ghosh and T. Pal, *Journal of Physical Chemistry C*, 2007, **111**, 4596–4605.
- [241] F. G. Eichel and D. F. Othmer, *Industrial & Engineering Chemistry*, 1949, **41**, 2623–2626.
- [242] A. M. Clover, *Journal of the American Chemical Society*, 1924, **46**, 419–430.
- [243] L. Sandhiya and H. Zipse, *Chemistry - A European Journal*, 2015, **21**, 14060–14067.

- [244] C. E. H. Bawn and J. E. Jolley, *Proceedings of the Royal Society A: Mathematical, Physical and Engineering Sciences*, 1956, **237**, 297–312.
- [245] K. Yamaguchi and N. Mizuno, *Angewandte Chemie - International Edition*, 2002, **41**, 4538–4542.
- [246] L.-c. Wang, Y.-m. Liu, M. Chen, Y. Cao, H.-y. He and K.-n. Fan, *Journal of Physical Chemistry C*, 2008, **112**, 6981–6987.
- [247] M. D. Mantle, D. I. Enache, E. Nowicka, S. P. Davies, J. K. Edwards, C. Dagostino, D. P. Mascarenhas, L. Durham, M. Sankar, D. W. Knight, L. F. Gladden, S. H. Taylor and G. J. Hutchings, *Journal of Physical Chemistry C*, 2011, **115**, 1073–1079.
- [248] M. Sankar, E. Nowicka, E. Carter, D. M. Murphy, D. W. Knight, D. Bethell and G. J. Hutchings, *Nature communications*, 2014, **5**, 3332.
- [249] P. Haider, B. Kimmerle, F. Krumeich, W. Kleist, J.-D. Grunwaldt and A. Baiker, *Catalysis Letters*, 2008, **125**, 169–176.
- [250] M. Haruta, *Catalysis Today*, 1997, **36**, 153–166.
- [251] A. S. K. Hashmi and G. J. Hutchings, *Angewandte Chemie International Edition*, 2006, **45**, 7896–7936.
- [252] S. K. Medda, M. Mitra and G. De, *Journal of Chemical Sciences*, 2008, **120**, 565–572.
- [253] A. Abad, P. Concepción, A. Corma and H. García, *Angewandte Chemie (International ed. in English)*, 2005, **44**, 4066–9.